Inaugural – Dissertation

zur
Erlangung der Doktorwürde
der
Naturwissenschaftlich-Mathematischen Gesamtfakultät
der
Ruprecht-Karls-Universität Heidelberg

vorgelegt von
Diplom-Ingenieur Doris Höglinger
aus Rohrbach, Österreich

Tag der mündlichen Prüfung:

5. Oktober 2015

The roles of sphingosine in calcium signaling and Niemann-Pick disease type C

Gutachter:

Dr. Anne-Claude Gavin, EMBL Heidelberg

Prof. Dr. Felix Wieland, Universität Heidelberg

Dissertation

submitted to the
Combined Faculties for the Natural Sciences and for Mathematics
of the Ruperto-Carola University of Heidelberg, Germany

for the degree of

Doctor of Natural Sciences

presented by

Diplom-Ingenieur Doris Höglinger

born in Rohrbach, Austria

Oral examination:

5th October 2015

The roles of sphingosine in calcium signaling and Niemann-Pick disease type C

Referees:

Dr. Anne-Claude Gavin, EMBL Heidelberg

Prof. Dr. Felix Wieland, Universität Heidelberg

This work was carried out under the supervision of Dr. Carsten Schultz at the European Molecular Biology Laboratory (EMBL) in Heidelberg, Germany, between October 2011 and July 2015.

Abstract

Although several lipids have been shown to participate in intracellular signal transduction events and to influence central cellular processes, the bioactive actions of most lipids remain unexplored. This lack of knowledge is mainly due to a shortage of tools to manipulate lipid levels within living cells in a non-invasive way and to identify new protein interactors of single lipid species. This work presents the development of two methods to overcome these drawbacks applied to sphingosine (Sph). The origin of calcium signaling properties of Sph and its involvement in the pathophysiological development of the lysosomal storage disease Niemann-Pick type C (NPC) are reported.

First, 'caged' variants of sphingosine were synthesized which enable the precise elevation of Sph levels in single living cells within seconds using light. This acute increase in Sph concentration led to an immediate release of lysosomal calcium through the actions of the two-pore channel 1 (TPC1). In cells derived from NPC patients, an accumulation of Sph in the endolysosomal compartments was visualized for the first time. Additionally, NPC cells exhibited reduced calcium signals upon Sph uncaging, indicating that Sph accumulation is upstream of a calcium defect in this disease. Sph-induced calcium release also initiated the nuclear translocation of transcription factor EB, which positively regulates the expression of autophagic and lysosomal biogenesis genes, further underlining the importance of lysosomal calcium release in direct lysosome-to-nucleus signaling pathways.

In order to capture Sph-interacting proteins, a trifunctional Sph (TFS) was developed. TFS facilitates the release and immediate crosslinking of Sph to its interacting partners within the living cell. Mass-spectrometric analyses identified known Sph-binding proteins such as the ceramide synthase, as well as novel putative Sph-interactors. The general applicability of this method was proven by using trifunctional diacylglycerol as well as a trifunctional fatty acid. TFS was further employed in investigations of the subcellular localization and transport of Sph through the cell. NPC patient fibroblasts showed a striking accumulation of Sph in late endosomes and lysosomes. Sph transport out of these vesicles was severely hindered in the NPC condition. The kinetics of Sph efflux correlated with the severity of symptoms in different NPC patients, so this assay could potentially be used for monitoring and prognosis of NPC disease severity.

Zusammenfassung

Nur einige von tausenden Lipidspezies in eukaryotischen Zellen sind bereits bekannte bioaktive Lipide, welche in komplexe intrazelluläre Signalübertragungsnetzwerke eingebunden sind. Viele andere Lipide haben noch unerforschte Auswirkungen auf zelluläre Prozesse. Mögliche Gründe dafür sind die Schwierigkeiten, die Konzentration dieser Lipide in lebenden Zellen durch nicht-invasive Methoden zu manipulieren oder deren Wechselwirkungen mit Lipid-bindenden Proteinen zu erforschen.

In dieser Arbeit werden Methoden zur spezifischen Freisetzung von Lipiden mit hoher zeitlicher und räumlicher Auflösung sowie zur Proteom-weiten Identifizierung von Lipid-bindenden Proteinen in lebenden Zellen vorgestellt. Als Modelllipid diente Sphingosin (Sph), ein einkettiges Lipid aus der Gruppe der Sphingolipide, welches eine bedeutende, allerdings noch nicht näher definierte Rolle in der Pathologie der lysosomalen Erbkrankheit Niemann-Pick Typ C (NPC) spielt.

Die Modifizierung von Sph mit verschiedenen photospaltbaren Schutzgruppen lieferte inerte Sph-Vorläufer, welche nach Zugabe zu verschiedenen Zelllinien kein Signal auslösten. Erst durch Photospaltung direkt am Mikroskop erhöhte sich die Konzentration von Sph in einzelnen lebenden Zellen innerhalb von Sekunden. Dieser Anstieg löste die Freisetzung von Kalzium aus den lysosomalen Kalzium-Speichern aus, welche durch den Kalzium-Kanal TPC1 gesteuert wurde. Untersuchungen von NPC-Patientenzellen zeigten sowohl ein reduziertes lysosomales Kalzium-Signal als auch erhöhte Sph Konzentrationen in Endosomen und Lysosomen, welches den Schluss nahelegt, dass die Akkumulation von Sph in diesen Zellen zur Senkung des lysosomalen Kalziumspiegels beiträgt und somit die Fusion von Endosomen und Lysosomen erschwert. Die Bedeutung des Sph-induzierten Kalzium-Signals wurde durch die nachfolgende nukleare Translokation des Transkriptionsfaktors EB unterstrichen.

Die Entwicklung eines trifunktionalen Sph (TFS) ermöglichte die Freisetzung und sofortige Quervernetzung von Sph mit wechselwirkenden Proteinen in lebenden Zellen. Nachfolgende massenspektrometrische Analysen identifizierten bereits bekannte als auch potenziell neue Sph-bindende Proteine und zeigten die Anwendbarkeit dieses Konzepts auf andere Signallipide. TFS wurde auch benutzt, um die Lokalisation von Sph in NPC-Patientenzellen zu untersuchen. Eine deutliche Ansammlung von Sph in Endosomen und Lysosomen sowie ein erschwerter Transport von Sph aus diesen Organellen wurde sichtbar. Die Kinetik des Sph-Transports korrelierte direkt mit der Schwere der Smyptome dieser NPC-Patienten. Dieser Assay könnte somit in Zukunft zur Beobachtung und Prognose von NPC-Patienten verwendet werden.

Contents

List of Figures

“But then science is nothing but a series of questions that lead to more questions.”
— Terry Pratchett, *The Long Earth*

Chapter 1 - Introduction

1.1. Sphingolipids form a network of highly bioactive lipids and are involved in many cellular processes

Lipids are crucial for the functioning of all organisms. At the physiological level, lipids serve for the storage of energy in adipose tissues, mostly in the form of triglycerides[1]. On a cellular level, lipids are needed as structural components of membranes and are therefore essential for constituting the plasma membrane as well as for forming intracellular organelles[2]. However, more than 37 000 structurally distinct lipids have been identified so far[3], with more likely to come as technologies advance. Each eukaryotic cell is estimated to contain over 1000 different lipid species[2]. This diversity is too great to result from mere structural roles, and leads to the hypothesis that structurally different lipids have distinct functions. Indeed, some lipids have been shown to act as signaling molecules and their deregulation results in severe diseases such as cancer, inflammation and metabolic syndrome[4].

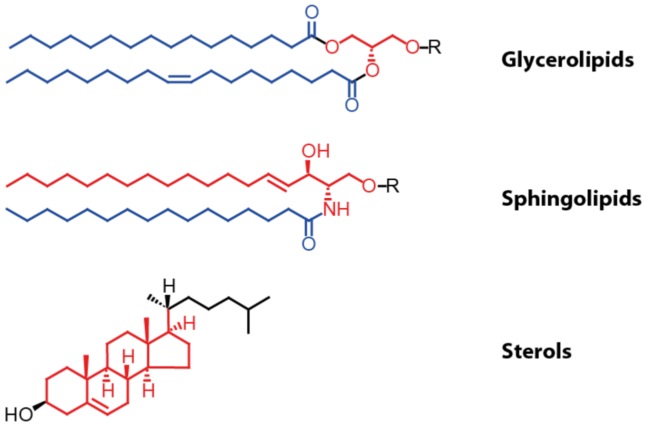

Figure 1.1 Major groups of membrane lipids in mammalian cells. The common backbone of each group is highlighted in red, fatty acids are shown in blue and R signifies variable headgroup modifications such as phosphate, ethanolamine, choline or sugars.

In mammalian cells, lipids are classified into three main categories: glycerolipids, sphinoglipids and sterol lipids (see Figure 1.1). Glycerolipids share glycerol as a common backbone and are the most abundant cellular lipids. The major glycerolipid by mass, phosphatidylcholine (PC), is the primary component of cellular membranes and already accounts for over 30 % of total cellular lipid content[5]. Sterols share the fused four-ring core structure of steroids (highlighted in red in Figure 1.1) and are modified by an alcohol functionality at position 3 of ring A. The main sterol lipid cholesterol and its derivates are essential for regulating membrane fluidity[6], while other sterol lipids such as bile acids aid in the solubilization and absorption of dietary fat from the intestine through formation of micelles[7]. Other steroid-derived molecules (e.g. androgens, estrogens or corticosteroids) have different biological roles as hormones and signaling molecules[8,9].

Sphingolipids are a closely related group of bioactive lipids which have a sphingoid (sometimes called long chain base) backbone. In mammalian cells, this backbone is sphingosine (see Figure 1.2 – sphingosine is highlighted in bold). Sphingolipids are synthesized via a *de novo* pathway starting with the condensation of L-serine with palmitoyl-CoA by the serine palmitoyltransferase (SPT) at the endoplasmic reticulum (ER). This is not only the start but also the key regulatory step for sphingolipid biosynthesis. Mutations in SPT can lead to a severe disease of the peripheral nervous system called hereditary sensory and autonomic neuropathy type I (HSAN1)[10]. The next step is mediated by 3-ketodihydrosphingosine reductase (KDSR) and yields dihydrosphingosine (dhSph), which can be recognized by several ceramide synthases (CerS) to form a variety of different dihydroceramides (dhCer), differing in fatty acyl chain length and saturation[11].

The dhCers are converted to ceramides (Cer) by the actions of a sphingolipid desaturase (DES). Ceramides are the central point of sphingolipid metabolism and have been implicated in the regulation of many biological processes, ranging from apoptosis[12] to inflammation[13] or autophagy[14]. Cers are further modified in four different ways:

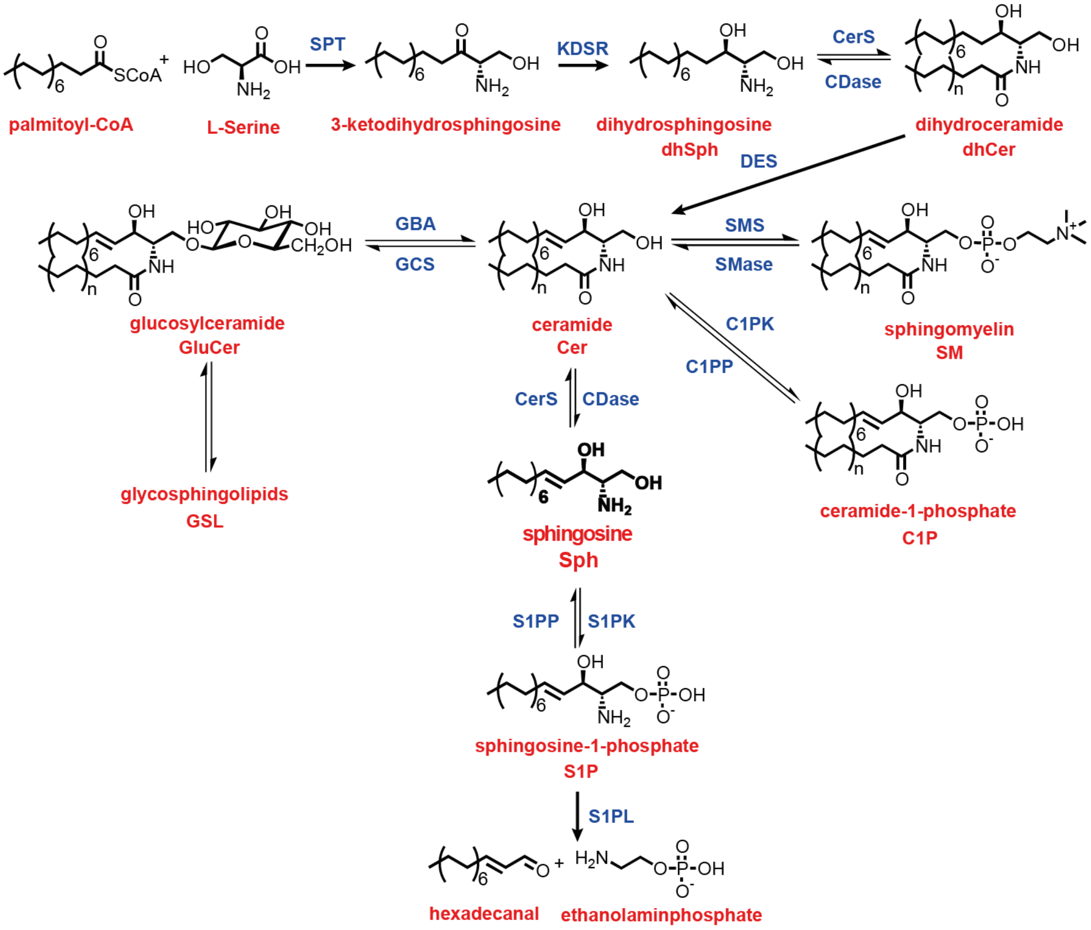

Figure 1.2 Overview of the sphingolipid metabolic pathway.

1.) Cer is phosphorylated by ceramide kinase (CerK) to give another biologically active lipid, ceramide-1-phosphate (C1P), which, interestingly, promotes cell survival[15] and migration[16], contrary outcomes to its parent molecule Cer.

2.) A family of sphingomyelin synthases (SMS) adds a choline headgroup to Cer, thus producing sphingomyelin (SM), the most abundant sphingolipid in mammalian cells. SM is found in high concentration (14-18 mol%[17]) at plasma membrane and is enriched in erythrocytes, nerve tissue and the brain[18].

3.) Cers are also modified by galactosyl- or glucosylceramide synthases (CDS) which attach galactose or glucose moieties to the headgroup of Cer to form galactosylceramide (GalCer) or glucosylceramide (GluCer) as illustrated in Figure 1.2. These serve as starting points for the formation of all complex glycosphinoglipids, which reach a great variety in glycan composition and are important receptors for carbohydrate binding proteins[19]. Mutations in enzymes of the glycosphingolipid metabolism lead to severe lipid storage disorders, such as Gaucher disease[20], Fabry disease[21], Tay-Sachse and Sandhoff disease[22] among others.

4.) The breakdown of Cer by ceramidases (CDase) leads to the formation of sphingosine (Sph), an important signaling molecule, which has been shown to be implicated in the regulation of growth arrest, apoptosis[23,24] and the pathophysiology of another lipid storage disease, Niemann-Pick type C[25] (see chapter 1.2).

Through the actions of two sphingosine kinases (SK1 and SK2), Sph can be rapidly converted to another powerful signaling lipid, sphingosine-1-phosphate (S1P), which is involved in proliferation and inflammation[26] and is therefore closely linked to carcinogenesis[27]. Like Cer and C1P, Sph and S1P also exhibit completely contrary signaling properties, even though they are closely linked structurally and metabolically. Given this high degree of convertibility between lipids with such opposing effects, it was proposed that the relative ratio between pro- and anti-apoptotic lipid levels, rather than the absolute concentrations determines cell fate in a 'rheostat' fashion[28]. Finally, the exit point of the sphingolipid metabolic pathway is the cleavage of the sphingosine backbone of S1P by sphingosine-1-phosphate lyase (S1PL) yielding hexadecanal and ethanolaminophosphate. S1PL is the only known enzyme to enable the irreversible exit of the sphingoid substrate from the sphingolipid metabolic pathway[29] and its knock-down leads to an accumulation of cholesterol esters and sphingolipids alongside severe neurodegenerative symptoms in mice[30–32].

The difficulties in studying sphingolipid signaling lie mainly in the high interconnectivity of the metabolic pathway, where many paths, often operating at the same time, can lead to the same lipid. Additionally, many sphingolipid metabolizing enzymes exist in families of different paralogs, all of which catalyze the same reaction (e.g. synthesis of Cer from Sph) but are regulated differently or even make products of different molecular identity (e.g. Cer with different fatty acid chain lengths and unsaturations)[33]. Yet another layer of complexity is added when considering the different subcellular localizations of the sphingolipid metabolic enzymes. Figure 1.3 summarizes what is known about sphingolipid localization, transport and metabolism in the cellular context.

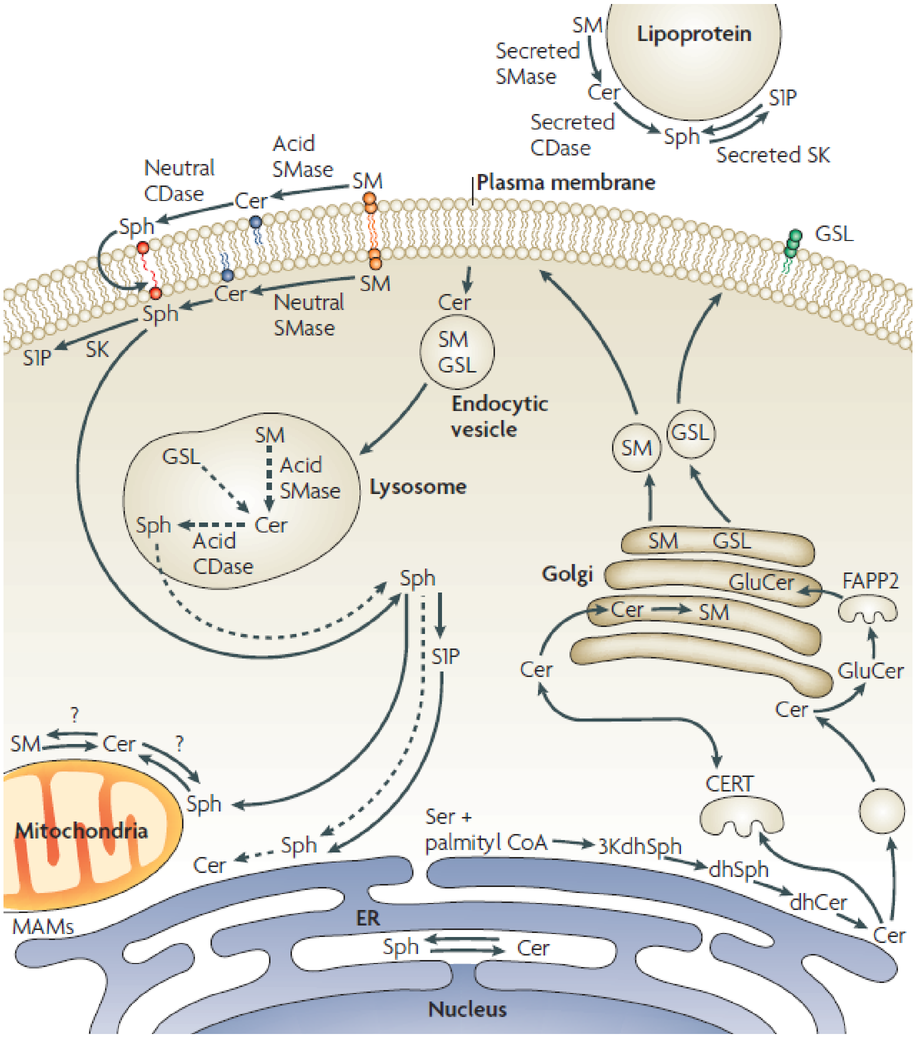

Figure 1.3 Subcellular compartmentalization of the sphingolipid metabolism. Figure is reprinted by permission from Macmillan Publishers Ltd: Nature Reviews Molecular Cell Biology, Hannun & Obeid[34] copyright 2008 under license number 3655250849060.

Many enzymes involved in the catabolism of higher sphingolipids (such as GBA, SMase or CDase) are localized to the endolysosomal system[35] (see Figure 1.3), whereas most enzymes involved in the *de novo* pathway are localized to the ER[34]. SM-synthases and glycosphingolipid synthases are localized to the Golgi apparatus[36]. Taking into account the poor solubility of lipids in cells (Cer in this example), it is necessary to facilitate transport from ER to Golgi, and subsequently to the plasma membrane. This may happen via vesicular transport or even dedicated transfer proteins such as the ceramide transfer protein (CERT)[37]. The regulation of this transport is another way to influence the levels of certain lipids in the cell and therefore transport proteins such as CERT could develop into important targets for therapy, specifically anticancer therapy in the future[38].

1.2. Sphingosine accumulates in the lipid storage disorder Niemann-Pick type C

Niemann-Pick disease type C (NPC) is a lysosomal storage disorder with a wide variability in clinical expression and age of onset. Typically, NPC patients develop neurological symptoms such as ataxia and progressive dementia and often die within the first decade[25]. As with most other lysosomal diseases, the genetic cause for NPC is well identified. Mutations in the genes encoding for two lysosomal proteins NPC1 (95 % of cases) or NPC2 (5 % of cases) lead to the development of this fatal neurodegenerative disorder[39]. However, the cellular functions of these proteins remain unclear. NPC2 is a small, soluble, lysosomal glycoprotein of 132 amino acids, which has been shown to extract and transport cholesterol between membranes[40]. NPC1 on the other hand is a multipass transmembrane protein with 13 transmembrane domains localized to the limiting membrane of late endosomes/lysosomes[41] (Figure 1.4). Its exact function remains unclear, but one luminal loop has been found necessary and sufficient for filovirus entry and infection[42] (see also chapter 1.5). Homology studies have furthermore identified a putative sterol sensing domain[39].

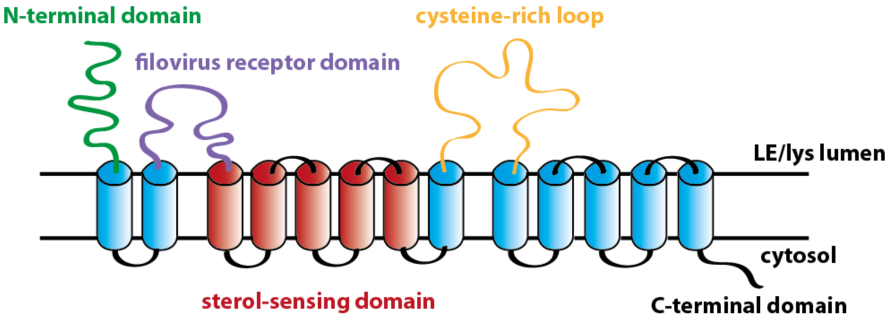

Figure 1.4 Topology of the NPC1 protein. Figure adapted from [41].

Mutational analysis of 30 unrelated NPC patients showed some clustering of the mutations in the luminal cysteine-rich loop as well as the sterol-sensing domain (SSD)[43], indicating the likely importance of these domains for the proper functioning of the NPC1 protein. In addition to the SSD, the N-terminal domain of NPC1 has also been shown to bind cholesterol[44,45]. It seems that the NPC1 protein could be cholesterol-regulated, if not acting as a cholesterol transporter. And indeed, NPC patient cells show a striking accumulation of unesterified cholesterol in the endosomal/lysosomal system. This has been used for clinical diagnosis of NPC using filipin[46], a mixture of fluorescent compounds that form specific complexes with unesterified cholesterol.

An exemplary staining of control and NPC patient fibroblasts used in our laboratory is shown in Figure 1.5.

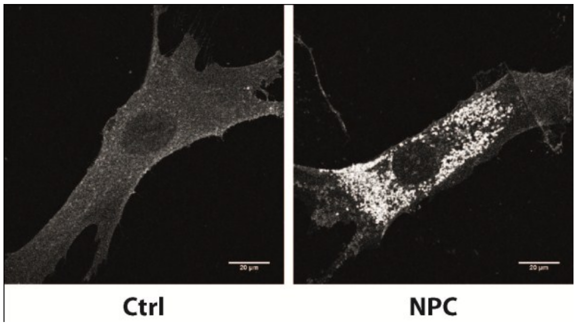

Figure 1.5 Cholesterol accumulates in NPC disease. Filipin staining of control and NPC patient fibroblasts.

On the other hand, mutagenesis studies have demonstrated a primary role of the SSD domain in sphingolipid distribution[47], indicating cholesterol accumulation is a secondary event in the NPC disease. Indeed, other diseases such as cystic fibrosis, most sphinoglipidoses and Huntington's disease show a lysosomal cholesterol accumulation even though the NPC1 protein remains functional[48–50]. Additionally, cholesterol lowering therapies are not of clinical benefit to NPC patients[51] and cholesterol has been shown to be transported out of Npc1$^{-/-}$ late endosomes / lysosomes through other mechanisms[52,53]. All these facts point toward a secondary role of cholesterol in NPC disease. In the search for other potential causative substances, it becomes clear that the materials stored in NPC are highly complex and belong to different classes of lipids. Apart from cholesterol, sphingomyelin, higher glycosphingolipids as well as sphingosine accumulate[54]. The reason for this collective accumulation is thought to be a trafficking block at the lysosomal stage so that lipids and proteins cannot leave the endolysosomal system to reach the Golgi aparatus[55]. It remains unclear which of these substances is the offending metabolite. Several hints point toward glycosphingolipids, particularily the observation that inhibition of glycosphingolipid synthesis through the amino sugar miglustat reverses the NPC trafficking defect[56]. Miglustat is the only approved therapy for NPC disease up to now. Other studies indicate that Sph accumulation is the first detectable biochemical change after NPC1 inactivation and that addition of free Sph or dhSph to cells is enough to induce the NPC phenotype[57]. This Sph accumulation is then followed by a defect in calcium homeostasis of the acidic stores, leading to chronically lower calcium concentrations, which in turn leads to defective vesicular fusion and accumulation of storage materials in the endosomal compartment[57]. This theory is supported by the fact that correcting the calcium phenotype through agents like curcumin reverses the cellular lipid storage and increases the lifespan of NPC mice[57]. The purpose and regulation of the NPC1 protein still remain unclear and further studies are needed to elucidate its cellular function, but strong hints point towards the importance of Sph and acidic store calcium homeostasis in this disease.

1.3. The acidic compartment is a new player in intracellular calcium signaling

Ionic calcium has long been recognized as an important cellular second messengers controlling a wide variety of cellular processes, such as neuronal transmission, insulin secretion, muscle contraction and proliferation, to name a few[58]. This diversity of different signals is possible because cells possess a number of different receptors and channels which react to and conduct calcium ions (see Figure 1.6). The cytoplasmic calcium concentration in resting cells is maintained at around 50 - 100 nM, but this is rapidly increased by activation of plasma membrane calcium channels, which lead to calcium influx from the extracellular space where the calcium concentration averages around 1.6 mM. Some of these channels react to membrane depolarization (such as voltage-gated calcium channels VGCC), whereas other plasma membrane calcium channels react to empty intracellular calcium stores and refill them without affecting cytosolic calcium (such as the ORAI channels). The mammalian transient receptor potential (Trp) channels are another family of calcium channels found mainly at the plasma membrane. The Trp channel family consists of 28 channels divided into six sub-families which are all activated either by chemical stimuli through molecules such as diacylglycerol or through physical stimuli like heat, low pH or mechanical stress[59].

Calcium is also stored in intracellular organelles, most prominently the ER and the sarcomere in muscle cells, which can reach calcium concentrations of 100 – 800 µM[60]. Second messengers such as *myo*-inositol 1,4,5-trisphosphate (InsP$_3$) or cyclic ADP-ribose (cADPR) act on calcium channels in the ER, namely the InsP$_3$-receptor and the ryanodine receptor (RyR) respectively and release the calcium into the cytoplasm (see Figure 1.6). Unlike the well-studied ER, the acidic compartments were only later discovered to act as intracellular calcium store. Measurements on MDCK cells in 1996 showed an increase in cytosolic calcium after a glycyl-L-phenylalanine 2-naphtylamide (GPN) induced osmotic lysis of acidic vesicles[61]. Since then, the concentration of calcium in acidic stores (which increases with decreasing pH during the maturation of endosomes) has been measured to have values in the range from 400 – 600 µM in lysosomes[62].

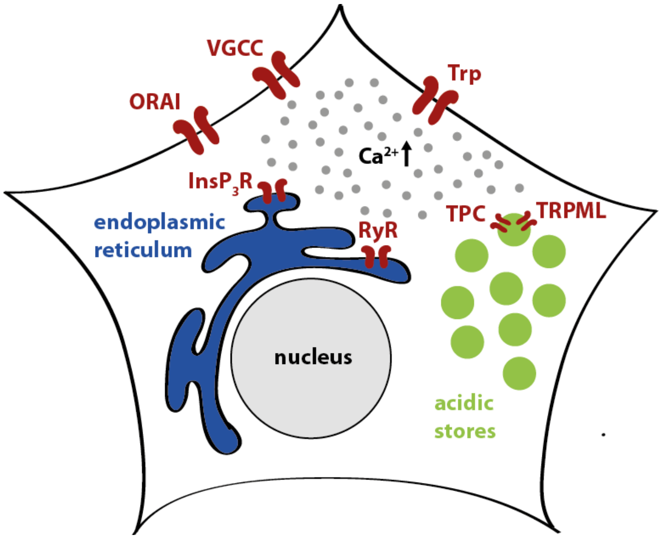

Figure 1.6 Schematic representation of the most important cellular calcium channels.

Not all the components involved in lysosomal calcium homeostasis have been identified yet, but several calcium releasing channels have been characterized: a group of three channels with homology to the Trp channel family are known to localize to the endosomal / lysosomal system: TRPML1, TRPML2 and TRPML3. All of them are non-selective cation channels which have been reported to be activated by phosphatidylinositol 3,5-bisphosphate ($PI(3,5)P_2$)[63]. The other, recently discovered family of acidic compartment calcium channels comprises two two-pore channels (TPC1 and TPC2). TPC1 was first discovered in plants[64] and later shown to be the target of the calcium-mobilizing agent nicotinic acid adenine dinucleotide phosphate (NAADP) in mammalian cells[65]. There is still some controversy around whether TPCs are actually the cellular targets of NAADP. Strong evidence obtained via different approaches, including reconstitution of purified TPC in artificial membranes[66], single-lysosome patch-clamp[67], and patch-clamp on plasma-membrane anchored TPCs[65] showed that TPCs were NAADP-gated Ca^{2+}-permeant channels. Two studies[68,69] challenged this notion by finding that a cell-permeant version of NAADP remained able to invoke calcium increase in fibroblasts from a TPC1/TPC2 double knockout mouse. However, this knock-out mouse may not have been generated properly, resulting in an N-terminal truncation and potential residual activity of the TPCs[70,71]. While NAADP should therefore not be discarded as the primary TPC activator, other ligands have also been found to stimulate TPC in a convergent fashion: Mg^{2+}, PI(3,5)P2 and p38/JNK kinases were shown to regulate TPC2 channel activity[70,72,73].

Functional calcium release from acidic stores is crucial for vesicle fusion along the endolysosomal system[74] and non-functional calcium homeostasis therefore contributes to the lipid storage phenotype in NPC. Mutations in proteins involved in acidic store calcium homeostasis cause severe diseases such as mucolipidosis type IV[75] or Hailey-Hailey disease[76]. It is therefore vital to study the mechanisms and regulatory steps involved in acidic store calcium filling and release in order to find treatments for these diseases.

1.4. The lysosome is a signaling hub involved in the initial steps of autophagy

The biological function of the lysosome was long reduced to merely the “trashcan” of the cell, where cellular material is degraded through the action of lysosomal hydrolases and lipases. This ‘endpoint’ way of thinking was recently challenged when several observations were made showing that the cell actively monitors lysosomal content and changes transcriptional activity according to this information. It was shown that the mechanistic target of rapamycin kinase complex (mTORC1), which is a master regulator of cellular growth, associates with the lysosomal surface[77] to sense amino acid levels in the lysosome via the vacuolar H^+-ATPase (v-ATPase)[78]. In starvation conditions, when amino acid levels are low, mTORC1 is dissociated from the lysosome and thereby inactive[78] (see Figure 1.7).

This inactive mTORC1 can no longer phosphorylate the transcription factor EB (TFEB), allowing it to translocate to the nucleus[79]. TFEB was identified as a transcriptional regulator of a whole gene network involved in lysosomal biogenesis and autophagy termed CLEAR (coordinated lysosomal expression and regulation)[80]. Functionally, TFEB induces biogenesis of lysosomes and autophagosomes, enhances their fusion and promotes degradation of their cargo. Other lysosomal functions, such as lysosomal exocytosis, are also influenced by TFEB[81].

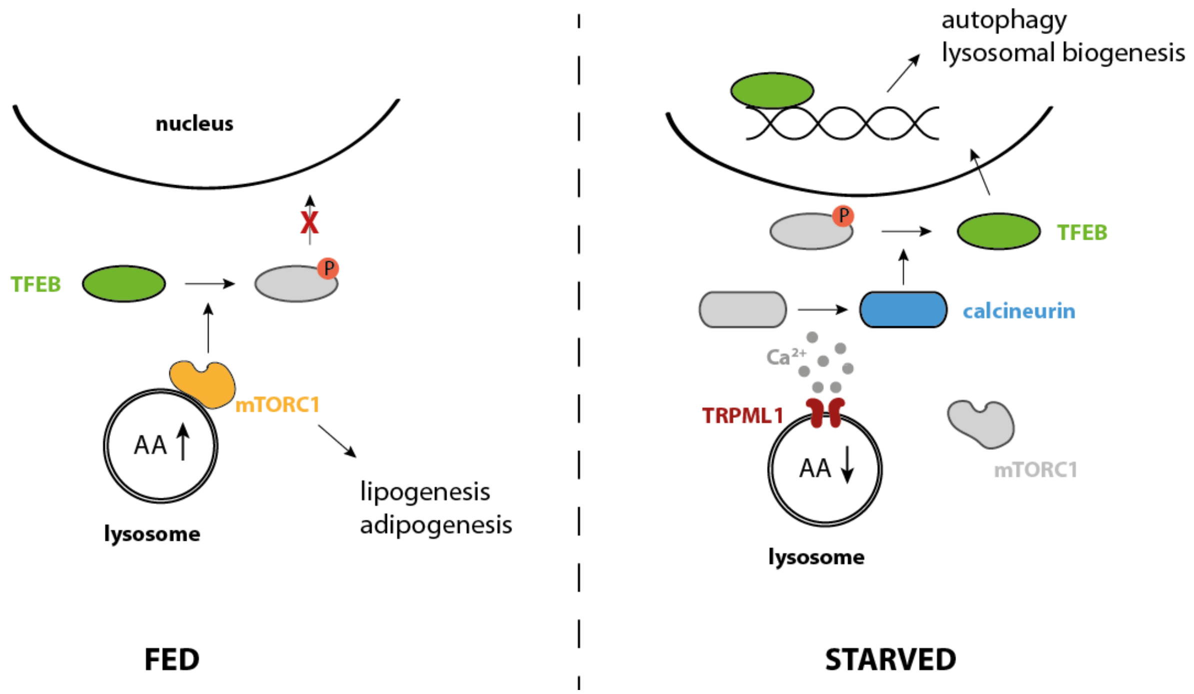

Figure 1.7 Schematic representation of the egulation of TFEB in the context of cellular metabolism. Figure is adapted from [82].

The mechanism by which mTORC1 inactivation leads to TFEB nuclear translocation was recently identified and includes lysosomal calcium release through the actions of TRPML1, which activates the phosphatase calcineurin leading to dephosphorylation and nuclear translocation of TFEB[82]. These new discoveries place the lysosome at the center for sensing the metabolic state of the cell and for regulating cellular processes accordingly. They also open new therapeutic avenues for treating lysosomal storage diseases or metabolic disorders. For example, overexpression of TFEB has already yielded promising results in diseases such as Pompe disease[83], Parkinson's disease[84], Alzheimer's disease[85] and Huntington's disease[86].

1.5. NPC1 and TPC2 are necessary for successful infection of host cells by the Ebola virus

The biological importance of understanding the NPC pathway as well as TPC dependent calcium signaling was recently highlighted by several findings which implicated a role of both proteins in filovirus infection. The Ebola virus (EBOV) as well as the Marburg virus (MARV) belong to the class of filoviridae, a family of enveloped, negative-stranded RNA viruses which infect humans and non-human primates and cause haemorrhagic fever with mortality rates of up to 90 %[87].

The 2013-2015 Ebola outbreak in West Africa with over 10 000 confirmed deaths[88] underlined the dire need to develop therapies, because there are currently no Ebola-specific treatments available[89]. Recently, however, several important steps have been made in the investigation of the molecular basis of Ebola virus infection (see Figure 1.8).

The binding of the virion to the host cell is dependent upon a single viral transmembrane domain glycoprotein (GP), the structure of which was recently identified[90]. GP consists of two subunits: a receptor-binding subunit GP1 and a membrane fusion subunit GP2, which are organized into trimeric spikes on the virion surface. Upon internalization into host cells via macropinocytosis[91,92], the GP is cleaved by endosomal proteases (cathepsin L, cathepsin B) to remove the heavily glycosylated C-terminal domain of GP1[90,93,94]. The remaining N-terminal domain of GP1 interacts with a host factor promoting dissociation of GP1 and GP2, driving GP2-mediated membrane fusion and subsequent release of the nucleocapsid into the cytoplasm[90,93,95].

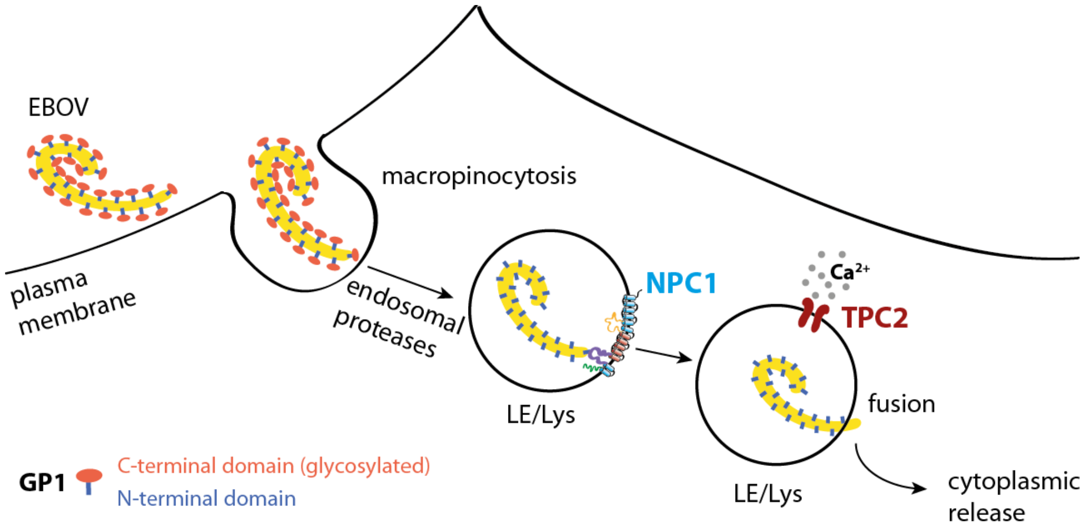

Figure 1.8 A model of EBOV entry. Figure is adapted from [96].

A genetic screen in human haploid cells recently identified several candidate proteins responsible for successful filovirus entry[97]: all six members of the homotypic fusion and vacuole protein-sorting (HOPS) complex, which is responsible for lysosomal function and fusion were identified along with the lysosomal transmembrane protein NPC1. This suggests that the lysosome plays a critical role in the late stages of viral entry. In parallel, it was shown that binding of the N-terminal GP1 to NPC1 is crucial for infection, and that small-molecule inhibitors of NPC-GP1 binding are successful in preventing EBOV infection[98]. These new findings open up new avenues for Ebola therapy by directly targeting the NPC1 protein. The importance of NPC1 in EBOV infection was further strengthened in follow-up studies identifying NPC1 as an intracellular filovirus receptor due to its ability to overcome species barriers: Expression of human NPC1 in non-permissive reptilian cells rendered them susceptible to filovirus entry and infection[42]. In the same study, the luminal loop C of the NPC1 protein (filovirus receptor domain in Figure 1.4) was shown to bind the proteolytically truncated GP1 domain of EBOV and proved necessary and sufficient for filovirus entry[42]. These findings were recently confirmed *in vivo*, showing that Npc1$^{-/-}$ and even Npc1$^{+/-}$ mice were protected from EBOV infection and that NPC1 was directly required for filovirus entry irrespective of its role in cholesterol homeostasis[99].

Aside from NPC1, other cellular processes have been shown to be crucial for successful EBOV infection. An siRNA screen on HEK293 cells identified several host cell genes which play critical roles during infection, most prominently a network of calcium or calmodulin dependent kinases[100]. Follow-up studies identified TPC2 to be necessary for successful EBOV entry[101]. The authors further demonstrate that drugs blocking TPC2 activity improve survival of EBOV infected mice, opening yet another avenue for Ebola-specific antiviral therapy.

1.6. Studying the specific contributions of lipids to cellular processes is challenging

Given the vast diversity of different lipid species, it is somewhat surprising that only some of them, for example certain diacylglycerol[102] and phosphatidic acid[103] species as well as phosphatidylinositol phosphates[104] and sphingosine-1-phosphate[105], are recognized second messengers with clear modes of action. Others are merely implicated in different cellular processes[19,106], without knowing their precise signaling effectors. Functions for many other known lipids are not elucidated yet. One reason might be that lipids are part of a complex network. They are transiently generated and quickly converted by a sophisticated lipid handling machinery consisting of hundreds of proteins[107].

Ideally, one would follow the localization and concentration of the investigated lipids in the cellular system with high accuracy. These requirements effectively restrict the experimental approaches to fluorescence microscopy or – if applicable – electrophysiology. However, well performing biosensors which would allow such precise monitoring only exist for a few lipids, such as diacylglycerols[108] and several phosphatidylinositol phosphates[109–113]. Most of these biosensors are based on translocation of a lipid binding domain, but these translocation-based probes recognize the respective lipid well at the plasma membrane and not at other organelles[114]. Following the cellular distribution of lipids through the use of fluorescently tagged lipids is problematic as well since they are easily mislocalized owing to the lipophilic properties of many fluorophores. To faithfully follow endogenous lipid behavior, it is essential to minimally interfere with the biophysical properties of the lipid molecules[115].

Another challenge in studying the biology of lipids is the need to specifically manipulate lipid levels in cellular systems. Simply adding lipids to the medium or feeding organisms with the lipids of interest may not lead to an intracellular elevation of the same lipid species because they may already be modified and/or degraded before reaching concentrations at which they would affect cellular signals. Standard molecular biology techniques such as overexpression or RNAi mediated knockdown of a key lipid metabolizing enzyme are not ideal because they require many hours to take effect. During this time, the cells may compensate by transcriptionally regulating other parts of the lipid signaling network. A faster method employs rapamycin-mediated translocation of constitutively active lipid metabolizing enzymes to certain organelles, generating a local pool of the lipid of interest. This method has been successfully applied to the study of phosphoinositide signaling[112,116–119]. However, rapamycin itself inhibits the mTOR kinase complex and thereby also perturbs cellular signals[120]. New developments in non-inhibitory rapamycin-analogues[121,122], light inducible translocation[123] or novel chemical dimerizers[124] already seek to circumvent this drawback. Another way to precisely elevate certain lipid species is to deliver biologically inert lipid precursors (‘caged’ lipids) to the cells and to release the lipids inside the cells by illumination with light (see chapter 1.6.1).

Lipids affect cellular signals by interacting with lipid binding proteins, either by recruiting proteins to certain membranes[125,126] or by binding and activating cellular receptors[127,128], yet studying the interactions between lipids and proteins remains challenging. Very few tools allow for a large-scale mapping of lipid binding proteins. Two such screens were performed using lipid arrays on solid support. First, a phosphatidic acid derivate was coupled to an agarose-based matrix and incubated with brain cytosol[129]. Proteins which showed suppressed binding in presence of soluble phosphatidic acid were identified by mass spectrometry and included several proteins involved in intracellular traffic such as coatamer, Arf and kinesin. A more recent screen used an array of over 50 lipids immobilized on nitrocellulose, probed the binding of over 170 tandem-affinity purification (TAP) tagged yeast proteins and identified 530 distinct lipid-protein interactions[130]. This approach works well to capture proteins interacting with the lipid headgroup, but due to the solid support, the lipids are not present in their native state and cannot interact with deeper binding pockets of the proteins.

To overcome this drawback, a microarray was established where lipids were presented on liposomes. The binding preferences of fluorescently tagged protein lysates to 120 liposomal membranes with different lipid compositions have been monitored by automated microscopy[131]. In another approach, lipids binding to 13 TAP-tagged yeast lipid transfer proteins expressed at endogenous levels were identified by TLC and mass spectrometry after affinity purification. The results show that two oxysterol binding protein homologs (Osh6 and Osh7) bind phosphatidylserine and mediate its transport from the ER to the plasma membrane[132]. Regrettably, all these methods are restricted to cytosolic proteins, because the detergent-based solubilization of the membrane necessary for integral membrane proteins also disrupts specific protein-lipid interactions. Given the wide variety of cellular lipids as well as integral membrane proteins, it is likely that specific interactions of lipids with membrane proteins occur within the lipid bilayer. One such example is the regulation of p24, an integral membrane protein of COPI vesicles, by a single molecular species of sphingomyelin (SM18:0). The interaction of SM18:0 with p24 has been pinpointed to a four-residue motif within the transmembrane domain[133]. This highlights the need to systematically map protein-lipid interactions and to include integral membrane proteins in those screens. One promising avenue is the application of photoactivatable and clickable (bifunctional) lipid analogues, which allows for a proteome-wide screening of lipid binding proteins in living cells (see chapter 1.6.2).

1.6.1. Caged lipids are useful tools for studying intracellular signaling

One way to increase the concentration of a specific lipid in living cells with high accuracy in time and space is to liberate caged lipids by a flash of light. We have recently reviewed caged lipids with respect to design considerations as well as applications in biological systems[134] and the key aspects are only briefly discussed here. Caged lipids are obtained by masking a key group essential for the activity of the lipid with a photoremovable protecting group through chemical synthesis, thereby rendering the lipid inactive. The hydrophilic headgroup of lipids is crucial for interactions with the cellular machinery, and the functional groups (alcohol groups, amino groups, phosphates) are easily accessible for chemical modification. All reported caged lipids have therefore been modified at the headgroup, using either nitrobenzyl-derived or coumarin-derived caging groups[134] (see Figure 1.9).

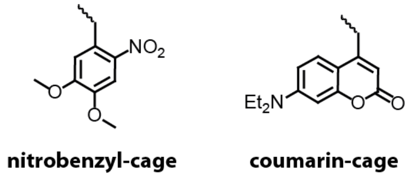

Figure 1.9 Chemical structure of two commonly used caging groups. 4,5-dimethoxynitrobenzyl (DMNB) and *N*,*N*-diethylaminocoumarin (DEAC).

The main differences in the cages result from their respective photophysical properties: the absorption spectra of coumarin-groups are red-shifted with respect to nitrobenzyl groups. This enables successful uncaging using the 405 nm laser of a standard microscope setup, while nitrobenzyl-modified lipids have to be uncaged with a special UV-laser because their absorption maximum lies at 365 nm[134]. Irradiating living cells at these wavelengths could lead to photodamage, which needs to be controlled for. Another difference is the inherent fluorescence of the coumarin groups which allows monitoring the loading of the compound either by fluorescence microscopy or via TLC. The photochemical mechanism of uncaging is another, fundamental distinction between the caging groups. While nitrobenzyl groups decay via an *aci*-nitro intermediate[135], coumarins are most likely cleaved by solvent-assisted photo-heterolysis[136], leaving different byproducts which could potentially influence the observed signal. It is therefore good practice to include a positive control compound using a caging group with a different uncaging mechanism. Another key consideration in the application of caged lipids is the delivery of the lipid to living cells. Due to their hydrophobic nature, caged lipids sometimes require addition of mild, non-ionic detergent. This does not hold true for uncharged lipids with only one hydrophobic tail (such as sphingosine or mono-acylglycerols), which cross the plasma membrane spontaneously without any detergent. The presence of charged groups on the lipids (such as phosphate, choline or ethanolamine) makes delivery over the plasma membrane impossible and requires more sophisticated delivery techniques. Microinjection is not recommended because it results in severe disturbances to the membrane which could make it impossible to observe any naturally occurring signaling events. The best strategy is to mask the charges on the headgroup by chemically attaching bioactivatable protecting groups such as butanoyl-, acetoxymethyl- or S-acetyl-thioethyl-groups, rendering the molecule neutral. After successful passing of the plasma membrane, intracellular esterases cleave these protecting groups, restoring the original charges. The biological activity of the lipid is then restored after uncaging with a flash of light (see Figure 1.10).

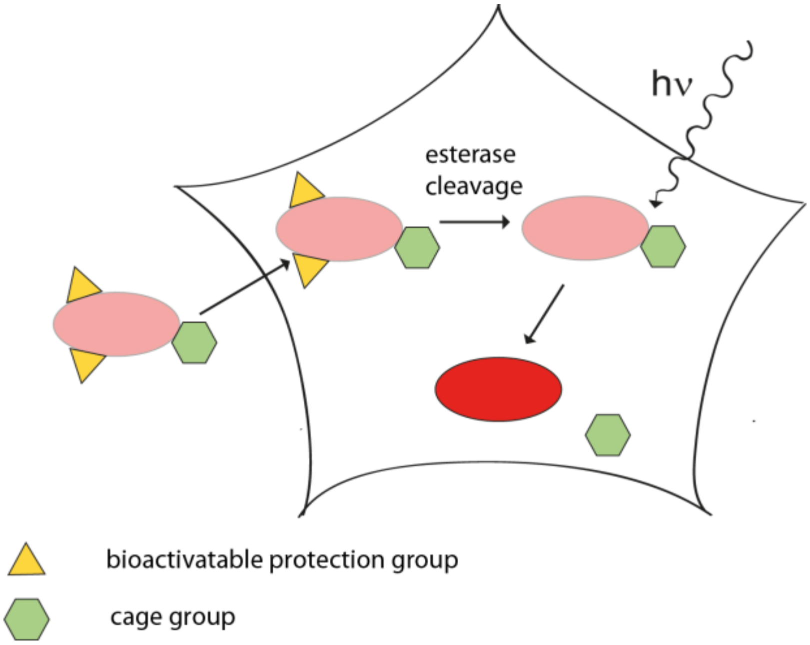

Figure 1.10 Schematic diagram illustrating the application of caged, membrane-permeant lipids.

Owing to the speed of lipid release after photo-uncaging, caged lipids are ideal tools to study highly dynamic processes in membrane biology in a non-invasive way. Somewhat surprisingly, so far only 20 individual lipids have been reported in caged from, and even fewer have found application in studying biological questions[134]. An important example is the caged version of sphingosine-1-phosphate, which was first synthesized and used by the Spiegel group[137] and later made commercially available. It proved crucial in distinguishing receptor-mediated S1P-dependent pathways from those which result from intracellular S1P targets[138–140]. These results illustrate that, once made broadly available, caged lipids have the power to answer many biological questions, especially those where high temporal and spatial resolution is important.

1.6.2. Proteome-wide identification of lipid-binding proteins by bifunctional lipids

In vitro methods to study protein-lipid interactions rely on either purified proteins or cell lysates and are therefore limited to soluble proteins. In order to develop new methods for identifying protein-lipid interactions in the native environment, several advances in chemistry were necessary. First, a covalent bond between lipid and protein is essential to preserve the lipid-protein complex during solubilization of membrane proteins. Such covalent bonds are created upon UV illumination of lipids modified with certain photoactivatable groups (Figure 1.11), which create a highly reactive intermediate (e.g. carbene or nitrene) and are able to insert into any chemical bond of the target proteins.

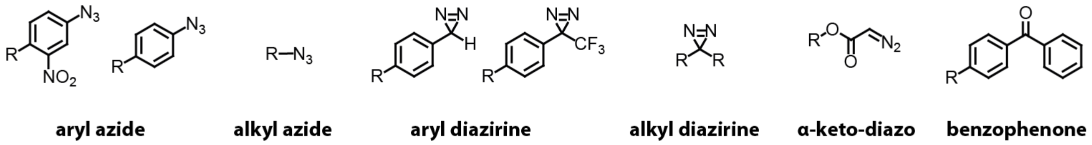

Figure 1.11 Photoactivatable groups used in photoaffinity labeling experiments.

Further requirements for such photoactivatable groups in use in the cellular system are mainly the stability in non-activating conditions, so that the reducing environment of the cell and cellular enzymes do not modify the group before photoactivation, as well as rapid photolysis rates in order to avoid long UV exposure times which are damaging to the sample. Additionally, the crosslinking reaction of the UV activated probes should proceed quickly and non-selectively with molecules in their direct environment, to increase specificity and reduce background crosslinking with small molecules such as water. Well-known photoactivatable groups which would fulfill these criteria such as benzophenones, aryl azides or aryl-trifluoromethyldiazirines are too large to be incorporated into small molecules such as lipids without significantly changing their physicochemical properties. Smaller groups such as alkyl azides were employed in early studies of photoactivatable lipids[141], but were later found to require too harsh photoactivation conditions to be useful in biological studies[142]. Alkyl diazirines however, show remarkable chemical stability even during peptide synthesis and incorporation into proteins in mammalian cells, as demonstrated by the application of alkyl diazirine-modified leucine and methionine for protein-protein crosslinking experiments[143].

The first lipids modified with alkyl diazirines were cholesterol[144] and sphingosine[145]. Both lipids were also radiolabeled by incorporation of ^3H to identify the captured protein-cholesterol or protein-sphingolipid complexes. One drawback of this design is that it does not allow for proteome-wide identifications, since every candidate protein has to be immunoprecipitated, purified and probed via autoradiography.

The other important advance in chemistry was the introduction of click chemistry by Sharpless, Finn and Kolb[146]. Especially Cu(I) mediated cycloaddition between alkyne and azide groups[147] (Figure 1.12) opened up new possibilities for modifying lipids.

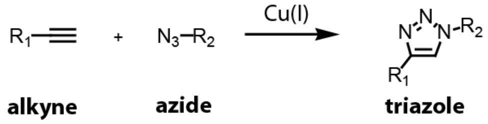

Figure 1.12 Copper(I) catalyzed alkyne-azide cycloaddition.

The alkyne group shows similar advantages to the diazirine group: it is small and interferes therefore only minimally with the structure of the modified lipid, it is stable in the cellular environment and unreactive with any naturally occurring functional group.

A combination of both the diazirine as well as the alkyne functionality on the same lipid gives a powerful tool which enables the identification of protein-lipid complexes in the natural environment. As the lipid is only modified with small additional functionalities, it closely mimics its natural counterpart in localization and protein interaction. These interactors are then captured by covalent crosslinking upon UV irradiation. The major advantage of such a bifunctional design is the fact that functionalization of the probe (e.g. with biotin for a subsequent avidin-mediated pulldown) happens after crosslinking to its interacting partners (see Figure 1.13). Therefore the bulky biotin modification does not inhibit protein-lipid interactions at all.

A second advantage is the versatility of the functionalization. The same photoactivatable and clickable lipid can be used to probe the subcellular localization of said lipid at different time points, thereby following the metabolism and traffic within the cells (Figure 1.13, right-hand side). This is achieved by crosslinking of the lipid to its interaction partners and subsequent fixing of the cells. This new covalent bond makes rigorous washing steps possible, which reduces the background due to non-crosslinked lipids. Furthermore lipid mobility in the membranes, which is known to occur even with aldehyde fixation techniques[148], is abolished by the covalent binding to large, crosslinked biomolecules. Bifunctional lipids are therefore best suited to faithfully display the subcellular localization of lipids, a challenge which has occupied the lipid biology field for decades[115].

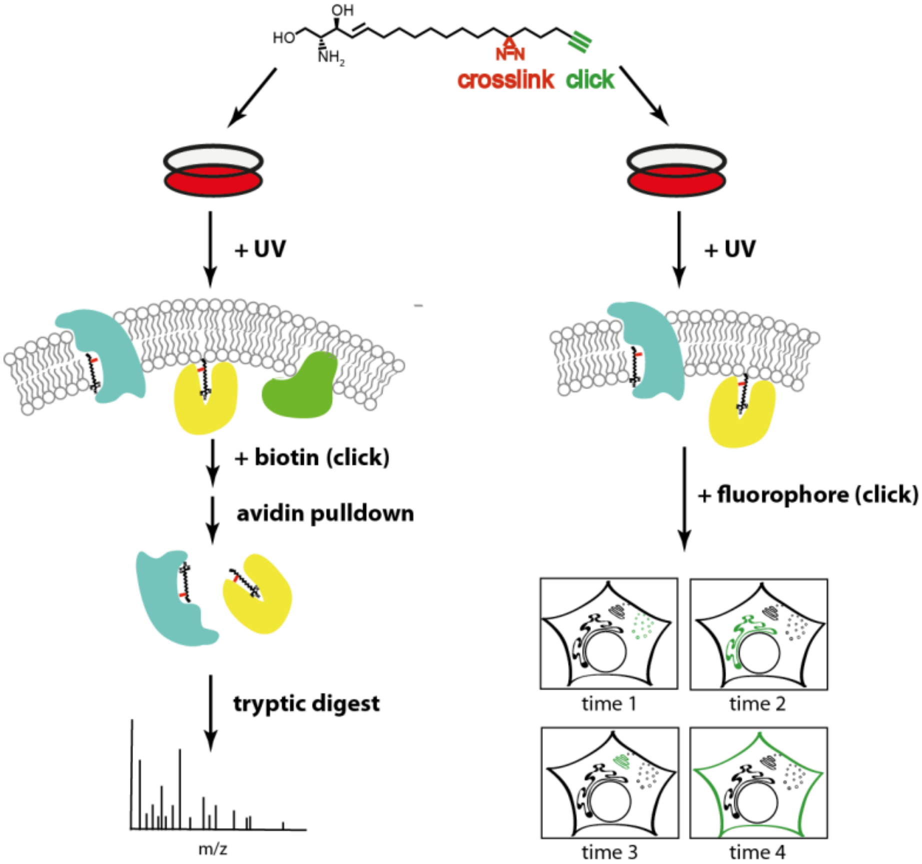

Figure 1.13 Application of bifunctional lipids for mass spectrometry and confocal microscopy.

So far, only few photoactivatable and clickable lipid species have been reported. A major reason for this is certainly the substantial effort necessary for the lengthy synthesis of each individual lipid species. The introduction of the diazirine group in particular suffers from poor yields of around 30 %[144,145]. The first reported bifunctional lipids were phenylazide- and benzophenone derived phosphatidylcholines (PC) with an alkyl azide as a click handle[149]. They were used to probe PC binding partners on mitochondrial inner membranes.

The first bifunctional lipid featuring the diazirine/alkyne combination was reported in 2009 with the application of a bifunctional cholesterol to map cholesterol-interacting proteins in living cells[150]. In stable isotopes of amino acid in culture (SILAC) screens, 265 proteins were identified which showed specific interaction with cholesterol as determined in competition assays. In a different approach, Haberkant et al.[151] used a bifunctional C15 fatty acid precursor, which upon feeding to cells readily incorporated into all glycerolipids, but not into sphinoglipids. Crosslinking, affinity purification and mass spectrometry revealed 105 high-confidence glycerollipid-binding proteins. Additionally, this study introduced the power of visualizing lipids using bifunctional precursors in whole organisms by imaging the glycerolipid distribution in *C. elegans*.

Another, very recent study employed a variety of different bifunctional lipids: arachidonyl-, stearoyl-, palmitoyl- and oleyl-containing endocannabinoids as well as bifunctional arachidonic acid to perform in-depth screens of the lipid interactome. Additionally, the geometry of protein binding on the lipid (e.g. interactions with the lipid headgroup vs binding of the lipid in a hydrophobic pocket) was probed by performing screens using precursors with varying position of the photoactivatable diazirine group (on the headgroup vs. on the lipophilic tail)[152]. Furthermore, the impact of different drugs on the lipid-interaction proteomes was profiled, showing the applicability of such bifunctional probes to map drug target and off-target effects as well as to identify new, potentially drugable proteins. The study progressed even further, screening functional ligands of these newly identified proteins (such as nucleobindin-1 (NUCB1)) and used these ligands to characterize the biochemical function of NUCB1 which is to facilitate transfer of *N*-acyl ethanolamides and *N*-acyl taurins to their respective metabolic enzymes[152]. The last study is an impressive example of the power of bifunctional lipids not only in discovering novel lipid-interacting and potentially drugable proteins, but also in elucidating the biochemical functions of these newly discovered proteins.

Aim of the thesis

Investigating the roles of lipids in cellular signaling is still limited by challenges such as the manipulation of lipid concentrations inside living cells or the identification of protein-lipid interactions. Sphingosine is a central lipid in the sphingolipid metabolic network, yet little is known about its signaling properties or its protein interactors other than metabolic enzymes. It has been implicated in apoptosis signaling and has been shown to accumulate in the lysosomal storage disorder Niemann-Pick disease type C, but the exact mode of action has not been elucidated so far. We envision that chemical biology can provide tools to overcome the difficulties faced in studying lipid signaling which will further the understanding of sphingosine mediated pathways and, eventually, lead to a treatment of Niemann-Pick type C.

The main aim of this work is to manipulate sphingosine levels in living cells and monitor the downstream effects. Caged lipids provide an elegant, non-invasive method to increase their concentration with high spatial and temporal precision, permitting the study of fast-acting signaling events such as calcium signaling. Therefore the synthesis of caged sphingosine, a positive control equipped with a different caging group as well as a caged version of a closely resembling lipid, dihydrosphingosine as a negative control will be a major synthetic goal. In the first part, sphingosine-induced calcium signaling will be investigated in HeLa cells, but the assay will later be transferred to fibroblasts derived from patients suffering from Niemann-Pick C, as it is known that Niemann-Pick C cells feature chronic sphingosine accumulation as well as defective acidic store calcium homeostasis.

In addition, we will improve on the bifunctional lipid technology so that protein interactomes of single lipid species can be captured. To this end, we will add a cage group to bifunctional sphingosine, characterize the resulting trifunctional probe and screen for proteins which uniquely interact with sphingosine. Furthermore, the trifunctional sphingosine will be a great tool for studying the subcellular localization and transport of sphingosine in living cells using pulse-chase experiments. This probe will be applied to the study of NPC patient fibroblasts in an attempt to find a biomarker for predicting the severity of symptoms in NPC patients based on the extent of Sph storage.

Chapter 2 - Results and Discussion

2.1. Caged sphingosine is a useful tool to investigate cellular signaling

The specific effects of Sph on intracellular signaling pathways are difficult to tease apart, mainly due to a lack of tools to precisely manipulate Sph levels in living cells. As with other biologically active lipids, traditional methods of lipid manipulation have drawbacks which make it impossible to study acute downstream signals of Sph (see chapter 1.6.). Exogenously added free Sph, for instance, is both quickly metabolized to Cer and subsequently higher sphingolipids and it is broken down via the S1P-lyase pathway before it reaches intracellular concentrations which are comparable to an endogenously occurring signal. Therefore, it is challenging to attribute a certain signaling outcome to the lipid added and to exclude contributions of up- or downstream metabolites. On the other hand, overexpression of Sph-producing enzymes such as ceramidases often takes days, during which time the cell may turn on compensatory mechanisms to maintain low Sph concentration inside cells such as the up-regulation of the S1P-lyase pathway. One way to overcome this problem would be to use small molecules which penetrate the cell membrane easily and then quickly act on these enzymes. However, only a few molecules are known to specifically act on sphingolipid metabolizing enzymes, and all of them have inhibitory action[153]. No small molecule activator of any of the five known ceramidases has been reported so far.

Another way to rapidly elevate Sph inside cells is to design caged variants of Sph, which circumvent ongoing sphingolipid metabolism and allow for the specific release of Sph during the experiment. The caging methodology is very successful and has been broadly applied to the field of neurotransmitters and other second messengers[154]. However, only two studies have ever reported the use of caged Sph. More than 15 years ago, Zehavi published the synthesis[155] and application of caged Sph and dhSph in dorsal root ganglion neurons[156]. The caging group was a first-generation nitrobenzyl group directly attached to the amino group of the sphingoid backbone, and uncaging was achieved by a xenon flash lamp with a bandpass filter of 365 nm ± 110 nm. Both Sph and dhSph showed a Ca^{2+}-activated inward rectifying current as measured by whole cell patch clamp[156]. These findings gave the first hint of a connection between sphingolipid and calcium signaling, but they have not been followed up. In the meantime, new caging groups with faster photolysis rates have been developed[157] and advances in microscope hardware make it possible to uncage at single wavelengths, thereby avoiding potential photodamage likely to result from the shorter UV wavelengths of a bandpass filter. In this project, we have made use of these advances and synthesized new versions of caged Sph to study Sph-mediated calcium signaling in living cells.

2.1.1. Design and synthesis of caged sphingosine

For this work we chose to use a *N,N*-diethylamino-coumarin (DEAC) group as the principal caging group for Sph. This group allows for efficient and rapid uncaging at longer wavelengths than commercially available nitrobenzyl-caging groups[158]. An additional advantage of the DEAC group is its fluorescent properties which permit monitoring of DEAC-caged Sph (Sph-Cou) on the microscope in order to check labelling of the cells. To exclude any contribution of the cleaved group to the observed signal, we synthesized as a positive control Sph caged with a 4,5-dimethoxy-nitrobenzyl (DMNB) group (Sph-NB). As a negative control dihydrosphingosine was chosen. dhSph is a naturally occurring, close structural analogue of Sph which differs only by one double bond from Sph. For the control experiments, dhSph was also caged with a DEAC group (dhSph-Cou).

In order to prevent recognition and metabolism of the caged coumpounds by the cellular machinery, the caging group must be located at the head group of the lipids. In addition, the only functional groups on Sph and dhSph available for synthetic chemistry are within the head group. We therefore chose to attach the cage groups to the amino functionalities of Sph and dhSph since the higher reactivity of the amino group compared to the alcohols allowed us to perform protection group-free synthesis. Figure 2.1 shows the synthetic protocols used for the three compounds used in this study.

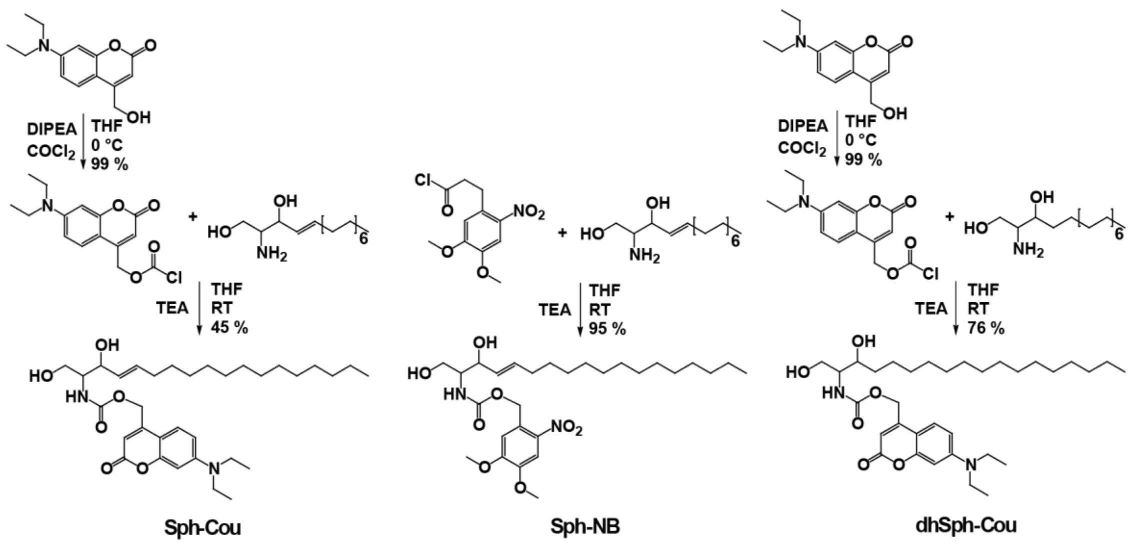

Figure 2.1 Synthesis of caged Sph derivates. *N,N*-diethylaminocoumarin-caged Sph (Sph-Cou), 4,5-dimethoxynitrobenzyl-caged Sph (Sph-NB) and *N,N*-diethylaminocoumarin-caged dhSph (dhSph-Cou).

We chose to link Sph/dhSph to the cage groups by a carbamate linker. This leads to CO_2 release after photolytic cleavage which drives the reaction forward by shifting the equilibrium to the side of the free lipid. The carbamate link was obtained by reacting the chloroformate derivates of the cage groups with the lipids at room temperature for 1 h, giving 45 – 95 % isolated yields. The target compounds were purified using column chromatography and the identity of the final caged lipids was confirmed using nuclear magnetic resonance (NMR) and high-resolution mass spectrometry (see chapter 3.2 and NMR spectra in Appendix A).

2.1.2. Caged sphingosine is stable in the cellular environment

We first used thin layer chromatography (TLC) to determine whether caged Sph was inert inside cells prior to uncaging. HeLa cells were incubated with 2 µM Sph-Cou for different time periods and some samples were subsequently illuminated with a mercury arc source equipped with a 400 nm highpass filter for 2 min. The cells were pelleted and the cellular lipids were extracted according to the protocol developed by Thiele's group[159], using a mixture of chloroform / methanol / acetic acid. The extracts were developed on silica TLC plates and visualized using the fluorescence of the coumarin group. Figure 2.2 shows a time-dependent uptake of intact Sph-Cou into cells. As expected, higher intensities were observed for longer incubation times. Photocleavage was observed as a drop in intensity for each +UV condition. Comparing the intensities of the non-irradiated with the irradiated bands, we estimated the extent of the photoreaction in this setup at 70 %.

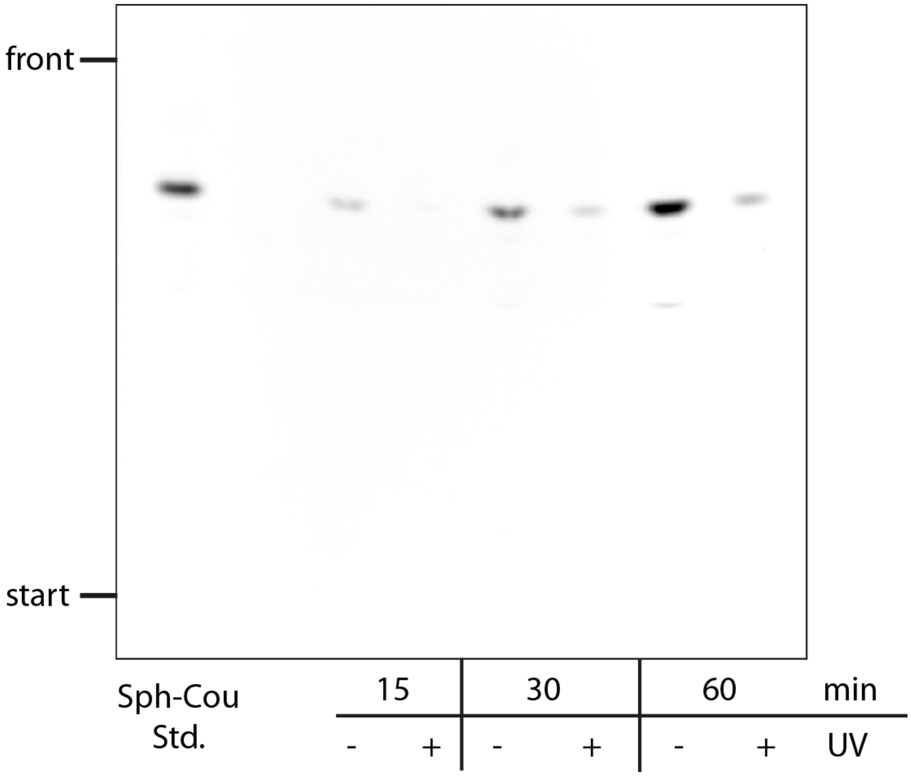

Figure 2.2 Stabilty of caged Sph in cells. TLC analysis of lipid extracts of HeLa cells incubated with 2 µM Sph-Cou. The background was subtracted using Fiji software.

Most importantly, Figure 2.2 shows no additional DEAC-labelled lipids, even with one hour incubation periods. This indicates that the Sph-Cou is stable in the cellular environment and that the free alcohol groups on the Sph headgroup did not undergo further modification (for example with phosphates or cholines) by any sphingolipid metabolizing enzyme.

However, this experiment does not rule out the possibility that the carbamate bond of Sph-Cou could have been cleaved by cellular enzymes. The loss of the coumarin group would make the resulting lipids invisible on TLC. To obtain a quantitative estimate of the Sph concentration inside cells, we subjected cellular extracts of Sph-Cou treated cells to lipidomic analysis as follows: Cells were labelled with 2 µM Sph-Cou for 15 min and subjected to UV treatment as described above. As controls, non-labelled HeLa cells as well as labelled but non-UV treated HeLa cells were collected. C17 standards were added to the cells for normalization after the extraction. Cellular lipids were extracted using a one-phase pyridine extraction protocol[160] to minimize loss of S1P and dhS1P, and were derivatized with the fluorescent label 6-aminoquinolyl-*N*-hydroxysuccinimidyl carbamate (AQC)[161]. The sphingoid bases were analyzed on a TSQ Vantage and their amounts were normalized to their C17 counterparts.

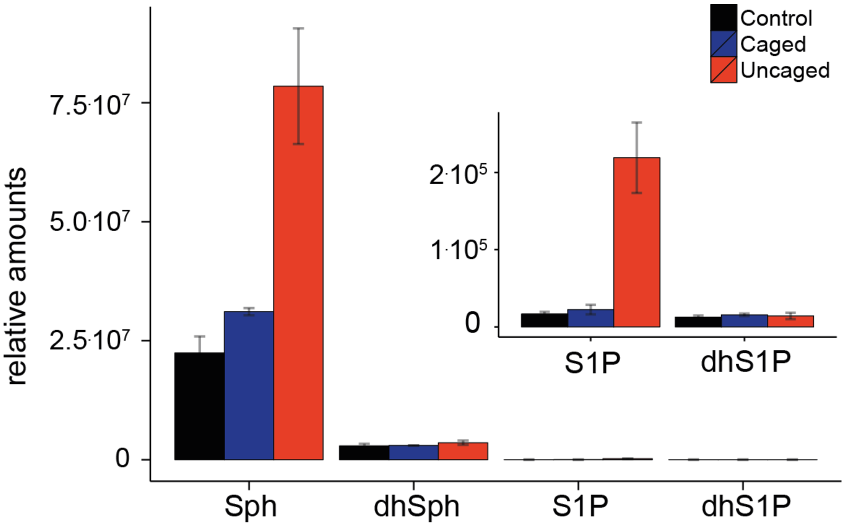

Figure 2.3 Comparative lipid analysis by mass spectrometry shows a specific increase in Sph upon uncaging. Values are normalized to the internal standards. Mass spectrometric analyses were perfomed by Auxiliadora Aguilera-Romero (University of Geneva, Switzerland).

Figure 2.3 shows the relative amounts of Sph, S1P, dhSph and dhS1P detected in control, non-UV treated (caged) and UV-treated (uncaged) conditions. The stability of the caged Sph in the cells was confirmed because comparable levels of Sph were measured in control and non-UV treated conditions, indicating that no cleavage of the carbamate linkage of Sph-Cou took place. Additionally, incubation with Sph-Cou did not perturb the lipid homeostasis in the cells because all investigated lipids showed similar concentrations compared to control conditions. Upon illumination of cells incubated with Sph-Cou, Sph levels were found at 3.4 times as high than in control samples. This increase was specific for Sph and was not observed for dhSph. The levels of S1P, however, increased in UV-treated conditions to $2 \cdot 10^5$ a.u., which corresponded to a 9.6 fold increase over control. We attributed this increase to ongoing metabolism during and after the uncaging reaction, which was carried out using a mercury arc source for 2 min. This comparably long time was necessary to ensure complete uncaging of all cells in this setup. To minimize metabolism, cells were kept on ice throughout the experiment, however it seems that the time for the uncaging reaction as well as the following steps (collection of the cells and extraction of the lipids) was long enough that phosphorylation reactions occurred to a significant extent even at 0 °C. The magnitude of the S1P increase (9.6 fold vs 3.4 fold for Sph) is explained by the generally low abundance of S1P in cells. Therefore, even if only a small portion of the liberated Sph was converted to S1P it resulted in a high increase.

2.1.3. Sph release after uncaging transiently increases cytoplasmic calcium levels

Intracellular calcium signaling has been intensively studied for a long time[162]. This has led to the development of a wide variety of different probes able to sense calcium concentrations inside cells[163,164]. The main types are small-molecule-based fluorescent calcium indicators, and genetically encoded, protein-based calcium sensors. In this work, especially with regards to eventually studying NPC-patient derived cells which cannot easily be transfected, we chose to work with a small-molecule based dye, namely Fluo-4 (Figure 2.4), which is delivered to cells using a lipophilic AM-ester modification that allows it to pass the plasma membrane[165]. Intracellular esterases then cleave off this modification and restore the active calcium sensing molecule. Fluo-4 undergoes fluorescence enhancement upon binding to Ca^{2+} [165]. An increase in free cytoplasmic calcium is therefore reported by an increase in Fluo4 fluorescence intensity.

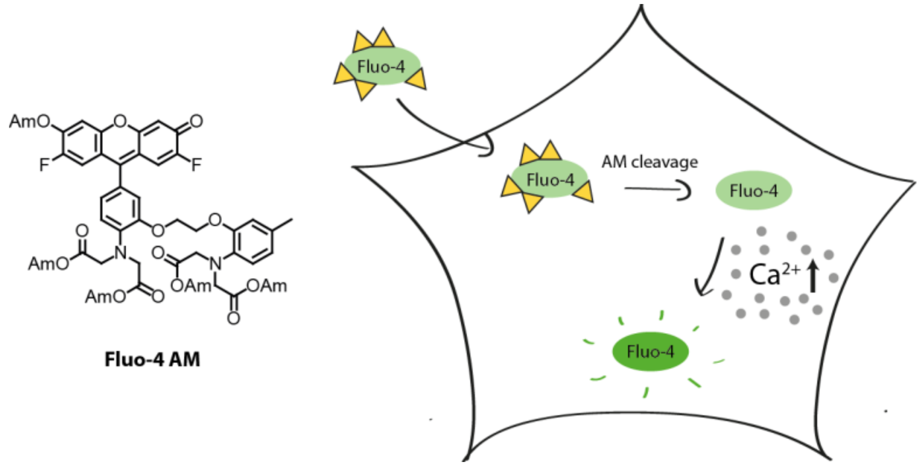

Figure 2.4 Fluo4-AM is an intensiometric cytoplasmic calcium indicator.

To check whether a sudden release of Sph following uncaging affects the cytoplasmic calcium concentration, HeLa cells were labelled with Fluo-4 for 30 min to allow for sufficient esterase cleavage as indicated by the manufacturer's instructions. Cells were incubated with Sph-Cou for 15 min before being put under the microscope. The uncaging experiment was performed on a confocal microscope by acquiring a baseline of 10 s before uncaging with a 405 nm laser

(375 nm laser for Sph-NB) in a local, circular area (~ 9 µm^2) inside the cell for 3s for Sph-Cou and dhSph-Cou and for 6 s when Sph-NB was used. This microscope setup allowed for much shorter uncaging times compared to the whole-dish uncaging setup used for TLC and lipidomic experiments (chapter 2.1.2.). This should minimize the impact of any post-uncaging metabolism. The fluorescence of the Fluo-4 indicator after uncaging was monitored at a frequency of 1 frame per second. Cells loaded with Sph-Cou or Sph-NB responded with an immediate (1-5 s) and transient increase in cytoplasmic calcium, whereas neighboring, non-irradiated cells did not respond at all. This illustrates the high specificity in location that is possible with caged lipids. Figure 2.5a shows exemplary time-lapse confocal microscopy images of Fluo4-labelled HeLa cells after Sph-Cou in the indicated area within the cells. The experiments were repeated on different cells some distance away from the previously examined cell, so that only 4-5 cells were imaged in the same LabTek well. Whole-cell fluorescence intensity values of all uncaged cells were measured using the FluoQ macro for Fiji[166] and averaged using R[167].

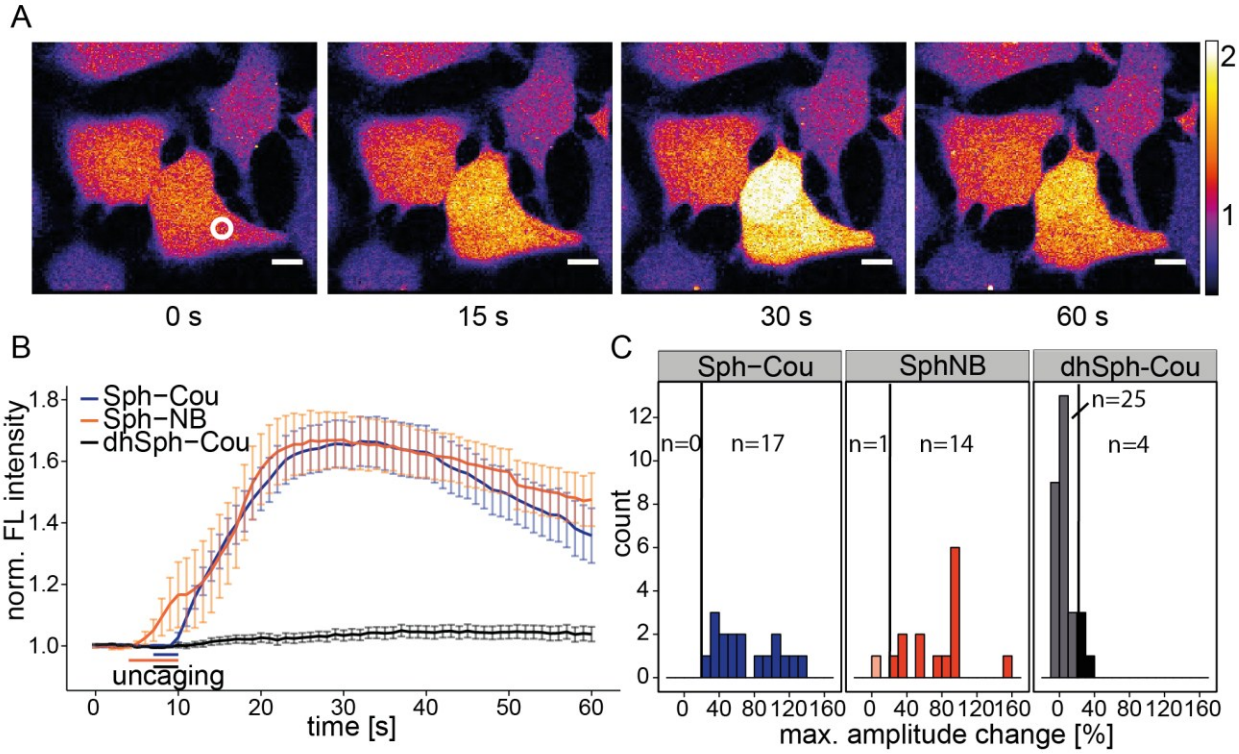

Figure 2.5 Local uncaging of Sph leads to calcium transients. A) Time-lapse confocal microscopy images of Fluo-4 labelled HeLa cells. B) Mean Fluo-4 fluorescence traces of cells loaded with Sph-Cou (17 cells), Sph-NB (15 cells), and dhSph-Cou (29 cells). C) Histogram of the maximum single-cell amplitudes. The threshold for responding cells (vertical line) was set at 20 % amplitude increase over baseline.

Figure 2.5b shows the mean Fluo-4 intensity over time with the standard error of the mean plotted as error bars. The calcium increase after Sph-Cou uncaging was also observed with the positive control Sph-NB. The only difference was the time of uncaging with was 6s for Sph-NB due to different photocleavage reactions. This resulted in a slightly slower onset of the response, which is partly explained by stronger bleaching of Fluo-4 when the 375 nm laser was used. On the other hand, the negative control compound dhSph-Cou did not evoke a calcium signal upon uncaging, indicating that the irradiation itself is not contributing to the increase in Fluo-4 fluorescence intensity. Furthermore, this illustrates that the Sph handling machinery follows such tight structural specifications that even a close analogue did not elicit a calcium signal. The promptness of the calcium increase seconds after Sph uncaging was a first hint that the observed response is due to Sph and not a downstream metabolite, which would take time to form.

To analyze single cell responses in more detail, the maximal amplitudes of the intensity traces of each irradiated cell were extracted and plotted in a histogram fashion (Figure 2.5c) with a threshold for responding cells set at 20 % increase over baseline. While all cells responded with Sph-Cou, less than 15 % (4 out of 29 cells) responded under control conditions (dhSph-Cou). Moreover, under control conditions, the few responding cells gave rise to markedly reduced amplitudes, further demonstrating the validity of dhSph as a negative control compound in this experiment.

To further ascertain that Sph is indeed the effector of this signal, we had to exclude any contribution of sphingosine-1-phosphate (S1P) formed post uncaging, as S1P is a potent calcium-mobilizing signaling lipid itself[138,168,169]. First attempts to silence both variants of the sphingosine kinase SK1 and SK2 using RNAi approaches were unsuccessful because cells did not survive the transfection. This is not particularly surprising as the sphingosine kinase/S1P lyase pathway is the only known way to degrade sphingolipids. A knockdown of the sphingosine kinases would lead to an accumulation of sphingolipids of which especially Sph and Cer are known to promote apoptosis[12]. We therefore turned to using several small molecule inhibitors of sphingosine kinases (Figure 2.6).

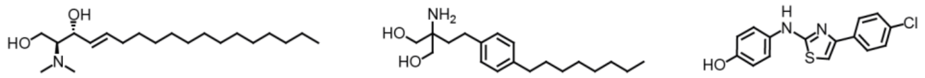

DMS **FTY720** **SKI-II**

Figure 2.6 Chemical structures of sphingosine kinase inhibitors.

1) Dimethylsphingosine (DMS) is a natural sphingosine analogue in some cancer cells and a competitive inhibitor of both sphingosine kinases with IC 50 values of 60 µM for SK1 and 20 µM for SK2[170–172]. However, it has been shown to have several non-specific off-target effects[173,174].

2) FTY720 is another sphingosine analogue, also known as Fingolimod, an immunosuppressant approved for treatment of multiple sclerosis. Its active, phosphorylated form acts on the S1P-receptors (S1PR), leads to S1P-R degradation and reduces circulating levels of T-lymphocytes[175]. Additionally, there is evidence that unphosphorylated FTY720 is an inhibitor of the catalytic activity of SK1[176].

Both of these described inhibitors would compete with the uncaged Sph for the binding to SK1 or SK2, therefore we also chose a third, non-competitive inhibitor.

3) SKI-II is not a Sph analogue and inhibits both SK1 and SK2, but is not active for other kinases. It acts as a mixed inhibitor for Sph and ATP binding on SK1[177], however its action on SK2 has not yet been studied.

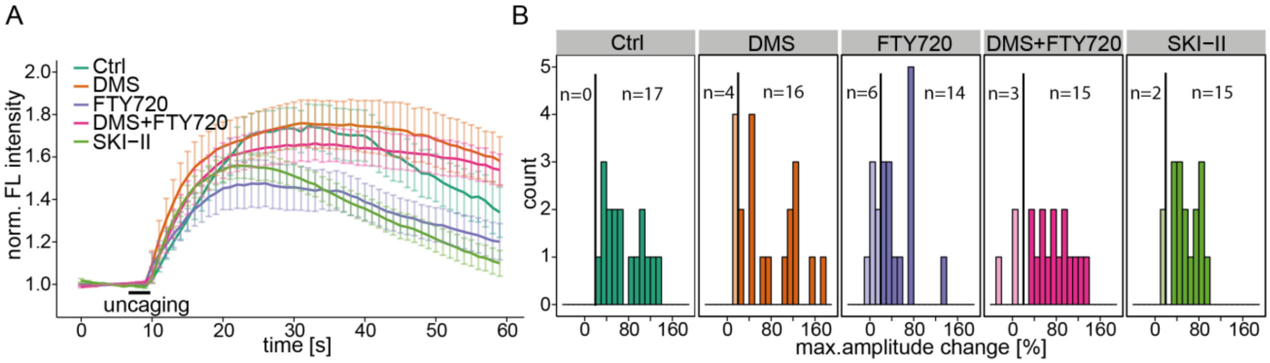

Figure 2.7 Inhibition of Sph kinases. A) Mean fluorescent traces of HeLa cells with and without SK-inhibitors. B) Histogram of the maximum amplitudes (20 % threshold, vertical line).

Figure 2.7 presents the data for this set of experiments. It can be seen that HeLa cells treated with these inhibitors exhibited similar calcium traces with respect to onset and amplitude of response compared to untreated cells, indicating that the uncaged Sph and not its S1P metabolite was responsible for eliciting this calcium response. Single cell analysis in Figure 2.7b showed slightly reduced response rates in the case of treated cells for all three inhibitors compared with untreated cells. This effect could stem from off-target effects of these inhibitors In spite of the minor effect of these inhibitors on calcium amplitudes, we concluded that rapid release of Sph directly leads to a transient increase in cytoplasmic calcium without involving S1P.

Addition of free Sph to the medium did not evoke calcium transients at concentrations of up to 5 µM. However, concentrations of free Sph greater than 6 µM killed cells frequently. The reasons for the lack of calcium response upon stimulation with free Sph have not been experimentally addressed. We hypothesize that cells have mechanisms for preventing the uptake of too high concentrations Sph. Any added lipid would also be subject to immediate metabolism (especially degradation through the S1P-lyase pathway). Only a rapidly generated Sph increase inside cells would lead to the observed calcium response.

2.1.4. Sph-induced calcium release originates at the acidic stores

To determine how the increase in cytosolic calcium levels upon Sph release was achieved and where in the cell the calcium was released from, we performed several inhibition experiments: First, we complexed extracellular calcium by changing the medium to calcium-free buffer supplemented with 0.1 mM ethylene glycol tetraacetic acid (EGTA) and added 5 mM Ni^{2+}, which blocks plasma membrane calcium channels in an unspecific way (PM block).

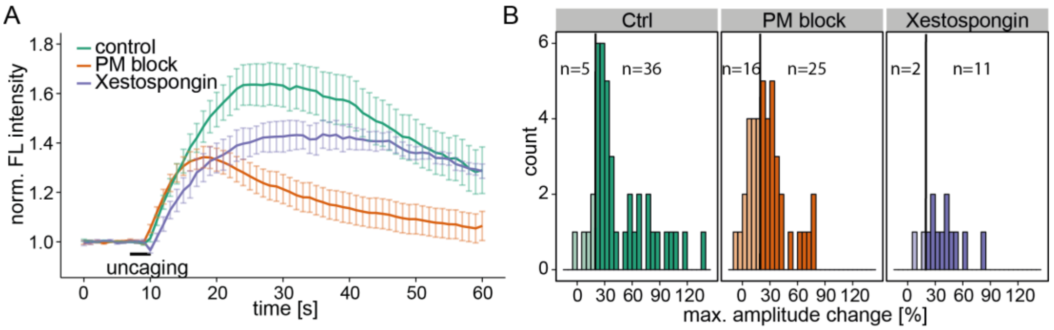

Figure 2.8 Investigating the source of Sph-induced calcium. A) Mean fluorescent traces of HeLa cells in control conditions (41 cells), in conditions blocking the plasma membrane calcium channels (PM block, 41 cells) or by blocking the $InsP_3$ receptors at the ER using Xestospongin C (25 µM, 13 cells). B) Histograms of the maximum amplitudes with a baseline of 20 %.

We performed uncaging experiments under these conditions and observed that cells still reacted to the increase of Sph with calcium transients (Figure 2.8). Even though the mean amplitude of the calcium response was reduced and the response rate (derived from single cell maximum amplitudes, Figure 2.8b) was at 61 % in PM block conditions compared to 88 % in control conditions, the initial (0 – 6 s after uncaging) increase in calcium is identical to control conditions, suggesting that influx of calcium from the outside is not the primary route. It might, however, be required for propagation of the signal via calcium induced calcium influx through plasma membrane channels. This could account for reduced amplitudes and response rates in PM block conditions.

In a separate experiment, the contribution of ER calcium store to the calcium response was investigated by using an inhibitor of the inositol trisphosphate receptor, Xestospongin C[178]. Uncaging Sph under these conditions led to similar calcium signals with only slightly reduced amplitudes but comparable response rates (Figure 2.8) to cells without inhibition. This suggested that the inositol trisphosphate receptor was not involved in Sph-induced calcium release.

To further strengthen the hypothesis that ER calcium was not released after Sph uncaging, we performed pre-release experiments. Adding ATP to the medium at t = 10 s stimulated G-protein coupled receptors and subsequently ER calcium was released (Figure 2.9).

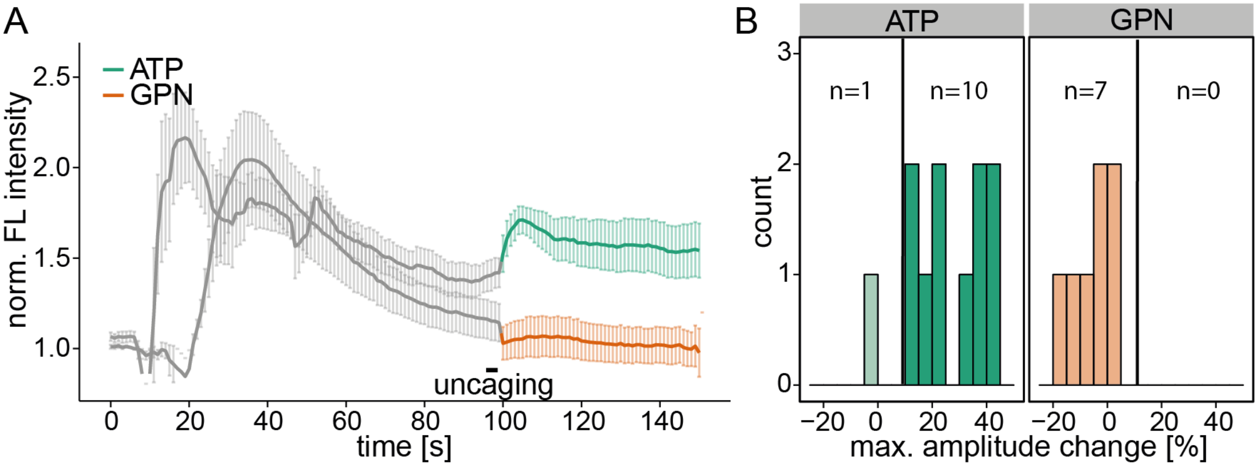

Figure 2.9 Pre-release experiments. A) Mean fluorescence traces of HeLa cells stimulated with 10 µM ATP (11 cells) or 200 mM glycyl-L-phenylalanine-beta-naphthylamide (GPN). Uncaging was performed at t = 100 s as indicated by the horizontal bar. B) Histogram of the maximum amplitudes. The threshold for responding cells was lowered to 10 % amplitude change over baseline.

The increase in cytosolic calcium was monitored and Sph uncaging was performed after the transient had passed (at t = 100 s). As expected, Sph release led to a second calcium transient even after the ER store had been emptied, suggesting that another intracellular calcium store was involved. These findings further supported the hypothesis that indeed Sph, and not S1P was responsible for these calcium transients, since S1P has been shown to release calcium from the ER[138].

Another, important calcium store is comprised of acidic vesicles such as endosomes and lysosomes, which contain up to 600 µM calcium[62]. To investigate their involvement in the Sph-induced calcium response, a separate pre-release experiment was performed. Glycyl-L-phenylalanine-*beta*-naphthylamide (GPN) is hydrolyzed by cathepsin C in lysosomes and causes osmotic lysis of acidic vesicles, consequently releasing their calcium[179]. After adding GPN to HeLa cells, a calcium increase similar to ATP stimulation was observed. However, uncaging Sph after the transient had passed failed to induce a second signal (Figure 2.9, orange trace), thereby strongly supporting the acidic compartment as the principal organelle to release its calcium in response to stimulation with Sph. This result is a novel finding which links sphingolipid metabolism to lysosomal calcium signaling and potentially constitutes a first confirmed function for Sph in cellular signaling.

2.1.5. Sph-induced calcium release from acidic stores requires TPC1

The mechanisms responsible for acidic store calcium release are not yet well defined. Several channels located to endosomes and lysosomes have been identified, most importantly the two-pore channels (TPC1 and TPC2) as well as mucolipin channel 1 (TRPML1). TPCs have recently been shown to be activated by nicotinic acid adenine dinucleotide phosphate (NAADP)[180,181], by Mg^{2+} and phosphatidylinositol 3,5-bisphosphate ($PI(3,5)P_2$)[72]. $PI(3,5)P_2$ has also been implicated in the regulation of TRPML1[182]. In this study, Sph-induced calcium release was investigated in cells devoid of TPCs or TRPML1 to see whether one of these channels was involved in this response as follows. First, we used fibroblasts derived from patients suffering from mucolipidosis type IV (MLIV), a disease characterized by mutations resulting in loss-of-function of TRPML1[75]. Uncaging Sph in these cells did not attenuate the calcium signal, but led to calcium transients with even higher mean amplitudes compared to fibroblasts derived from healthy controls (Figure 2.10a).

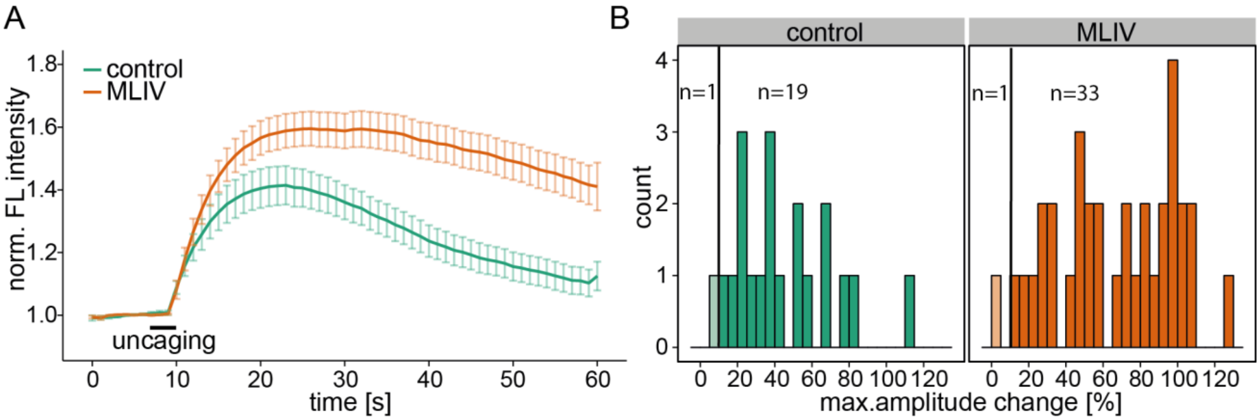

Figure 2.10 Contribution of TRPML1 channel. A) Mean fluorescent traces of control and mucolipidosis type IV (MLIV) patient derived fibroblasts. B) Histogram of the maximum observed amplitudes compared to baseline with the threshold set at 10 % increase over baseline.

MLIV patient derived fibroblasts exhibit a markedly different morphology to previously studied HeLa cells, mainly a bigger size. While the area and duration of uncaging was kept the same in all experiments across cell types, the calcium amplitudes were reduced in patient fibroblasts because the Fluo-4 intensities were averaged over a bigger area. The threshold of response for analyzing single cell responses was therefore reduced to 10 % increase over baseline compared to 20 % increase in HeLa cells (see vertical line in Figure 2.10b). Only one out of 20 control fibroblasts and one out of 34 MLIV patient-derived fibroblasts were non-responsive to Sph-uncaging. We therefore concluded that TRPML1 does not mediate Sph-induced calcium efflux from the acidic stores.

To investigate the contribution of two-pore channels, we employed embryonic fibroblasts derived from mice devoid of either TPC1, TPC2 or both (double knock-out, DKO)[183]. Again, an immediate calcium increase upon Sph uncaging was observed in WT mouse embryonic fibroblasts (Figure 2.10). TPC2 knock-out fibroblasts gave rise to comparable, if only slightly reduced amplitudes and response rates, indicating that TPC2 was probably not involved in the calcium response.

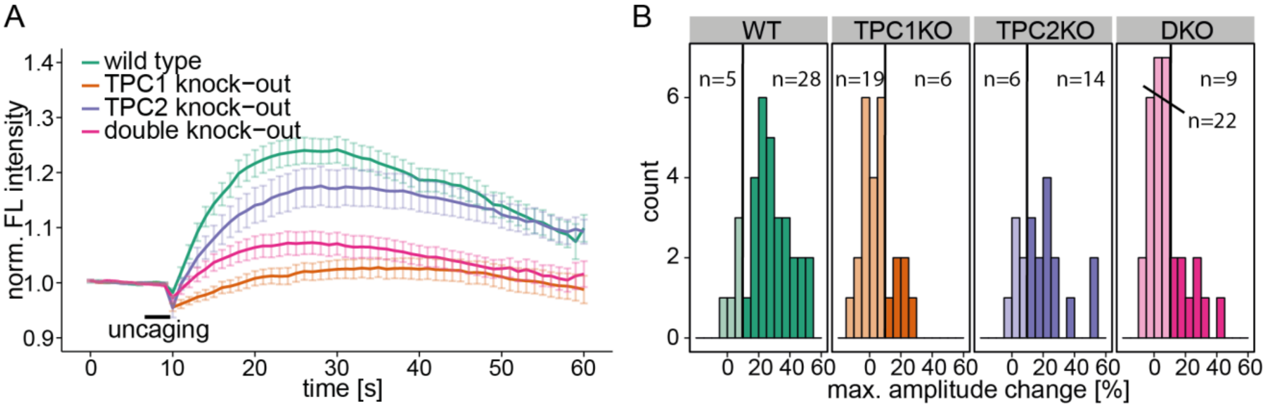

Figure 2.11 Two-pore channel knock-out studies. A) Mean fluorescent traces of primary mouse embryonic fibroblasts. B) Histograms of the maximum amplitudes compared to baseline, with a threshold at 10 % increase over baseline.

TPC1 knock-out fibroblasts, on the other hand, gave a significantly reduced mean calcium response compared to wild type and TPC2 knock-out cells. Only 6 out of 25 TPC1KO cells showed a response upon uncaging, and the maximum amplitudes of these responders were markedly decreased compared to wild type and TPC2KO (Figure 2.11b). We infer that TPC1 is responsible for releasing calcium from the endolysosomes upon increase in Sph concentration. To verify this finding, we employed fibroblasts from a TPC double knock-out mouse and again performed uncaging experiments. DKO fibroblasts also showed a strongly reduced mean calcium response as well as a decreased response rate. We therefore concluded that Sph-induced release of calcium from the acidic stores was mediated by TPC1, which has been shown to localize to early, recycling, and late endosomes as well as lysosomes[180].

Furthermore, these results also show that Sph-induced calcium signaling is not restricted to one cell type (such as HeLa cells), but is a general feature of intracellular signaling and can also be observed in human patient derived cells or in primary mouse embryonic fibroblasts.

Since two-pore channels are critically involved in NAADP-dependent calcium signaling[180,184], we decided to investigate whether NAADP and Sph act on the same targets. However, NAADP is a highly charged and therefore non-membrane permeant compound. For this reason, we used a membrane permeant pharmacological antagonist of NAADP, Ned-19[185], to study its effect on Sph-induced calcium release in HeLa cells (Figure 2.12).

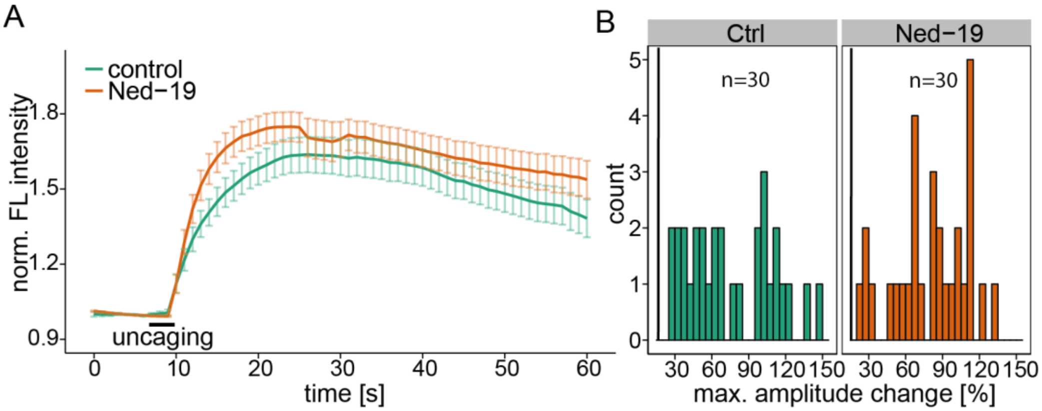

Figure 2.12 NAADP antagonist Ned-19 does not influence Sph induced calcium signals. A) Mean fluorescent traces of Ned-19 (100 µM) treated HeLa cells. B) Histogram of the distribution of maximum observed amplitudes with 20 % threshold.

Ned-19 treated HeLa cells did not exhibit a markedly different calcium response after Sph uncaging, which is in line with previous observations that TPC1 is unresponsive to Ned-19[186]. This result also strengthens the hypothesis that Sph acted specifically on TPC1 and not on TPC2.

2.1.6. Sph-mediated calcium release leads to the nuclear translocation of transcription factor EB (TFEB)

The biological significance of the lysosome as a signaling hub has been well established in recent years[187]. Sabatini's group found that the mTOR-complex, an important kinase which regulates cell growth, is translocated to the lysosome upon amino acid stimulation[77]. Another line of investigation found a new transcription factor, (transcription factor EB, TFEB) to be a master regulator of lysosomal biogenesis[80], which, in absence of nutrients, shuttles to the nucleus and targets several autophagy-mediating genes[79]. The mechanism of this TFEB nuclear translocation was very recently revealed: While lysosome-located mTOR phosphorylates TFEB and thus keeps it in the cytoplasm, cues such as starvation or exercise lead release of mTOR from the lysosomal surface and to calcium release from the lysosomal stores. This activates the phosphatase calcineurin, which binds and dephosphorylates TFEB and thereby promotes TFEB nuclear translocation[82] (see also Figure 1.7). The authors also showed that the lysosomal calcium release is mediated by TRPML1, but they did not investigate the contribution of TPC1. Taken together, our findings also link acidic store calcium signaling to central cellular processes such as autophagy.

In this work, we investigated whether sphingosine-induced lysosomal calcium signaling is also able to induce TFEB nuclear translocation. To do this, we expressed a TFEB-GFP fusion in HeLa cells together with a genetically encoded calcium sensor R-GECO[188]. We performed uncaging experiments while simultaneously monitoring the calcium release and the subcellular localization of TFEB. As can be seen in Figure 2.13, uncaged cells showed an increase in cytosolic calcium as well as visible translocation of TFEB to the nucleus within 5 min after uncaging.

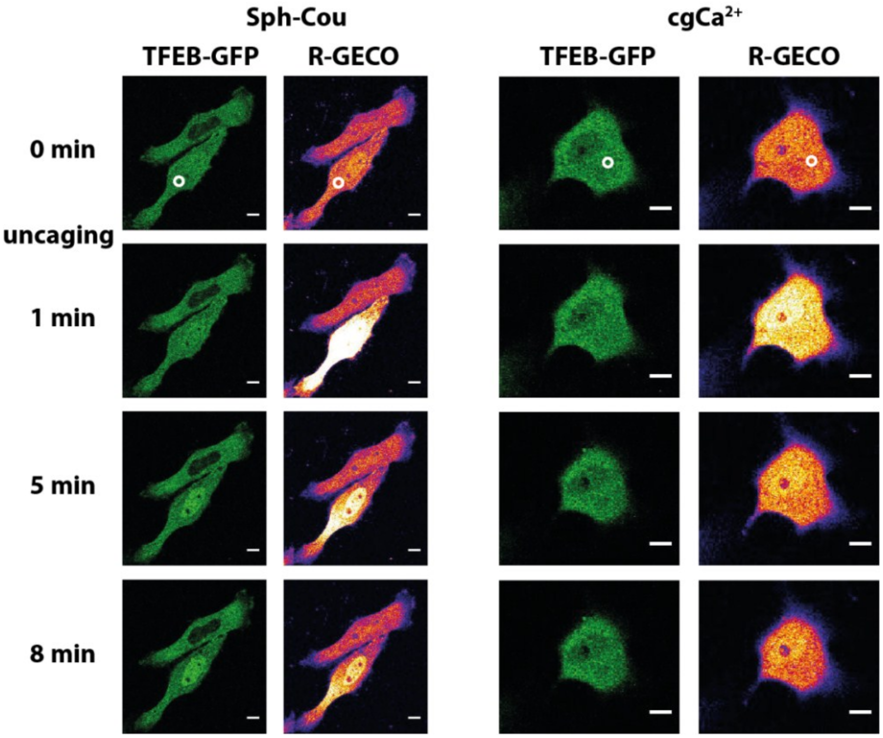

Figure 2.13 Sph uncaging leads to TFEB translocation to the nucleus. Time-lapse confocal microscopy images of HeLa cells transfected with TFEB-GFP and R-GECO. Uncaging was performed in a small area in the cells for 3s (Sph-Cou) or 2 s (cg Ca^{2+}).

As a negative control, we increased the cytoplasmic calcium concentration by uncaging o-nitrophenyl EGTA (“caged calcium”), a commercially available reagent which liberates calcium upon irradiation[189]. Releasing calcium in this way did not lead to TFEB nuclear translocation. Longer uncaging times of caged calcium led to a massive calcium increase in the cells which then induced TFEB translocation. This specific effect suggests that calcineurin senses calcium microdomains near the lysosomes and selectively dephosphorylates TFEB only upon a lysosomal calcium signal. Calcium release mediated ty TRPML1 has been reported to lead to TFEB tranlocation[82]. Our results confirm that lysosomal calcium signals induce nuclear translocation of TFEB and suggest that mediation by TPC1 has the same effect. We hypothesize that TFEB translocation upon Sph stimulation is also able to increase transcription of autophagy-related genes as it was shown previously[79,82,84]. These results further underline the importance of understanding the mechanisms of lysosomal calcium signaling and their ties to other cellular processes.

2.1.7. Calcium release is reduced in Niemann-Pick disease type C

NPC was long thought of as a cholesterol storage disease. Indeed, cholesterol accumulation is still used for clinical diagnosis using filipin staining[46] (Figure 1.5). However, it has become clear that the materials stored in NPC are much more complex than in other lysosomal storage disorders. Apart from cholesterol, sphingomyelin and glycosphingolipids, also sphingosine accumulates[54]. Another distinct hallmark of NPC is a defective acidic store calcium homeostasis which is downstream of Sph accumulation and leads to lower concentrations of calcium in the acidic stores[57]. Elevation of cytosolic calcium levels using agents like curcumin corrected the NPC cellular phenotype and helped to prolong the lifespan of NPC mice[57].

To further investigate this link between Sph and acidic store calcium signaling in NPC, we performed Sph uncaging experiments in fibroblasts derived from healthy subjects (control) and from NPC patients. As expected, the release of acidic store calcium in NPC fibroblasts after Sph uncaging gave rise to lower cytosolic calcium amplitudes compared to control fibroblasts (Figure 2.14). Previous measurements on NPC patient cells show reductions in acidic store calcium concentrations reduced by up to 70 %[57].

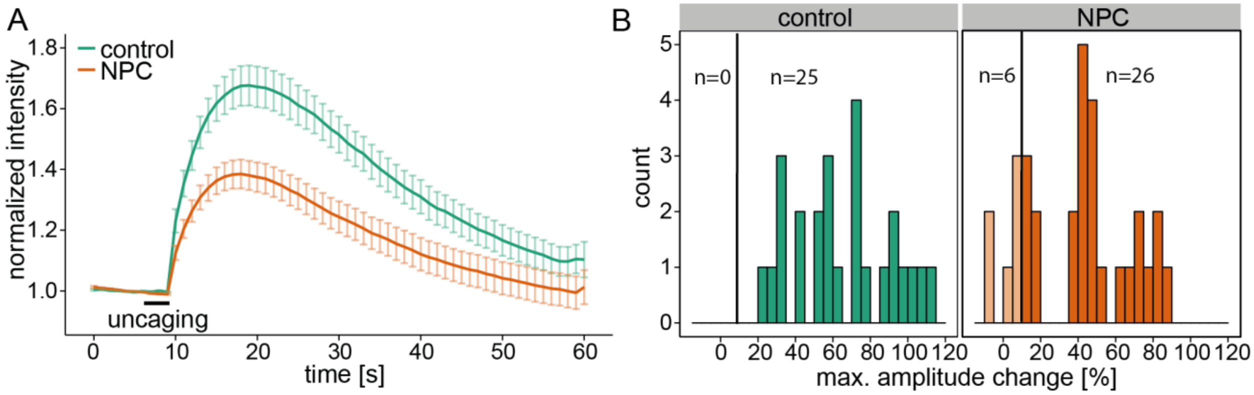

Figure 2.14 Calcium signaling in NPC disease. A) Mean fluorescent traces of control (25 cells) and NPC-patient derived fibroblasts (31 cells). B) Histogram of the distribution of maximum amplitudes with a response threshold set at 10% .

These results from NPC patient fibroblasts are the first direct evidence of Sph action upstream of acidic calcium signaling in this disease. They further confirm our previous results showing that Sph releases calcium directly from acidic stores and not from other intracellular compartments.

2.1.8. Sph localizes to late endosomes / lysosomes and accumulates in NPC

Of all lipid materials stored in NPC, only cholesterol can be probed for its subcellular localization by use of the Filipin complex. The latter revealed cholesterol to accumulate in late endosomes / lysosomes of NPC patient cells (see Figure 1.5) and consequently colocalize with the LAMP-1 antibody, as was shown previously[190]. The localization of sphingosine and higher sphingolipids is more difficult to study owing to a lack of tools. Even though fluorescent sphingolipids, e.g. sphingolipids modified with a small fluorescent group (usually nitrobenzoxadiazole, NBD or boron-dipyrromethene, BODIPY) are commercially available, these lipids do not faithfully represent the localization of endogenous sphingolipids since the NBD and BODIPY groups drastically alter their physical properties[115]. Bifunctional lipids are minimally modified and more closely mimic endogenous lipids, a fact which is useful in probing the subcellular localization of these lipids as shown using a bifunctional fatty acid precursor[151]. Per Haberkant synthesized a photoactivatable and clickable sphingosine (pacSph) and provided me with this compound to perform localization studies of Sph in NPC fibroblasts.

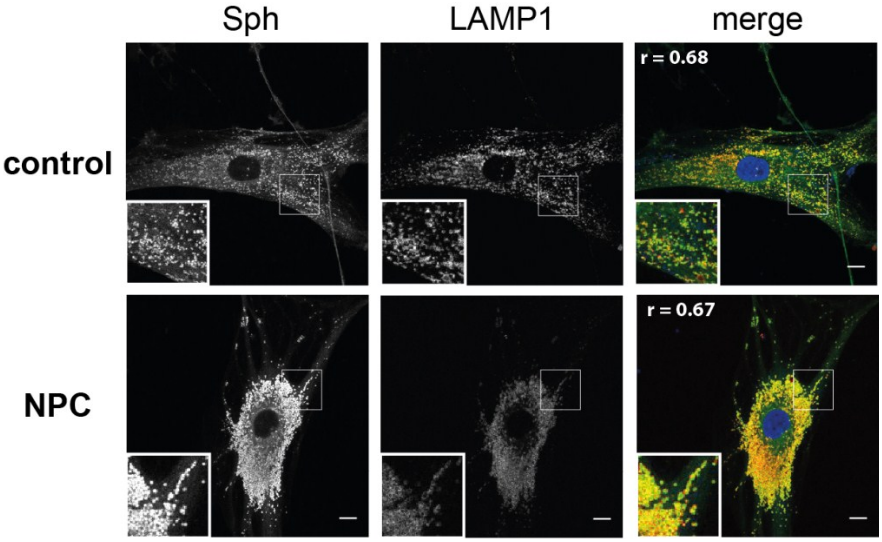

Figure 2.15 Subcellular localization of Sph. Confocal images of N_3-Alexa488-labelled TFS (green) and LAMP1 antibody (red) in human fibroblasts. The Pearson's correlation coefficient r is shown in the top left corner of the merged image. Scale bar represents 10 µm.

To investigate the subcellular location of Sph, we incubated control and NPC fibroblasts with pacSph for a short time (10 min) to minimize conversion to higher sphingolipids. The lipids were photo-crosslinked before fixation and subsequently visualized via click-reaction with a fluorophore (Alexa488-azide). Figure 2.15 shows a clear localization of pacSph to LAMP1-positive vesicles in both control and NPC fibroblasts.

This is the first direct evidence of Sph localization at the acidic compartment, which was postulated for a long time since the other stored materials such as cholesterol and glycosphingolipids also accumulate in these vesicles[191,192]. A striking difference between control and NPC fibroblasts was the number and size of late endosomes / lysosomes and the concentration of Sph therein, all of which were markedly increased in the NPC cells. It is known that the acidic compartment, which is usually visualized by LysoTracker staining, is enlarged in NPC disease[57,193]. Our findings confirm that Sph is indeed present at higher concentrations in these vesicles compared to control cells, as revealed by the increased Alexa488-staining.

A common hypothesis in the NPC field is that these lipids accumulate in the acidic compartments due to a post-endolysosomal trafficking block[55]. To check whether this block can be visualized using pacSph, we performed pulse-chase experiments. We labelled control and NPC fibroblasts with pacSph for 10 min as in the previous experiment (i.e. pulse), but instead of immediate crosslinking, cells were washed and incubated for further 10 min without pacSph (i.e. chase) before crosslinking and fixation. In this way, we followed the change of subcellular localization of Sph as it went through its metabolic path.

Figure 2.16 shows that Sph in control fibroblasts no longer co-localized with the LAMP1 antibody, but stained internal membranes, indicating release from the acidic compartments. Sph was likely transported to ceramide synthases at the ER[33] as part of the sphingolipid metabolic pathway[34]. On the other hand, Sph in NPC fibroblasts still co-localized with LAMP1 after 10 min chase and showed similar fluorescence intensities as at 0 min chase time. This points towards a Sph trafficking blockage at the late-endosomal / lysosomal stage and explains the increased Sph staining in NPC fibroblasts.

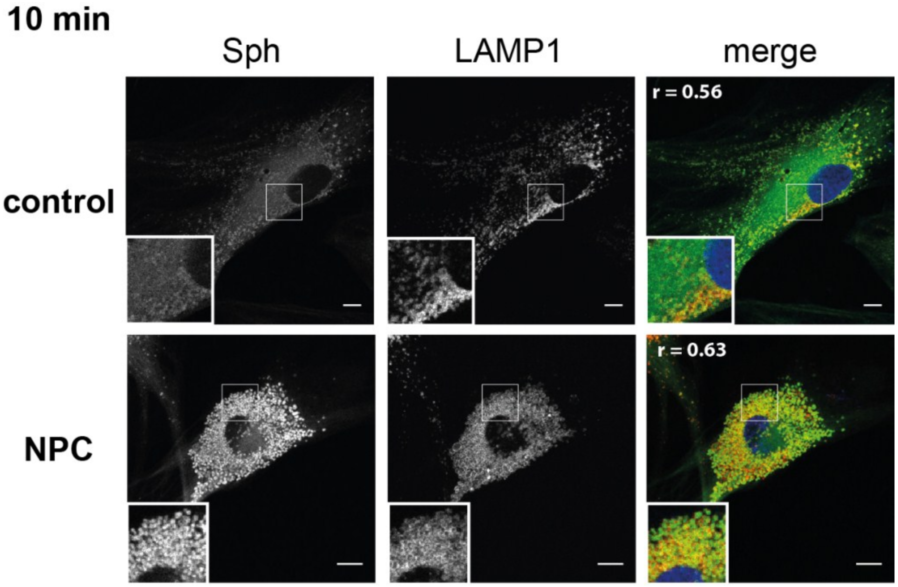

Figure 2.16 Subcellular localization of Sph after 10 min chase. Confocal images of N_3-Alexa488-labelled TFS (green) and LAMP1 antibody (red) in human fibroblast after 10 min chase. The Pearson's correlation coefficient r is shown in the top left corner of the merged image. Scale bar represents 10 µm.

2.1.9. Conclusion and outlook

Sph is a known bioactive lipid, yet few of its actions have been characterized on a molecular level. One of the few identified targets of Sph apart from its metabolizing enzymes is protein kinase C (PKC), which it inhibits[174]. Several apoptotic effects of Sph have been attributed to this inhibition[23]. Sph is also involved in the pathophysiology of NPC disease. Its accumulation has been shown upstream of a reduction in lysosomal calcium concentration[57]. In this work, we investigated the actions of intracellular Sph on lysosomal calcium signaling. Caged Sph proved to be a valuable tool to investigate this process which could not have been studied with conventional means (exogenous lipid addition, RNAi-mediated knock-down, or small molecule modulators). We found that spontaneously generated intracellular Sph is capable of releasing calcium from acidic stores, while addition of Sph to the medium of the cells did not evoke such a calcium release. This effect was specific to Sph since even dhSph, a naturally occurring, close structural analogue, did not release calcium upon intracellular photo-release. We further excluded any contribution of the immediate Sph-metabolite S1P, which is known to increase cytosolic calcium either via extracellular action on S1P G-protein coupled receptors[169] or by intracellular release from the ER through a yet unidentified receptor[138,194].

Caged Sph was applied to three different cell lines: cultured HeLa cells, primary mouse embryonic fibroblasts and human patient-derived cells. Uncaging Sph stimulated a calcium transient in all cell types, indicating that this newly discovered connection between Sph and lysosomal calcium release is an important and general feature of intracellular signaling.

We further pinpointed the endosomal/lysosomal channel TPC1 to be necessary for this response by employing embryonic fibroblasts from Tpc1$^{-/-}$ mice. The roles of two-pore channels have been widely debated in recent years. While many reports agree that TPC channels are NAADP-regulated Ca^{2+} channels[65,66,180,181], others indicate a broader ion specificity of TPCs[64,68,195] or alternative ligands such as $PI(3,5)P_2$[68,69]. Another report hinted towards a convergent regulation of TPC2 by Mg^{2+}, NAADP, $PI(3,5)P_2$ and two protein kinases (JNK and p38)[72]. Some of these findings were recently reconciled in a study showing that TPCs conduct both Ca^{2+} and Na^+ ions and that TPCs are activated by NAADP as well as $PI(3,5)P_2$[73,196]. This work introduces Sph as a new small molecule activator of TPC.

Several questions still remain concerning the mechanism of TPC1 activation. First, it is unclear if Sph has a direct interaction with TPC1 or if other, yet unidentified molecules mediate this response. Similarly, the site of Sph action needs to be addressed. Does the initiation of Sph-induced calcium release take place outside the lysosome, from the lysosomal lumen or within the lysosomal membrane? Second, the crosstalk of Sph-induced TPC1 activation with NAADP-induced TPC1 activation remains unclear. Since TPC1 is unresponsive to the small molecule NAADP-antagonist Ned-19[186], other tools such as a membrane-permeant version of NAADP[197] should be employed to investigate how NAADP influences Sph action on TPC1.

Sph-induced calcium signaling was also investigated in the context of NPC disease. The calcium release from the lysosomes in NPC patient fibroblasts was reduced compared to control fibroblasts. This is in line with other measurements performed with an intra-lysosomal calcium probe, showing that lysosomal calcium content is reduced in NPC due to an acidic store-filling defect[57]. Furthermore, we visualized the subcellular localization of Sph in NPC fibroblasts for the first time. Using the bifunctional Sph probe synthesized by Per Haberkant, we localized Sph to late endosomes and lysosomes, which were more numerous and larger in NPC fibroblasts compared to control. The concentration of Sph inside these vesicles was also higher in NPC cells. This is in line with observations made for cholesterol using the Filipin staining (Figure 1.5) and indicates that both these lipids are stored in the same compartments. To investigate whether post-lysosomal traffic is impaired in NPC disease as suggested in literature[55], we performed pulse-chase experiments and showed that Sph exited the endosomes/lysosomes in healthy controls, while it accumulated in NPC cells. It is hypothesized that permanently lowered acidic store calcium levels in NPC cells are responsible for the secondary accumulation of cholesterol, glycosphingolipids and sphingomyelin due to defective, calcium-dependent vesicle fusion[57]. Sph accumulation, however, occurs upstream of the calcium defect[57]. Our work gives the first evidence of a direct connection between Sph and lysosomal calcium efflux. Identification of the exact mechanism of Sph action on lysosomal calcium homeostasis could uncover new potential therapeutic targets for treatment of NPC. Another challenge is to identify the function of the NPC1 protein itself and how its inactivation leads to Sph accumulation. This would offer another point of therapeutic intervention.

Few biological processes, such as vesicle fusion and secretion[198] as well as induction of autophagy and lysosomal biogenesis[82] have been shown to depend on lysosomal calcium efflux. The mechanism of autophagy induction was recently identified and involved the nuclear translocation of TFEB upon dephosphorylation by calcineurin, which in turn was activated by TRPML1-mediated lysosomal calcium efflux[82]. We also confirmed TFEB nuclear translocation upon lysosomal calcium efflux, in our case through TPC1 and stimulated by intracellular Sph. Since nuclear TFEB initiates transcription of autophagic genes, it is interesting to speculate that Sph-rich and potentially “leaky” lysosomes might lead to a permanent calcium signal and an over-induction of autophagy in the NPC disease. Indeed, increased autophagic flux and marked accumulation of autophagosomes are hallmarks of the NPC disease[199]. In NPC1-deficient cells, the inhibition of autophagy was found to have ameliorative effects[200], which may be attributed to lowered lysosomal stress due to a reduced delivery of autophagic substrates. Caged Sph could be used in the future as a tool to investigate whether releasing Sph within cells, especially neurons, which are particularly vulnerable in NPC disease, is capable of inducing an NPC-like phenotype by stimulating lysosomal calcium efflux.

2.2. Trifunctional sphingosine is a novel tool to identify protein-Sph interactions

Sphingolipids have been shown to influence central cellular processes[106,201] and their deregulation is implicated in severe diseases such as cancer[27,202], diabetes and metabolic disorders[203,204]. However, the mechanism of action of these lipids is poorly understood, mostly due to a lack of tools to investigate their interaction with proteins in a systematic fashion. Several excellent techniques for *in vitro* studies of protein-lipid interactions have been developed recently[131,205] but these rely on recombinant expression or cell lysates and are therefore limited to soluble proteins. To also investigate interactions of lipids with integral membrane proteins, and to examine these interactions in living cells, a bifunctional lipid technology was established[206]. Briefly, a lipid precursor is chemically modified with two additional functionalities:

1) a photoactivatable diazirine group which, upon irradiation, creates a covalent bond between the lipid and the interacting protein and
2) an alkyne group as a click handle for subsequent tagging and proteomic identification of the lipid-protein complexes.

One drawback of this method is that upon addition to the cells, the bifunctional precursor is immediately subjected to lipid metabolism and so several lipid species are generated of which all carry the additional functionalities. The identified proteins may therefore interact with multiple members of the investigated lipid class. To pinpoint proteins interacting with a single lipid species, we added to the bifunctional lipid technology by developing a caged bifunctional Sph (i.e. “trifunctional” Sph). This compound was designed so that uncaging of the lipid inside cells followed by immediate photocrosslinking should prevent lipid metabolism before crosslinking. This technology should enable the identification of the protein interactome of a single, well defined lipid species.

2.2.1. Design and synthesis of trifunctional sphingosine

For the synthesis of trifunctional sphingosine (TFS), we again chose to employ the DEAC group since its photochemical properties are compatible with the diazirine group. This strategy allows the uncaging reaction, which needs to precede the crosslinking at higher wavelengths (~ 400 nm) whereas the diazirine group is activated at 350 nm. The synthesis of trifunctional Sph was performed in a similar fashion to the synthesis of Sph-Cou (Chapter 2.1.1., see Figure 2.17a), using the bifunctional Sph provided by Per Haberkant. André Nadler in our group synthesized a trifunctional diacylglycerol species (stearoyl-arachidonylglycerol, SAG) as well as a trifunctional fatty acid (stearic acid) which served as control compounds during the interaction studies (Figure 2.16 b) and c)).

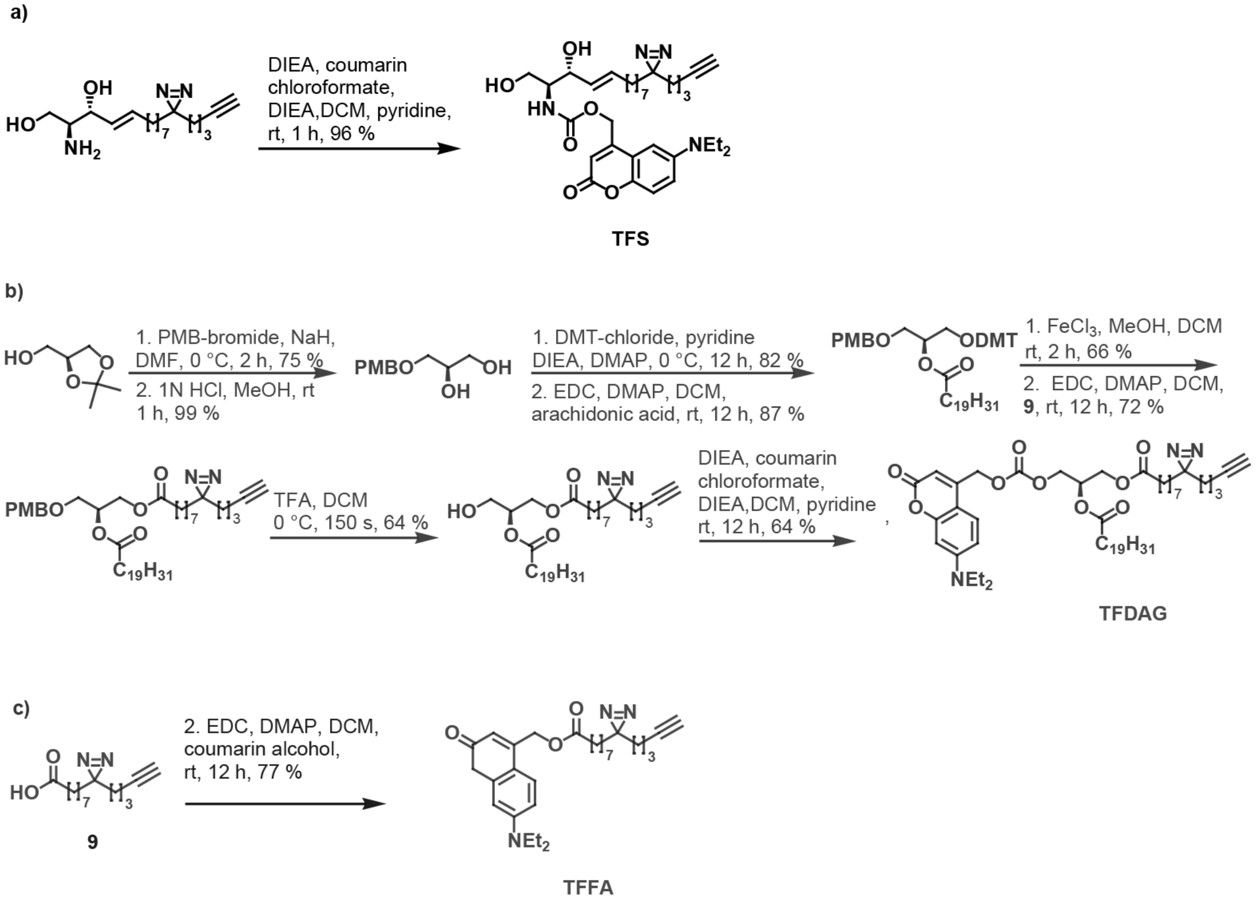

Figure 2.17 Synthesis of trifunctional lipids. a) Synthesis of trifunctional sphingosine (TFS). b) Synthesis of trifunctional diacylglycerol (TFDAG). c) Synthesis of trifunctional fatty acid (TFFA). b) and c) were carried out by André Nadler.

2.2.2. NMR feasibility studies

In order to determine whether the two photoreactions required for the successful application of trifunctional lipids (uncaging and photocrosslinking) are indeed orthogonal, we performed nuclear magnetic resonance (NMR) studies on the pure compounds. We chose to use TFDAG, which has a well dispersed ^{1}H-NMR spectrum where the relevant peaks were not overlapping with others and could therefore be easily monitored. Figure 2.18 shows a part of the spectrum of TFDAG with the relevant proton signals assigned in different colors. After collecting this spectrum, the NMR tube was subjected to a 2 min irradiation step using a mercury arc source (Newport) equipped with a 400 nm highpass filter. After this first irradiation step, i.e. the uncaging reaction, signals stemming from the CH_2-groups next to the carbamate linker (red and blue peaks) changed their chemical shifts to match the corresponding signals of the bifunctional DAG (BFDAG) standard. This demonstrated a successful and complete uncaging reaction. More importantly, the green and purple resonances (from CH_2 groups next to the diazirine group) did not change their chemical shifts, indicating that the diazirine was intact and that no photocrosslinking took place under the conditions used for uncaging.

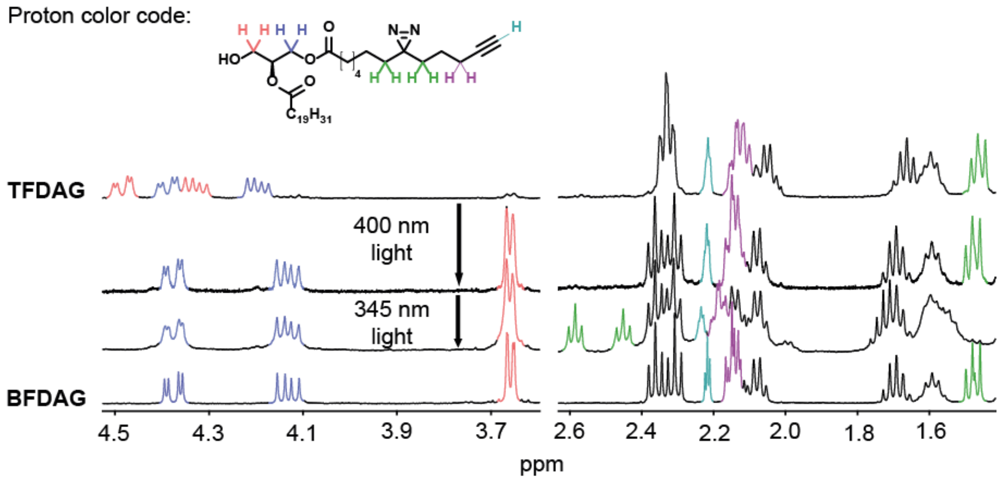

Figure 2.18 Two subsequent photoreactions are orthogonal. NMR spectra of TFDAG in $CDCl_3$ before and after irradiation steps as indicated. This experiment was carried out by André Nadler.

The NMR tube was then subjected to a second 2 min irradiation using the mercury arc source, this time equipped with a 345 nm highpass filter. During this second irradiation step, however, the green and purple resonances shifted considerably, proving that illumination with 345 nm light is necessary for reaction of the diazirine. Notably, the alkyne bond, as monitored through the triplet at 2.22 ppm, remained unaffected by each illumination step.

This experiment demonstrated that it is possible to perform two subsequent photoreactions on the same molecule and that the uncaging reaction can be carried out without affecting the crosslinkable group. This allowed us to precisely control the time of release and crosslinking of the lipid inside the cells. Additionally, it enabled us to perform very accurate pulse-chase experiments in order to follow the lipid metabolism in time and space either on TLC or with fluorescent microscopy.

2.2.3. Trifunctional lipids are inert and stable in the cellular environment

As with the caged Sph (chapter 2.1.), the success of this approach is dependent on the stability and the biological inactivity of the trifunctional lipids. We therefore tested whether the cage group was cleaved or whether the lipid precursors were metabolized before uncaging. Cells were incubated with trifunctional lipids for different times and the extracted cellular lipids were labelling by click-reaction with a fluorogenic compound. The most commonly used molecule for labeling lipid extracts is the commercially available 3-azido-7-hydroxycoumarin, which has already been used in several studies[151,159].

Unfortunately, the excitation and emission spectra of this compound are very similar to the DEAC group used in the synthesis of the trifunctional lipids. This complicates detection during TLC analysis and required the use of a new, orthogonal fluorophore. A longer-wavelength, fluorogenic fluorescein was reported recently[207] and prepared by André Nadler in our group. *p*-Azidofluorescein has a reported absorption maximum around 495 nm and an emission maximum around 518 nm[207], whereas the DEAC group absorbs around 375 nm. Azidofluorescein labelled lipids were detected independently of whether or not they bear a DEAC group. Unfortunately, the fluorogenity of azidofluorescein is lower than that of the commercially available coumarin, so that unreacted azidofluorescein is still visible on the TLC (see Figure 2.19). As a control, click reactions were performed in absence of alkyne-containing lipids and the resulting bands migrating with $R_f = 0.36$ and $R_f = 0.45$ were therefore attributed as background bands stemming from unreacted azidofluorescein.

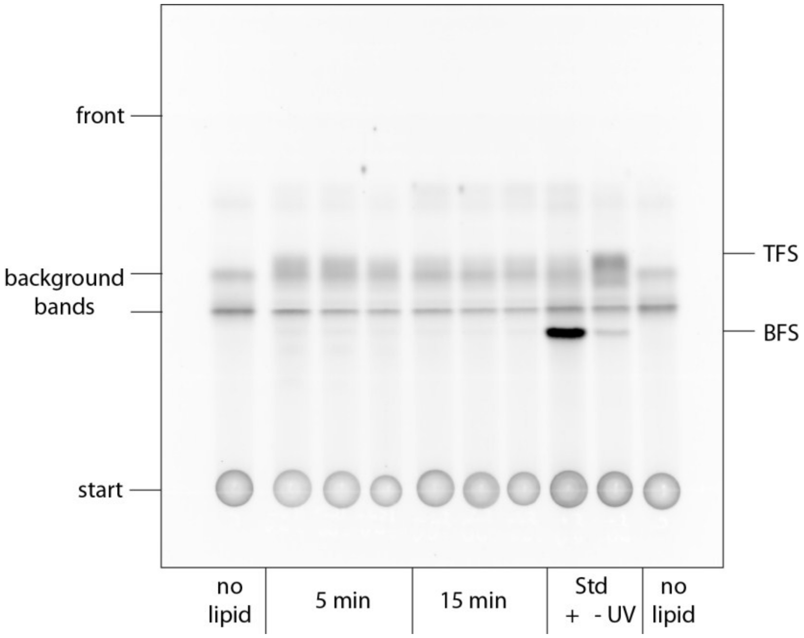

Figure 2.19 TFS is stable in the cellular environment. TLC analysis of lipid extracts of HeLa cells clicked to azidofluorescein. Pure TFS was subjected to +/- UV treatment, reacted with azidofluorescein and spotted as reference compounds (Std).

Figure 2.19 shows the TLC analysis of lipid extracts of HeLa cells incubated with TFS for the indicated time. The lipids were visualized by click-reaction with azidofluorescein. In both 5 min and 15 min incubation conditions, only one band, which co-migrated with the TFS standard, was visible. Apart from the background bands, there are no additional azidofluorescein-labelled spots, indicating that the TFS is inert and that it is not metabolized to other lipids in its caged state within these timeframes. The same experiment for the other trifunctional lipids was performed by André Nadler and proved inertness also for TFDAG and TFFA.

Having established the metabolic stability of all trifunctional lipids, we next determined loading conditions which would result in similar amounts of lipids inside the cells. HeLa cells were loaded with different concentrations of trifunctional lipids and their DEAC-fluorescence was monitored over time. Figure 2.20 displays the subcellular localization of the three trifunctional lipids in conditions which resulted in similar fluorescence intensities. It was notable that TFS was readily taken up by the cells, so that even a short incubation time of 5 min and a low concentration of 6 µM gave rise to fluorescence comparable of 100 µM TFDAG incubated for 15 min.

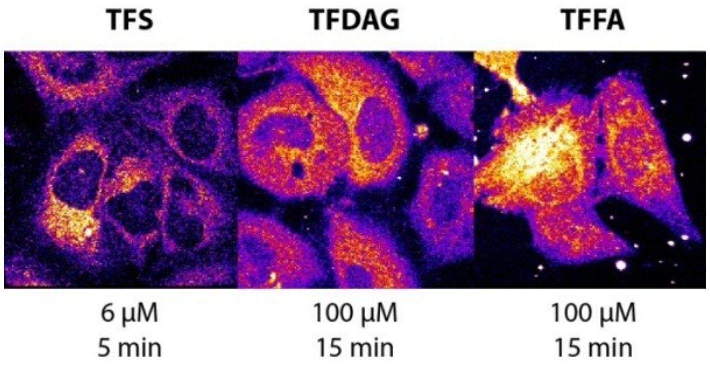

Figure 2.20 Subcellular distribution of trifunctional lipids. Confocal images of HeLa cells incubated with the indicated concentrations of trifunctional lipids.

As can be seen in Figure 2.20, the subcellular localization of all three lipids was determined by the properties of the DEAC cage and resulted in unspecific intracellular membrane staining and did not reflect the endogenous localization of the respective lipids. This unspecific uptake and labelling of cells by coumarin derivatives has already been reported[208]. With respect to the design of the proteomic screen, we decided to use the negative control TFFA at a concentration equal to that of TFDAG even though this gave slightly brighter staining of the cells. We reasoned that this would increase the specificity of the hits identified with TFS or TFDAG if even higher concentrations of TFFA failed to capture them.

2.2.4. Trifunctional lipids are bioactive

To investigate whether the lipids released after photouncaging are indeed biologically active (despite their diazirine and alkyne modifications), we performed pulse-chase experiments and monitored the resulting lipids by TLC. If the lipids were recognized by the cellular machinery, they would be quickly converted to other glycerolipids or sphingolipids. HeLa cells were labelled for 15 min, the lipids were liberated by illumination with 400 nm light and the cells were incubated for a further 15 min. The cellular lipids were then extracted and visualized through their azidofluorescein-adduct (Figure 2.21). The reference compounds were again treated with -/+ UV and taken through the same extraction procedure as the cellular extracts serving as standards. It is notable that the cage group of each pure, trifunctional lipid standards was partly cleaved during the extraction and click-reaction procedure as evident by the additional band in the –UV condition which co-migrated with the bright band of the +UV standard in each case. We quantified the extent of this cleavage as 22 % for TFS and 33 % for TFDAG and TFFA. In this experiment, however, this artefact was of no consequence since we were interested in the cellular lipid extracts after illumination and the standards were only used for co-migration analysis. Another complication was the fact that intact TFFA exhibited the same migration behavior as uncaged TFDAG (bifunctional DAG, BFDAG). Again, this did not hinder the interpretation of this particular experiment, as there was no more TFDAG in the cellular lipid extracts after illumination.

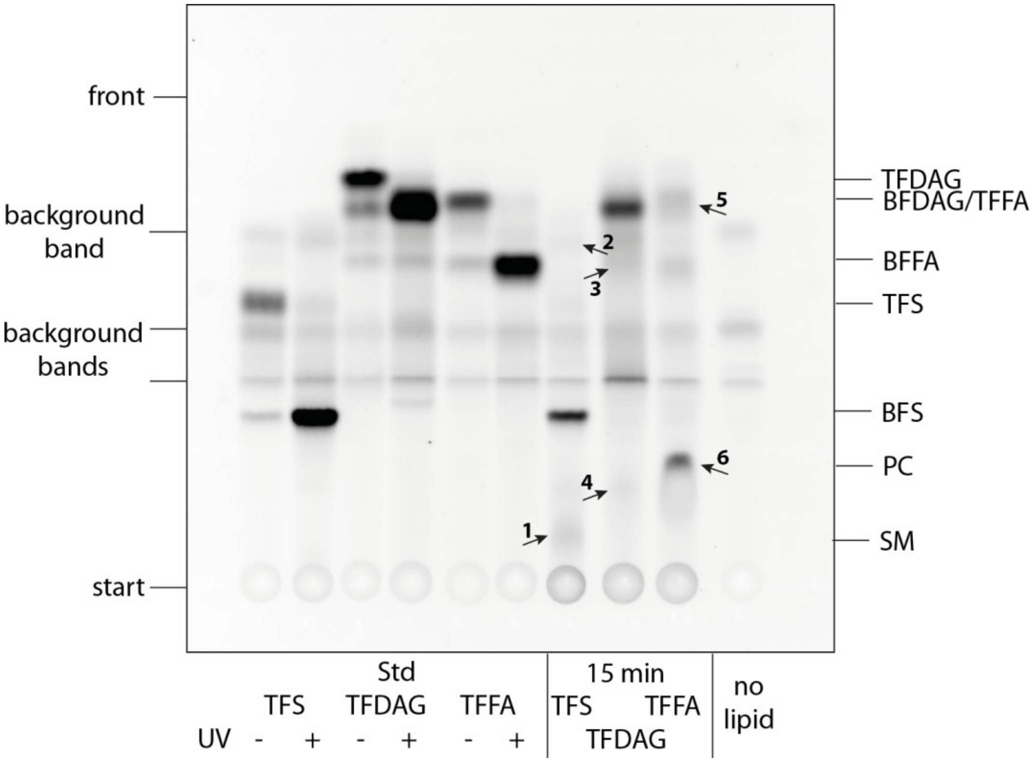

Figure 2.21 Uncaged lipids take part in the cellular metabolism. TLC analysis of lipid extracts of HeLa cells clicked to azidofluorescein after 15 min chase. Standards of each lipid were subjected to -/+ UV treatment, reacted with azidofluorescein and spotted on the left-hand side as reference compounds.

The lipids extracted after 15 min chase time showed additional bands for each trifunctional lipid pulse, indicating that the uncaged lipids were recognized by the lipid handling machinery and metabolized accordingly. The major lipid species in the TFS condition was the liberated (bifunctional) Sph (BFS), but we observed additional bands with slower migration behavior (arrow 1) that may indicate conversion to sphingomyelin. A very faint band migrating slightly faster than BFFA (marked by arrow 2) corresponded with the migration behavior of ceramide (Cer) in experiments done with 3-azido-7-hydroxycoumarin[209]. In such a short chase time, uncaged TFS already gave rise to multiple additional lipid species, indicating that the released bifunctional Sph is a close mimic of endogenous Sph. This is in line with Per Haberkant's studies. Similar observations were also made for TFDAG and TFFA, both of which gave rise to additional lipids (as indicated by arrows 3-6). DAG was converted to a fatty acid and a slow migrating species which we speculate to represent phosphatidylethanolamine (PE, arrow 4). However, we have no standards for PE and cannot prove this speculation. Cells pulsed with TFFA showed the highest level of metabolism and converted TFFA to DAG and mainly, phosphatidylcholine (PC, arrow 6). PC was identified by comparing its migration behavior to standards clicked to the commercial 3-azido-7-hydroxycoumarin in previous studies[151,159].

Another way to determine whether TFS mimics the behavior of endogenous Sph is to perform uncaging experiments and to monitor intracellular calcium signaling as described in chapter 2.1.3. As expected, TFS elicited an increase in cytosolic calcium immediately after uncaging in the same manner as Sph-Cou (Figure 2.22).

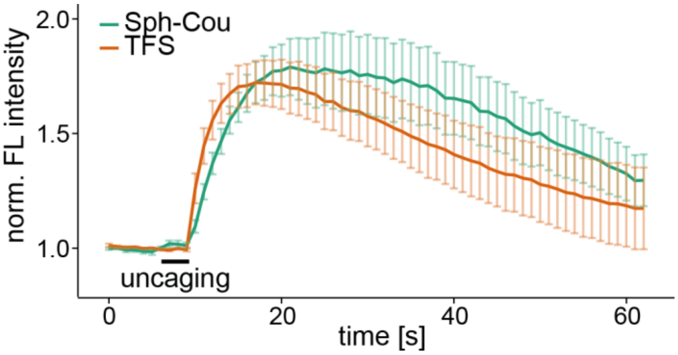

Figure 2.22 Trifunctional Sph uncaging increases cytosolic calcium. Mean Fluo-4 fluorescence traces of HeLa cells incubated with Sph-Cou or TFS. Uncaging was performed in a small circular area within the cell for 3 s as indicated by the black bar. The standard error of the mean is plotted as error bars.

The bioactivity of TFDAG was tested by André Nadler. He performed uncaging experiments and showed translocation of a DAG binding C1-domain (of PKCα) to the plasma membrane upon uncaging of TFDAG (data not shown). Taken together, the TLC and live-cell microscopy experiments showed clearly that the modification of the Sph backbone with two additional functionalities did not hinder its metabolism and that uncaging of TFS (and TFDAG) led to immediate signaling outcomes (calcium increase vs. C1-domain translocation). We therefore concluded that it was feasible to perform useful proteomic screens by uncaging trifunctional lipids in living cells followed by immediate crosslinking to their interacting proteins.

2.2.5. Design and outcome of proteomic screens

The bifunctional lipid technology has already been successfully used for performing several proteomic screens[150–152]. For our study, we adapted the previous protocol to include extra illumination steps and to update the proteolytic digestion. Figure 2.22 shows the workflow of the screens as we performed them. Briefly, we incubated HeLa cells with TFS, TFDAG or TFFA at concentrations determined in chapter 2.2.3. After washing away excess lipid, we irradiated the dishes on ice for 2.5 min at 400 nm and immediately afterwards for another 2.5 min at 345 nm. This immediate change was achieved by switching the two highpass filters in front of the UV lamp with a lever. The cells were scraped, washed and lysed. The proteins were then subjected to a reduction/alkylation step using DTT/iodoacetamide to reduce cysteines and to ensure successful protease digestion. The protein concentration in each condition was determined using the Amido Black assay (see chapter 3.6.2.) and an equal amount of each condition was subjected to a click reaction with biotin-azide.

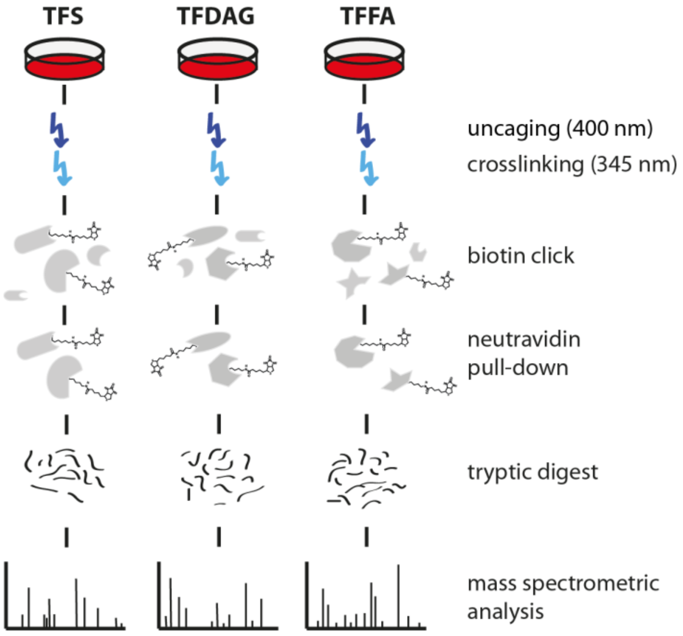

Figure 2.23 Schematic overview of the proteomic screens performed with trifunctional lipids.

Biotinylated protein-lipid complexes were enriched using neutravidin-agarose beads. After the elution step, a tryptic digest was performed on paramagnetic beads as recently described in Hughes et al.[210] and the resulting peptides were separated using high-pH offline fractionation, which increased proteome coverage by separating the peptide mixture in an orthogonal fashion to the LC-MS. 30 fractions were collected and pooled to 10 fractions, which were subjected to a desalting step and subsequently injected into an UPLC-MS/MS system.

The screen was performed twice and yielded a total of 3263 proteins. The overlap between the two screens is depicted as a Venn diagram at the top of Figure 2.24 and shows a good overlap of 1902 proteins identified in both screens. In order to investigate the specificity of the trifunctional lipid approach, we visualized the distribution of proteins identified with each of the different trifunctional lipids (Figure 2.24, bottom row). The majority of proteins in each screen were identified in all three conditions (red numbers) indicating that these proteins were either crosslinked non-specifically to all lipids due to close interaction in the membrane or that they were identified as background of the method due to non-specific binding to the neutravidin beads during pull-down. Conversely, proteins uniquely identified with one lipid may have been interacting with or binding to that lipid at the time of crosslinking. This high background is in line with previous observations[209] and highlights the importance of using adequate control lipids in every screen.

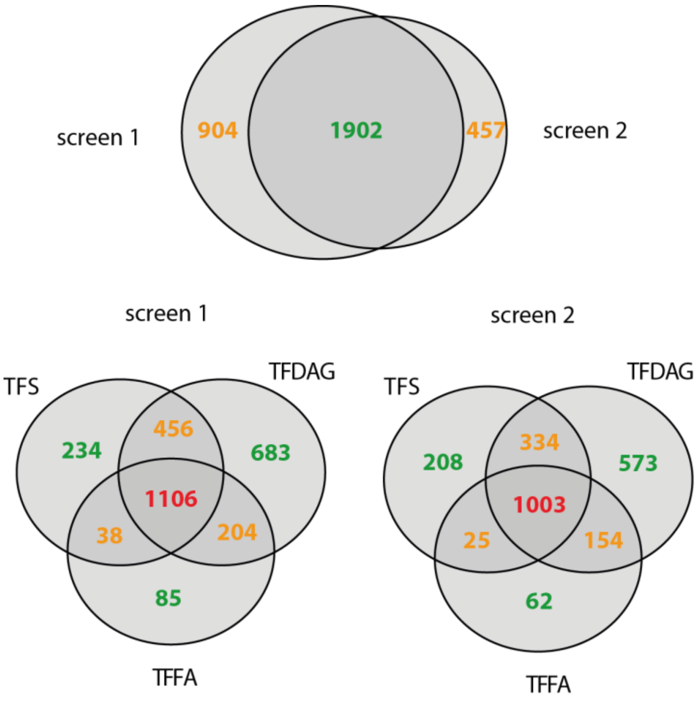

Figure 2.24 Number of proteins identified in two independent proteomic screens.

We narrowed the pool of candidate proteins by only looking at proteins identified in both screens. We visualized their distribution in a heatmap color-coded for their respective peptide spectral matches (PSM), a value indicating how often peptides belonging to the same protein were identified (Figure 2.25)

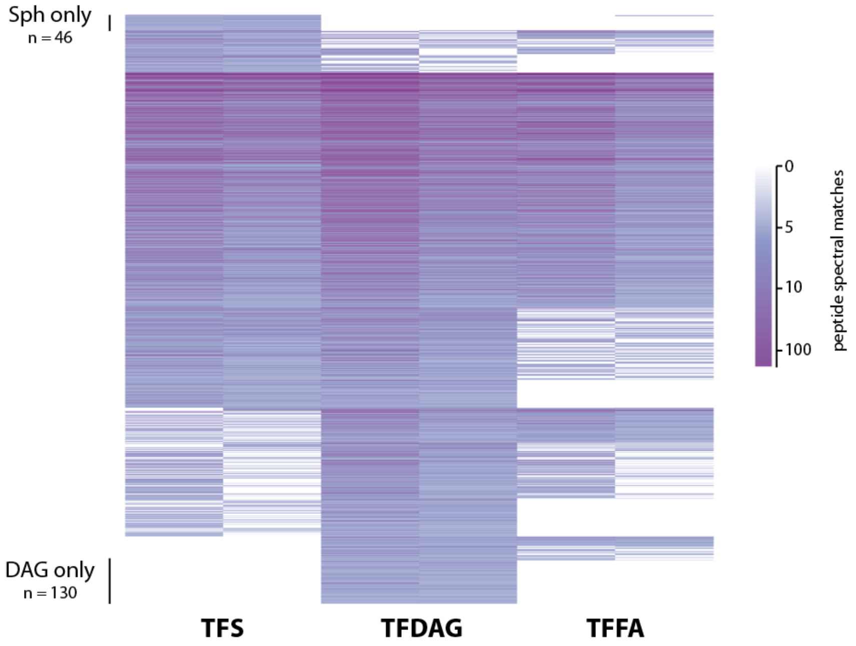

Figure 2.25 Distribution of high-confidence proteins.

It is apparent that the majority of identified proteins were found in all three conditions, indicative of a high background of unselective binding and crosslinking. However, 46 proteins were identified twice only with TFS, whereas 130 proteins were found in TFDAG experiments in both screens. These uniquely identified, 'high confidence' proteins were considered putative Sph or putative DAG binding proteins, respectively. It was still possible that some specific Sph or DAG-binding proteins were additionally identified in the control conditions with low PSM counts due false positive discovery rates in the protein identification procedure. We therefore introduced a threshold of 2.5-fold increased PSM count in one condition over the other two in order to include these proteins as well. This new threshold increased the number of putative Sph-binding proteins to 73 proteins and the number of putative DAG-binding proteins to 228 proteins (see Appendix B). It was encouraging that among the putative Sph-binding proteins, we found enzymes involved in the sphingolipid pathway such as 3-ketodihydrosphingosine reductase and ceramide synthase 2, which is known to bind Sph as a substrate.

We next compared the list of putative Sph-binding proteins obtained with the TFS probe to previous screens using bifunctional Sph (=pacSph) performed by Per Haberkant[209] (Figure 2.26, left-hand side). A quarter of high confidence TFS-binding proteins were uniquely identified with pacSph, further confirming the specificity of these protein-Sph interactions. Another quarter was identified with pacSph but also identified using pacFA as a control lipid, which was incorporated into multiple glycerolipids. It is possible that some of these proteins have dual specificity for Sph and certain glycerolipids (not SAG or arachidonic acid, which we excluded using the TFDAG and TFFA probes), but it is more likely that these proteins were unspecifically crosslinked to an abundant membrane glycerolipid such as PC while also specifically interacting with Sph. The majority of high-confidence TFS-binding proteins were not identified at all in any pacSph-screen. This exemplifies the major advantage of the trifunctional lipid concept: Since the bait lipid was not metabolized and only proteins interacting with Sph were crosslinked, the complexity of the proteome is reduced and proteomic analysis could therefore also detect proteins which were crosslinked at lower frequency and which would otherwise have failed detection due to more abundant proteins crosslinked to higher sphingolipids. A small percentage (10 %) of TFS-binding proteins were not identified with pacSph, but were crosslinked to pacFA. These proteins were either potential false positives in the TFS screen or they represent proteins which were crosslinked to Sph at low frequency and failed detection with pacSph, but were unspecifically crosslinked to glycerolipids such as PC.

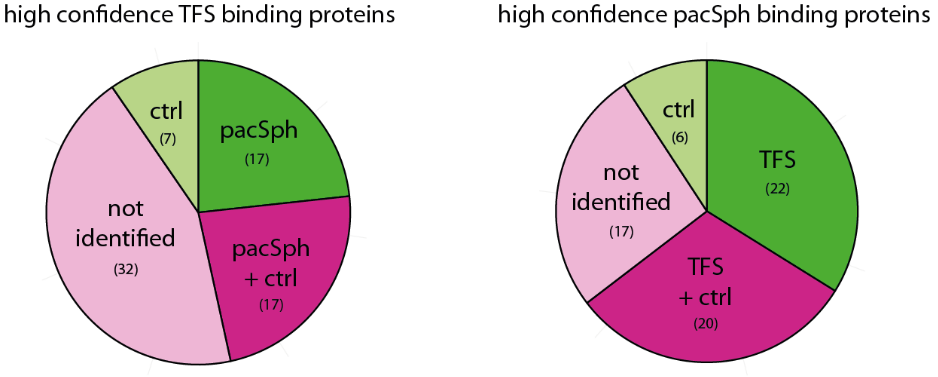

Figure 2.26 Prevalence of Sph binding proteins identified with TFS in the pacSph screen and vice versa. High confidence TFS-binding proteins (n=73) were examined if they were identified solely with pacSph, in pacSph and control (=pacFA), only in control conditions (ctrl) or not identified at all in 3 screens performed by Per Haberkant[209]. On the other hand, high confidence pacSph-binding proteins (n=65) were identified either only with TFS, with TFS but also control lipids (=TFDAG or TFFA), only in control conditions or not identified at all. The number of proteins is indicated in parentheses.

On the other hand, we examined a list of 65 high-confidence proteins which were uniquely identified in all three pacSph screens to see whether they were also detected using the TFS probe (Figure 2.26, right-hand side). Indeed, a third of the proteins were also detected by TFS, but not by TFFA or TFDAG. This again demonstrated the reproducibility of this crosslinking approach and helped to recognize this subset as Sph-binding proteins. The identification of the nature of the lipid crosslinked to these proteins is a major challenge in the bifunctional lipid field which has not previously been addressed. The discrepancy of 5 proteins in the green subsets of Figure 2.26 is explained by lower confidence proteins which were identified in only one or two screens. These proteins were not counted as high confidence proteins but were still considered as TFS- or pacSph-binding proteins in the making of Figure 2.26. Another 20 high-confidence pacSph binding proteins were identified with the TFS probe and additionally with TFDAG, TFFA or both probes. Again, some of these represent potential dual specificity proteins for Sph and SAG or Sph and arachidonic acid, which could not be identified using the pacFA precursor. Others, as well as the 6 proteins in control conditions, could be false positive results from the pacSph screen. The portion of 17 proteins identified with pacSph but not with any of the trifunctional probes represent proteins interacting specifically with higher sphingolipids such as Cer, SM or GSL.

2.2.6. The subcellular localization of Sph- and DAG-binding proteins matches with lipid localization

In order to determine at which subcellular compartments these newly identified high-confidence Sph-and DAG-binding proteins reside, we subjected them to an automatic GO-Term analysis using the BiomaRt package[211] in R and extracted the cellular compartment annotations (Figure 2.27). It should be mentioned that each protein is usually annotated to more than one subcellular compartment GO-Term (e.g endoplasmic reticulum, endoplasmic reticulum membrane, integral component of membrane, nuclear membrane, membrane for ceramide synthase 2). Only a small subset of these terms was queried in the automated analysis (see y-axis of Figure 2.27). Therefore, the percentage values on the x-axis do not add up to 100 %.

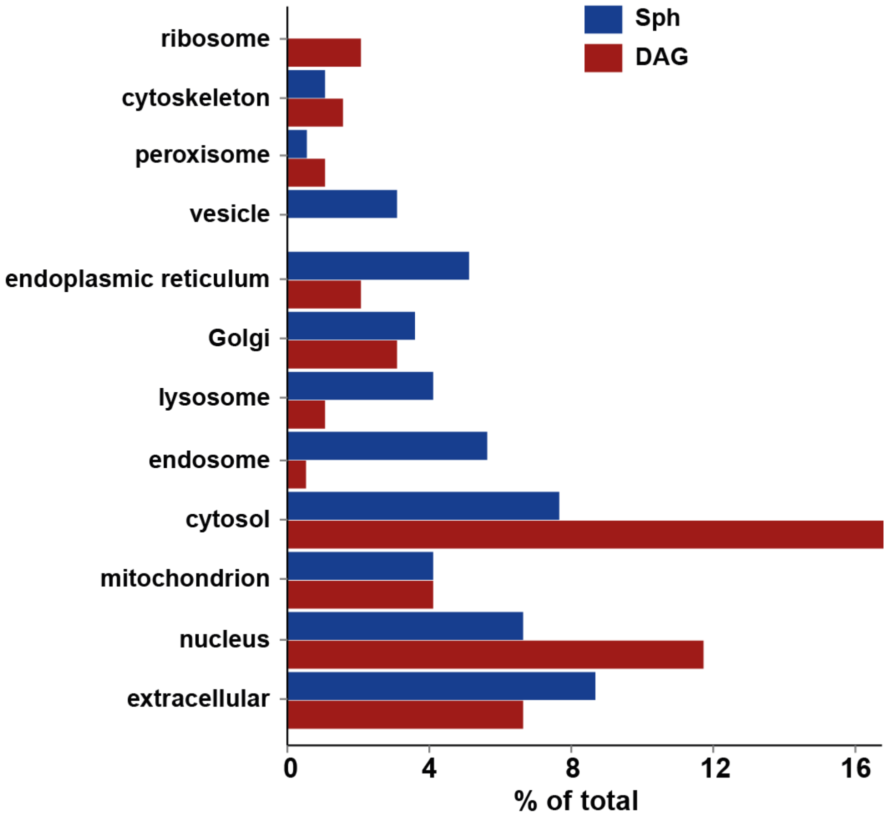

Figure 2.27 Localizations of high confidence proteins. Cellular compartment annotations of GO-terms of putative Sph- (n=73) and DAG-binding proteins (n=228).

This analysis revealed that most DAG-binding proteins resided in cytosolic and nuclear localizations and that they were almost completely absent from the endosomal/lysosomal system. Sph-binding proteins, on the other hand, were enriched along the endocytic pathway, with a higher percentage in endosomes/lysosomes compared to DAG-binding proteins. It is also worth noting that a substantial portion of putative Sph- and DAG-binders seem to be secreted to the extracellular space.

In order to compare whether the localizations derived from GO-term annotations coincided with the localization of the lipids after uncaging, we probed the subcellular locations of TFS, TFDAG and TFFA immediately after crosslinking by fixing the cells, washing away non-crosslinked lipids to reduce the background and subjecting the protein-lipid complexes to click-reaction with Alexa488-azide (Figure 2.28). In agreement with the oucomes of GO-term annotations, Sph was observed in the perinuclear region as well as in vesicular structures which co-localized with the late endosomal/lysosomal marker LAMP1.

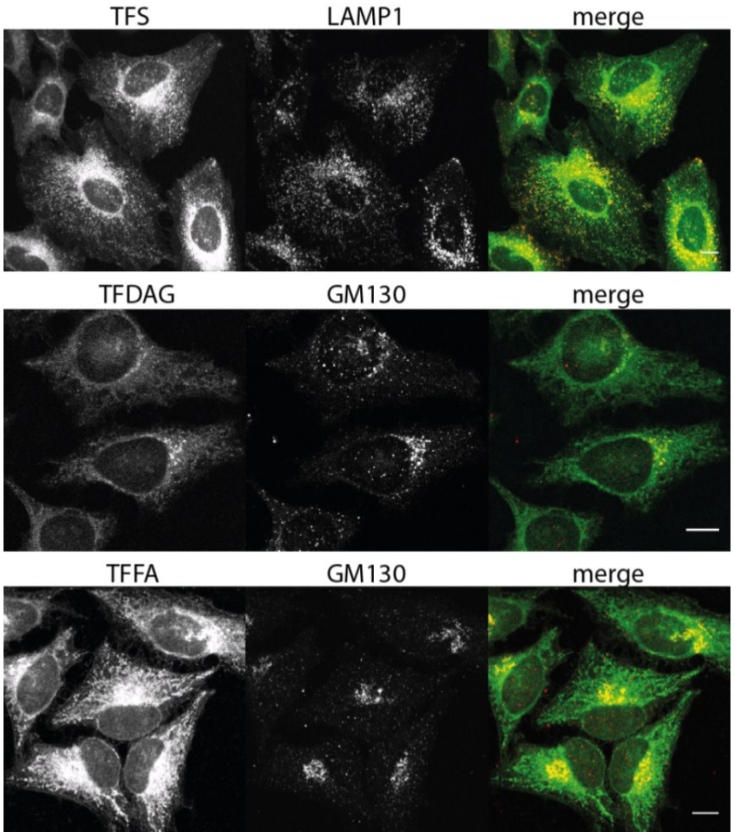

Figure 2.28 The subcellular localizations of Sph, DAG and FA are markedly different. Confocal images of HeLa cells. Alexa488-azide-conjugated lipids are shown in gray (left hand side) and green (merged image). Late endosomes/lysosomes and the Golgi apparatus are visualized by the LAMP1 and GM130 antibodies, respectively in gray (middle image) and red (merged image). The scale bars represent 10 µm.

Surprisingly, the intensity of DAG staining was much reduced compared to Sph and FA in this experiment, even though the trifunctional lipids were added in such concentrations that similar loading was achieved (see chapter 2.2.3). We speculate that this was primarily due to an artifact in the fixation procedure we used, because it is known that methanol fixation can extract nuclear and cytosolic proteins[212]. It is likely that the majority of DAG was crosslinked to cytosolic proteins (according to the GO-annotations) and was therefore extracted during the fixation. DAG localized uniformly to internal membranes with a slightly higher fluorescent intensity in the Golgi area as shown by co-localization with the Golgi marker GM130. Similarly, TFFA showed staining of internal membranes with enriched intensities in the Golgi and perinuclear area. We concluded that the distribution of lipid-binding proteins corresponded to the distribution of the lipids themselves. This gave another hint towards the feasibility of the use of trifunctional lipids for identifying protein-lipid interactions in living cells.

2.2.7. Sph accumulates in the acidic compartments of NPC cellular models due to failed efflux

A major advantage of the trifunctional lipids is the ability to liberate the active probe in a temporally and spatially precise way. In contrast to bifunctional lipids, which are taken up by cells in their active form, and are therefore immediately metabolized, all trifunctional lipid molecules are liberated at once with a flash of light, giving a precise starting point for pulse-chase experiments in subcellular localization studies. Additionally, the lipids are liberated inside the cells, thereby bypassing the endocytic machinery or extracellular checkpoints. We decided to make use of these advantages to study the subcellular localization of Sph in the context of NPC disease, since Sph may be the first and potentially causative change following NPC inactivation[57]. Using bifunctional Sph, we showed in chapter 2.1.8 that Sph accumulated in the late endosomes / lysosomes of NPC cells and that Sph did not escape these vesicles over time. A weakness of the bifunctional Sph method was that the endolysosomal localization was observed solely because the compound was taken up by endocytosis and then trapped in these vesicles due to protonation of the free amino group at low pH.

Using the TFS probe, the Sph localization in HeLa cells was examined and it was found that Sph indeed localized to the perinuclear region as well as to late endosomes / lysosomes at 0 min chase time (i.e. the time between uncaging and crosslinking) (see Figure 2.29). At chase times of 10 min or 30 min, the TFS probe no longer showed co-localization with LAMP1, but labelling of ER and Golgi (co-localization data not shown). This is in line with observations made by Per Haberkant using the bifunctional Sph[209] and indicates that Sph escaped from the acidic vesicles during this time and relocated to the ER where different ceramide synthases process Sph to Cer[33]. The Golgi staining represented further metabolism of Cer to SM and GlcCer, which is known to occur at the Golgi apparatus[34]. This experiment showed that even when Sph was released from anywhere within the cell, it rapidly re-localized to the endosomes/lysosomes, indicating a transport mechanism (either active transport or passive diffusion) of Sph to its endogenous localization.

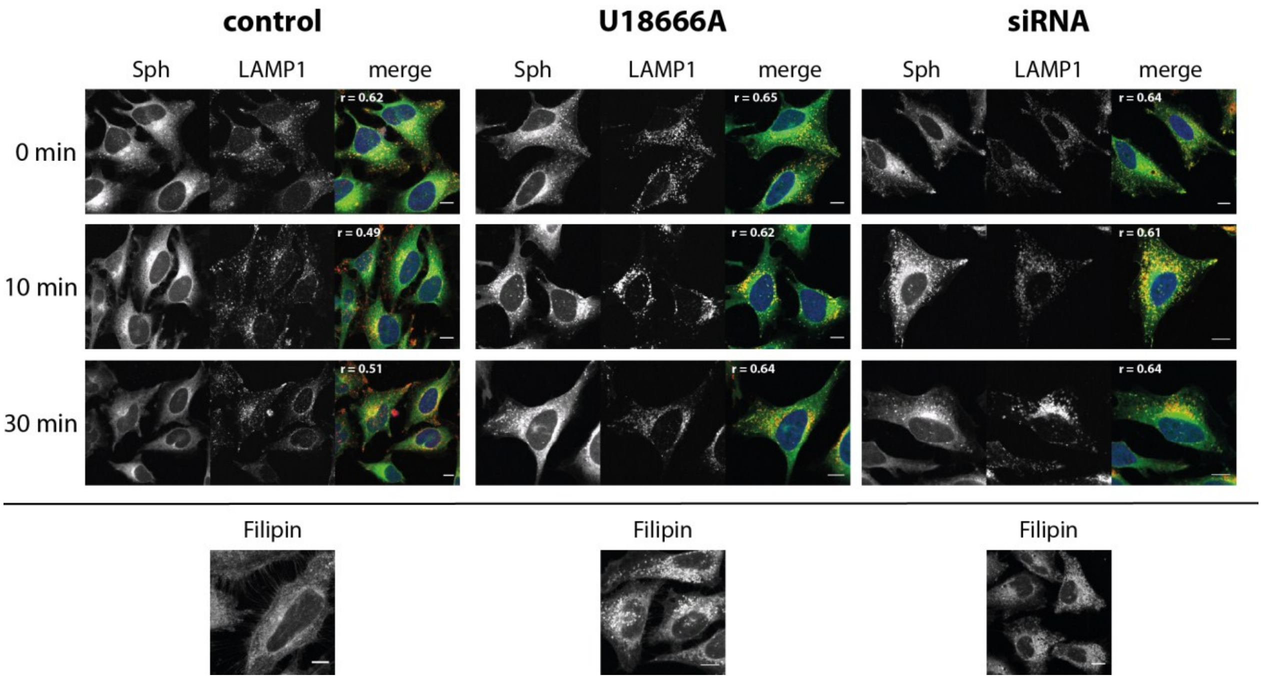

Figure 2.29 Sph is retained at endolysosomes in a cellular model of NPC disease. Confocal microscopy images of HeLa cells incubated with TFS (clicked to Alexa488-azide, green in the merged image). Late endosomes/lysosomes are shown in red in the merged image. For each condition, the distribution of free cholesterol was visualized by Filipin staining. The scale bars represent 10 µm. Pearson coefficient is indicated in top left corner of the merged image.

We next induced the NPC cellular phenotype in HeLa cells by employing the amphiphilic, hydrophobic amine U18666A, which partially disrupts NPC1 function[213]. The distribution of Sph was detected via the TFS probe (Figure 2.29, middle panel). At 0 min chase, Sph was visibly enriched in late endosomes / lysosomes, which were larger than in control conditions. Longer chase times of 10 min and 30 min, respectively still showed a marked late endosomal / lysosomal staining, indicating a defect in the efflux of Sph from the acidic compartments. Similar results were obtained by knock-down of NPC1 using an RNAi approach, which again gave rise to larger and more numerous endolysosomal vesicles compared to control conditions. The successful induction of the NPC phenotype in both cases (U18666A and siRNA) was confirmed by cholesterol staining using Filipin. Taken together, these results showed that Sph accumulated in late endosomes / lysosomes of NPC due to failed Sph efflux. The TFS probe enabled us to faithfully visualize the distribution of Sph in cells for the first time and we continued to use it in other models of NPC to check for Sph accumulation.

Another, commonly used model of the NPC disease is Chinese hamster ovary (CHO) cells, which are deleted of the NPC1 locus (M12)[214]. As control, we used M12 cells which are stably overexpressing the NPC1 protein (CHO/NPC1)[214]. M12 cells have been shown to accumulate cholesterol and to mimic the NPC phenotype, whereas CHO/NPC1 cells do not show increased Filipin staining even though the total cholesterol content of these cells is higher[214]. In order to investigate whether M12 cells reproduce the full NPC phenotype (i.e. also accumulated Sph), we probed the subcellular localization of Sph in these cells versus CHO/NPC1 cells using the TFS probe (Figure 2.30) at a chase time of 10 min because this already showed a clear difference between control and NPC condition.

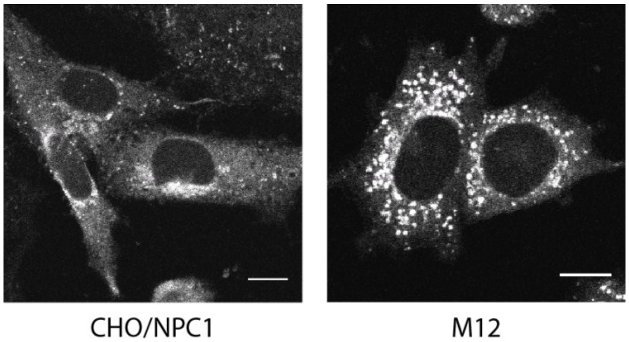

Figure 2.30 Sph also accumulated in CHO model of NPC. Confocal microscopy images of CHO/NPC1 and M12 cells labelled with TFS at chase times of 10 min. Scale bars represent 10 µm.

As expected, M12 cells accumulated Sph in enlarged late endosomes / lysosomes typical for the NPC cellular phenotype. In contrast, NPC1 overexpressing cells showed a mostly perinuclear / Golgi staining, indicating that Sph escaped from the acidic compartments and was transported to the Golgi for further modification, in line with observations made in HeLa cells. We concluded that the deletion of the NPC1 locus in CHO cells led to accumulation of Sph as well as cholesterol[214] in the late endosomes / lysosomes of these cells. This defect could be rescued by overexpression of the NPC1 protein, which restored Sph traffic and metabolism.

2.2.8. The rate of Sph transport in NPC patients correlated with the severity of their symptoms

The clinical presentation of the NPC disease can vary dramatically in age of onset and severity of the neurological phenotypes[215] and prediction of disease progression is challenging. Genotype-phenotype correlation is limited because most patient mutations are heterozygous. However, some of the over 200 known NPC mutations have been shown to correlate with disease severity[41,43,216]. The correlation between cellular trafficking defects or lipid accumulation with clinical presentation is very poor and many efforts have been made to identify biomarkers for NPC which would allow prediction and monitoring disease progression[217–219]. Here we investigated the Sph accumulation in fibroblasts derived from skin biopsies of NPC patients exhibiting a range of neurological symptoms to see whether the extent of Sph accumulation correlated with the severity of the disease. The confocal microscopy images are shown in Figure 2.31.

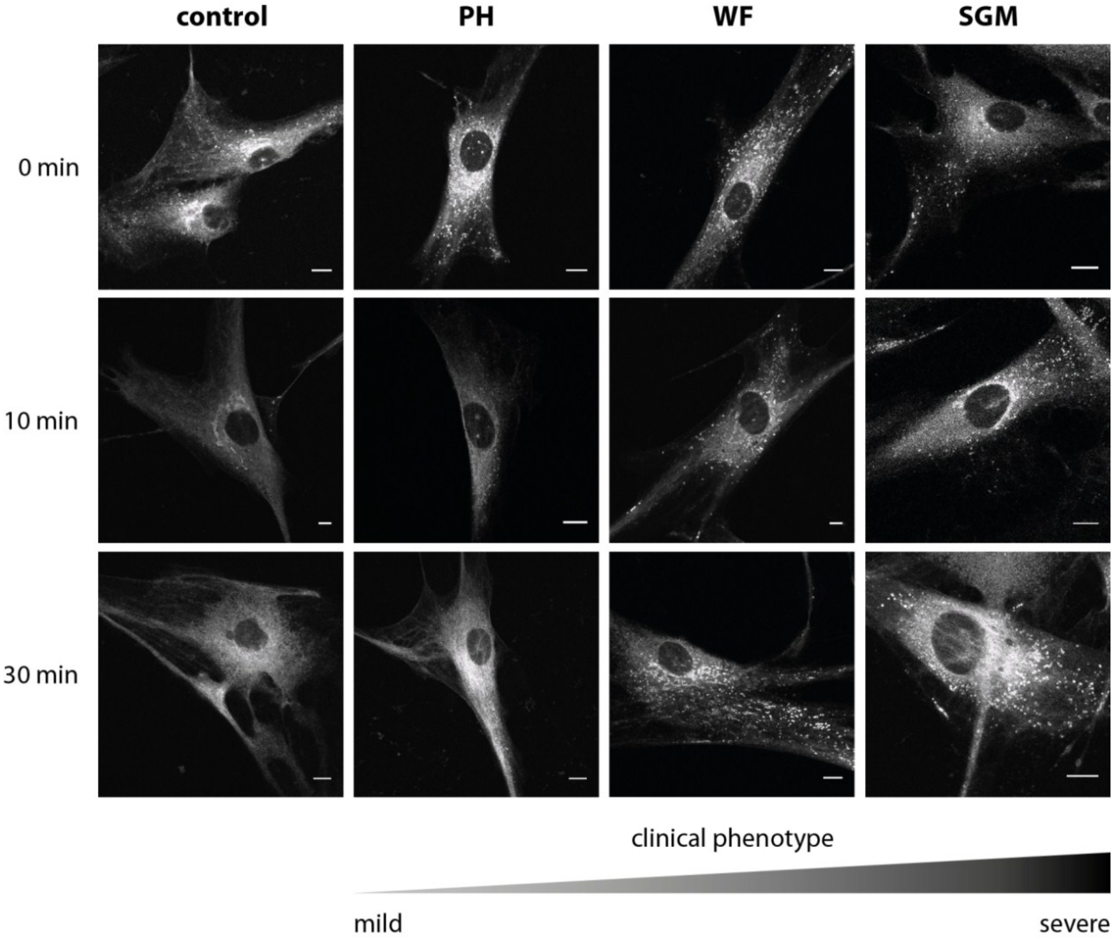

Figure 2.31 Lysosomal Sph efflux varied with NPC disease severity. Confocal microscopy images of NPC patient fibroblasts at various chase times. Cell lines were taken from patients exhibiting very mild symptoms (PH) to and intermediary phenotype (WF) and the severest phenotype seen to date (SGM). The scale bars represent 10 µm.

The initial Sph localization (at 0 min chase) was similar in all patient cells as well as in control fibroblasts and showed Sph mostly in late endosomes/lysosomes as well as in the perinuclear area. No significant difference in fluorescence intensity or number of labelled vesicles could be observed. However, all patient cells showed brighter lysosomal staining compared to control cells.

The rate efflux of Sph from these acidic vesicles, however, differed markedly between the different cell lines. At 10 min chase and 30 min chase, no more vesicular staining was observed in control cells. The fluorescent signal stemmed from internal membranes with a slight enrichment in Golgi staining, in line with observations made in HeLa and CHO cells (chapter 2.2.7.). Surprisingly, NPC PH cells (derived from a patient with mild clinical symptoms) did not show strong retention of Sph in late endosomes/lysosomes as observed in other NPC models (CHO/NPC1 or HeLa cells treated with U18666A or NPC1 siRNA). At 10 min chase, the fluorescent intensity in the endolysosomal vesicles was much reduced compared to 0 min and most of the staining stemmed from internal membranes, just as observed in control cells. After 30 min, only a few vesicles remained fluorescent and NPC PH cells resembled control cells with respect to the uniformity of internal membrane staining. It appears the NPC1 mutations in this patient (R978C point mutation, IVS21-2 A>G splice site mutation) did not critically affect the capabilities of the acidic vesicles to efflux Sph (and potentially other lipids).

In contrast, cells derived from patients with more severe phenotypes (WF and SGM) retained Sph accumulation in late endosomes / lysosomes after 30 min chase, indicative of a failed efflux of Sph from the acidic compartment. These findings constituted a promising first step towards establishing the TFS Sph efflux assay as a new diagnostic tool predicting the severity of the NPC disease in different patients. Further efforts employing cells from more patients and optimized chase times should confirm whether the rate of Sph transport from the late endosomes / lysosomes correlates with the severity of neurological symptoms observed in NPC patients.

2.2.9. Ultrastructural examinations of NPC

In order to examine the storage defect in NPC cells more closely, we investigated patient and control fibroblasts on the ultrastructural level using cryo-electron microscopy (cryo-EM). All EM sample preparation and analysis steps in this chapter were performed by Martina Schifferer in our group.

First, we analyzed samples by Transmission Electron Tomography (TEM). Control and NPC-WF fibroblasts were high-pressure frozen, embedded in Lowicryl and thick-sectioned (300 nm) and visualized by TEM. Figure 2.32 reveals a high abundance of very large (> 500 nm diameter) multivesicular bodies (MVB) in both control and NPC-WF cells. While the electron density in control MVBs was more homogenously distributed, NPC cells showed a striking enrichment of electron dense material in intraluminal vesicles (ILV).

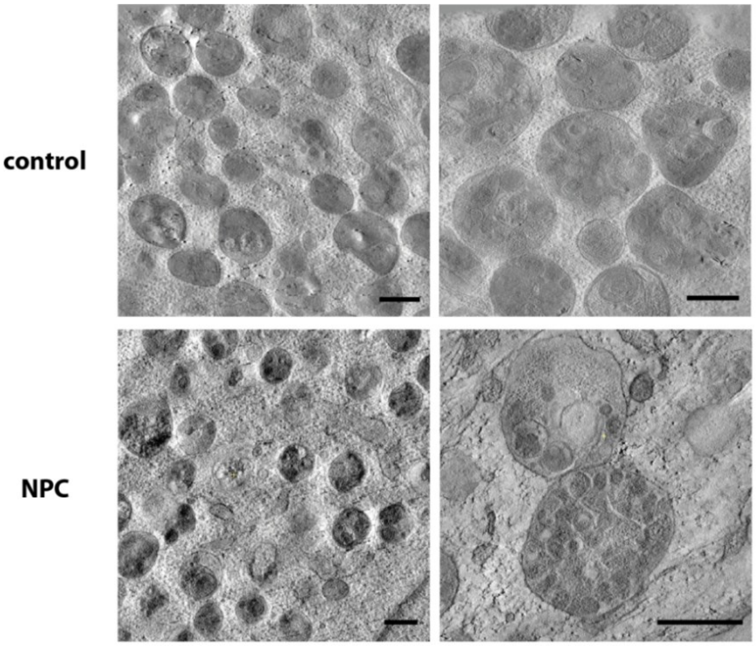

Figure 2.32 NPC cells show multivesicular bodies with high electron density. TEM images of control and NPC-WF fibroblasts. The scale bars represent 500 nm.

A close-up of NPC MVBs (Figure 2.32, bottom right image) revealed tight packing of many electron-dense ILVs, indicative of ILVs filled with storage material. These electron-dense vesicles may be the site of lipid accumulation in NPC disease.

To investigate whether Sph was indeed present in the ILVs, we used correlative light and electron microscopy (CLEM) on NPC-WF cells. We visualized Sph localization by clicking a fluorescent dye (Alexa594-azide) to the crosslinked TFS probe in PFA-fixed cells before high-pressure freezing. Samples were embedded in Lowicryl, thick sectioned and incubated with 50 nm Tetraspecks, both fluorescent and electron dense beads serving as landmarks for correlation fluorescent and electron microscopy images[220]. Figure 2.33 shows a representative correlation and confirms that Sph was present in MVBs of NPC-WF cells. Its distribution was not homogenous over the whole MVB, but enriched in single ILVs.

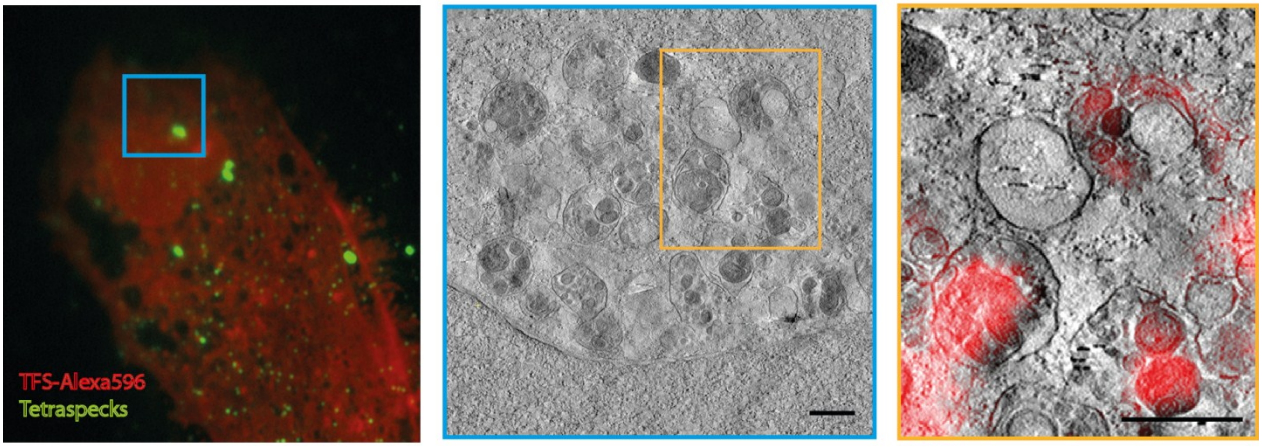

Figure 2.33 Sph is localized to intraluminal vesicles in NPC. CLEM images of NPC-WF fibroblasts labelled with TFS. The scale bars represent 500 nm.

This is further evidence consistent with the widely accepted hypothesis that fusion events are hindered in the NPC disease[55,57]. Sph and other storage materials are retained at the late endosomal / lysosomal stage and cannot be metabolized further. We hypothesize that accumulation of such ILVs in the late endosomes / lysosomes of NPC cells leads to lysosomal stress and weaken lysosomal membrane stability. Several of the storage lipids in NPC such as Sph[221] and SM[222] have already been shown to contribute to lysosomal destabilization. This might also explain the observation that inhibition of autophagy ameliorated the NPC phenotype in NPC1-null cells[200], because this reduced the delivery of substrates to compromised lysosomes.

2.2.10. Conclusion and outlook

The bifunctional lipid technology is currently one of the best methods to screen for soluble and transmembrane spanning lipid-binding proteins in a native cellular environment. Due to the synthetic effort necessary for creating these lipids, only few studies have been reported so far[150–152]. However, the power and applicability of this concept is gaining attraction as a whole new class of drugable proteins has been identified recently using bifunctional endocannabinoids[152]. Additionally, bifunctional lipids are optimally suited to probe the subcellular localization of lipids since the fluorescent group is only added after crosslinking and fixation and therefore does not alter the physicochemical properties of the lipid probe. This has been successfully demonstrated in cultured cells as well as in whole organisms[151].

The only drawback of this method comes from its biggest advantage: The bifunctional probe mimics endogenous lipids so closely that it takes part in cellular metabolism and is converted to multiple lipid species, thereby yielding mixed protein interactomes of different lipid probes. Here, we developed a novel method which retained all the advantages of bifunctional lipids and additionally circumvented ongoing lipid metabolism before crosslinking and identification of interacting proteins, by adding a caging group to bifunctional lipids. This technology ensured the inactivity of these trifunctional probes during delivery to the cells. Two subsequent photoreactions carried out on the same molecule allowed for the liberation of the active probe to its binding partners immediately before crosslinking. We demonstrated the orthogonality of the uncaging and photo-crosslinking reaction by NMR spectroscopy and showed that the liberated species are highly bioactive by live-cell microscopy.

One possible concern was the mislocalization of the trifunctional probe due to the lipophilic properties of the DEAC cage group. Indeed, all investigated trifunctional lipids exhibited the same non-discriminatory endomembrane staining before uncaging, which does not represent endogenous lipid localization. However, the conditions used for proteomic screens (2 min uncaging immediately followed by 2 min crosslinking) resulted in complete rearrangement of the trifunctional lipids inside the cells so that TFS was crosslinked mostly at endosomes and lysosomes while TFDAG exhibited cytosolic and ER staining. This hints towards a rapid transport mechanism of the liberated species to their endogenous locations, either passively by diffusion or actively via the action of lipid transfer proteins. Interestingly, we found several known transfer proteins (such as STARD3, STARD7 or PITPβ) and some unknown lipid transfer proteins in the Sph interactome, indicating that Sph either regulates these proteins or is transported by these proteins. Further experiments are needed to confirm these hypotheses.

Analysis of the protein interactomes of three different trifunctional lipids revealed a high overlap of proteins which were identified in all three conditions. This high background has been reported in other studies[151,152] and stemmed either from unspecific crosslinking of membrane proteins to the surrounding lipid layer, or from non-specific binding of the proteins to neutravidin beads during the enrichment step. Therefore, it is imperative to employ control lipids to exclude these background proteins. Additionally, these non-specific proteins also impeded the identification of proteins crosslinked at lower numbers due to the cut-off at the mass spectrometer. The same effect was observed in experiments with bifunctional lipids which were incorporated into many bifunctional metabolites. The increased complexity of the proteome led to the loss of proteins present in low copy numbers. We showed this effect by comparing high confidence TFS binding proteins with high confidence pacSph binding proteins. Almost half of the putative TFS-binding proteins were not identified at all when using pacSph. In conclusion, we developed a novel method to obtain protein interactomes of single lipid species with a much higher coverage than by using bifunctional lipids.

Interestingly, we also found TPC1, but not other lysosomal calcium channels such as TPC2 or TRPML1 crosslinked to TFS. This provides evidence of a direct interaction between Sph and TPC1 and explains the immediate effect of Sph on lysosomal calcium signaling. The TFS probe was further used to determine the binding site of Sph to TPC1. However, the TFS-Sph interaction was only detected in one screen and with low spectral counts and therefore needs to be further validated in future experiments.

We also demonstrated the power of trifunctional lipids as probes to investigate the subcellular localization and transport of lipids through the cell. Using TFS, we confirmed the late endosomal / lysosomal localization of Sph and its enrichment in different cellular models of the NPC disease, showing it was not an artifact from the endocytic uptake of the previously used bifunctional Sph. The TFS probe was also used in precise pulse-chase experiments to follow the efflux of Sph from the acidic compartments. This new assay was used to examine the differences between fibroblasts derived from NPC patients with varying disease severity. We showed that fibroblasts derived from the patient with the mildest phenotype had the ability to efflux Sph from the endolysosomes almost as fast as control cells, while NPC patients with more severe symptoms showed accumulation of Sph in acidic vesicles. More in-depth investigations involving cells from more patients and finer chase times should confirm the suitability of this assay as a biomarker for predicting NPC disease severity based on the extent of Sph storage.

Finally, we employed TFS to investigate Sph localization in NPC fibroblasts by correlative light- and electron microscopy. This is the first report visualizing the localization of a lipid on the ultrastructural level. We showed an accumulation of Sph in intraluminal vesicles of multivesicular bodies / late endosomes in NPC fibroblasts, an observation which is consistent with the long-standing hypothesis that NPC cells exhibit a trafficking block at the late endosomal / lysosomal stage[55,57]. Apart from the insights into the pathophysiology of NPC, we also believe that this new method will find application in many more areas where the ultrastructural localization of lipids is of interest.

Chapter 3 - Experimental methods

3.1. Reagents

Common laboratory chemicals were purchased from commercial sources (Acros, Fluka, Merck, Sigma-Aldrich or VWR) at highest available grade and were used without further purification. D-erythro sphingosine and D-erythro dihydrosphingosine, the sphingosine kinase inhibitor SKI-II, Xestospongin C and GPN were obtained from Biomol (Hamburg, DE). 7-Diethylamino-4-hydroxymethylcoumarin was a kind gift from Rainer Müller (EMBL Heidelberg, DE). Deuterated solvents for NMR analysis were purchased from Deutero (Karlsruhe, DE). Sphingosine kinase inhibitor *N,N*-dimethylsphingosine was obtained from Sigma-Aldrich. NAADP-antagonist Ned-19 was purchased from Tocris Biosciences (Bristol, UK). FTY720 was a kind gift from Dr. Fran Platt (University of Oxford, UK). The fluorescent calcium indicator Fluo-4-AM and Alexa488-azide were obtained from Life Technologies (Thermo Fisher Scientific, Waltham, USA).

3.2. Chemical synthesis

3.1.1. General synthetic procedures

All reactions were carried out using dry solvents under inert atmosphere in the dark. Thin layer chromatography (TLC) was performed on plates of silica gel (Merck, 60 F254) and visualized using UV light (254 nm or 366 nm) or a solution of phosphomolybdic acid in EtOH (10 % w/v). Preparative column chromatography was carried out using Merck silica gel 60 (grain size 0.063 – 0.200 nm) under a pressure of <1.5 bar. ^{1}H-NMR spectroscopic measurements were conducted on a 400 MHz Bruker UltraShield^{TM} spectrometer at 25°C. ^{13}C-NMR measurments were performed on a 500 MHz Bruker UltraShield^{TM} spectrometer at 25°C and were broadband hydrogen decoupled. ^{1}H- and ^{13}C-NMR spectra are shown in Appendix A. Chemical shifts are given in ppm referenced to the residual solvent peak. *J* values are given in Hz and splitting patterns are designated using s for singlet, d for doublet, t for triplet, q for quartet, m for mulitplet and b for broad signal. High-resolution mass spectra were recorded on a Finnigan LCQ quadrupole ion trap at the Organic Chemistry Institute of the University of Heidelberg

3.1.2. 7-(Diethylamino)-coumarin-4-yl)-methyl-chloroformate[223]

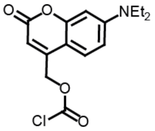

A solution of 7-diethylamino-4-hydroxymethylene-coumarin (48 mg, 194 µmol) in 2 mL dry THF was cooled to 0°C. DIPEA (0.1 µL, 575 µmol) and phosgene (300 µL, 610 µmol) were added dropwise and stirred in the dark for 2 h at 0 °C. The reaction mixture was extracted with EtOAc/H_2O (1:1, 75 mL), the layers were separated, the organic layer was washed with brine and dried using Na_2SO_4. The solvent was removed under reduced pressure and the product was dried further under high vacuum conditions. 7-(Diethylamino)-coumarin-4-yl]-methyl chloroformate was used without further purification.

3.1.3. (7-(Diethylamino)-2-oxo-2H-chromen-4-yl ((2R,3S,E)-1,3-dihydroxyoctadec-4-en-2-yl)carbamate)

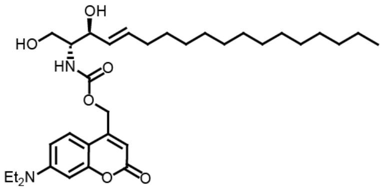

Sph-Cou

To a solution of D-erythro-sphingosine (30 mg, 100 µmol) in 2 mL dry THF, TEA (70 µL, 500 µmol) and a solution of 7-diethylamino-coumarin-4-yl-methyl chloroformate (46 mg, 148 µmol) in 1 mL dry THF were added. The mixture was stirred at RT for 1 h in the dark. EtOAc (50 mL) was added to stop the reaction and the mixture was washed twice with citric acid (5 % w/v, 25 mL) and twice with saturated $NaHCO_3$. The organic layer was dried with Na_2SO_4 and the solvent was removed under reduced pressure. The residue was purified by repeated flash chromatography (first column: eluent: DCM/MeOH 13:1, second column: eluent: cyclohexane/EtOAc 1:5 (+1 % TEA)). Sph-Cou was obtained as yellow oil (26 mg, 45 µmol, 45 % over two steps)

^{1}H NMR (400 MHz, $CDCl_3$) δ = 7.29 (d, *J*=8.9, 1H), 6.58 (d, *J*=8.7, 1H), 6.50 (s, 1H), 6.14 (s, 1H), 5.96 (d, *J*=8.3, 1H), 5.80 (dd, *J*=14.6, 7.2, 1H), 5.55 (dd, *J*=15.2, 6.1, 1H), 5.22 (s, 2H), 4.39 (s, 1H), 4.05 – 3.96 (m, 1H), 3.76 (d, *J*=11.6, 1H), 3.68 (q, *J*=3.8, 1H), 3.40 (q, *J*=7.0, 3H), 3.06 (s, 1H), 2.05 (dd, *J*=13.5, 6.6, 2H), 1.41 – 1.10 (m, 28H), 0.87 (t, J=6.6, 3H). ^{13}C NMR (126 MHz, $CDCl_3$) δ = 162.15, 156.18, 155.60, 150.40, 134.45, 128.70, 126.78, 124.43, 108.98, 106.16, 98.13, 74.75, 74.17, 66.85, 62.21, 61.89, 55.73, 44.96, 32.29, 31.93, 29.70, 29.67, 29.64, 29.51, 29.37, 29.22, 29.10, 22.70, 14.12, 12.40.

HRMS for $C_{33}H_{53}N_2O_6^+$ calculated: 573.39036; found: 573.39027

3.1.4. (2,4-Dimethoxy-6-nitrophenyl-((2R,3S,E)-1,3-dihydroxyoctadec-4-en-2-yl)-carbamate)

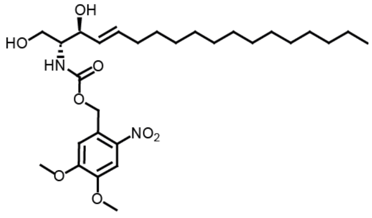

Sph-NB

A solution of D-erythro-sphingosine (30 mg, 100 µmol) in 2 mL dry THF and TEA (70 µL, 500 µmol) was stirred during dropwise addition of 4,5-dimethoxy-2-nitrobenzyl-chloroformate (41 mg, 150 µmol) in 2 mL dry THF. The mixture was stirred at RT for 1h in the dark. EtOAc (50 mL) was added and the mixture was washed twice with citric acid (5 % w/v, 25 mL) and twice with saturated $NaHCO_3$. The organic layer was dried with Na_2SO_4 and the solvent was removed under reduced pressure. The residue was purified by chromatography (eluent: cyclohexane/EtOAc 1:5 (+1 % TEA)). Sph-NB was a colorless oil (51,4 mg, 95 µmol, 95 %).

^{1}H NMR (400 MHz, $CDCl_3$) δ = 7.70 (s, 1H), 7.02 (s, 1H), 5.84 – 5.75 (m, 2H), 5.55 (d, *J*=6.0, 1H), 5.51 (s, 2H), 4.38 (s, 1H), 4.01 (s, 1H), 3.98 (s, 3H), 3.95 (s, 3H), 3.73 (d, *J*=11.5, 1H), 3.67 (s, 1H), 2.39 (s, 2H), 2.12 – 1.96 (m, 2H), 1.42 – 1.13 (m, 22H), 0.87 (t, *J*=6.7, 3H) ^{13}C NMR (101 MHz, $CDCl_3$) δ = 155.99, 134.47, 128.58, 110.07, 108.15, 74.81, 63.78, 62.24, 56.52, 56.50, 56.40, 55.57, 32.28, 31.94, 31.92, 29.71, 29.68, 29.62, 29.48, 29.36, 29.22, 29.08, 22.71, 22.69, 14.13.

HRMS for $C_{28}H_{47}N_2O_8Na^+$ calculated: 561.31519, found: 561.31557

3.1.5. (7-(Diethylamino)-2-oxo-2H-chromen-4-yl-((2R,3S)-1,3-dihydroxyoctadecan-2-yl) carbamate)

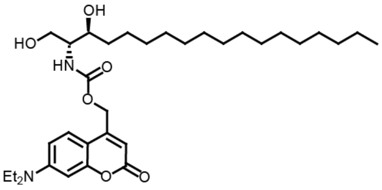

dhSph-Cou

To a solution of D-erythro-dihydrosphingosine (10 mg, 33 µmol) in 1 mL dry THF, DIPEA (23 µL, 230 µmol) and a solution of [7-(diethylamino)-coumarin-4-yl)-methyl chloroformate (15 mg, 50 µmol) in 0,5 mL dry THF were added. The mixture was stirred at RT for 1,5 h in the dark. EtOAc (20 mL) was added to stop the reaction and the mixture was washed twice with citric acid (5 % w/v, 10 mL) and twice with saturated $NaHCO_3$. The organic layer was dried with Na_2SO_4 and the solvent was removed under reduced pressure. The residue was purified by repeated flash chromatography (first column: eluent: DCM/MeOH 13:1, second column: eluent: cyclohexane/EtOAc 1:5). dhSph-Cou was obtained as yellow oil (14.5 mg, 25 µmol, 76 % over two steps)

^{1}H NMR (400 MHz, $CDCl_3$) δ = 7.27 (d, *J*=8.9 Hz, 1H), 6.56 (dd, *J*=9.0, 2.3, 1H), 6.49 (d, *J*=2.3, 1H), 6.14 (s, 1H), 6.08 (d, *J*=8.4, 1H), 5.22 (s, 2H), 4.07 (dd, *J*=11.4, 2.3, 1H), 3.82 (d, *J*=11.7, 2H), 3.66 (s, solvent THF), 3.62 (dd, *J*=8.1, 3.3, 1H), 3.40 (q, *J*=7.0, 4H),2,30 (t, J=7.6, solvent), 1.67 – 1.45 (m, 4H), 1.36 – 1.13 (m, 30H), 0.87 (t, *J*=6.7, 3H) ^{13}C NMR (126 MHz, $CDCl_3$) δ = 162.34, 156.17, 155.52, 150.60, 130.02, 129.77, 124.41, 108.83, 106.12, 105.90, 97.90, 74.36, 62.24, 61.83, 55.13, 51.44, 44.82, 34.55, 31.94, 29.71, 29.67, 29.61, 29.59, 29.37, 27.23, 25.99, 24.96, 22.70, 14.12, 12.43.

HRMS for $C_{33}H_{55}N_2O_6^+$ calculated: 575.40601; found: 575.40626

3.1.6. (7-(Diethylamino)-2-oxochromen-4-yl)methyl-((2*S*,3*R*,*E*)-1,3-dihydroxy-13-(3-(pent-4-yn-1-yl)-3*H*-diazirin-3-yl)tridec-4-ene-2-yl)carbamate

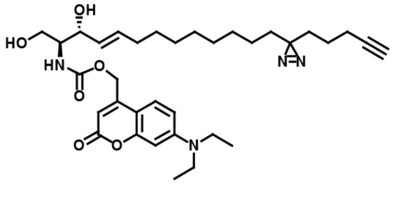

TFS

A solution of 20 mg (59.7 µmol) photoactivatable and clickable sphingosine (Per Haberkant) in 1.5 mL THF was cooled to 0 °C and 52 µL DIPEA (0.3 mmol) was added. [7-(diethylamino)-coumarin-4-yl)-methyl chloroformate (28 mg, 0.09 mmol) in 1 mL dry THF were added and stirred at room temperature for 1 h. The product was extracted with 30 mL EtOAc and 30 mL citric acid (5 % w/v) and washed twice with 30 mL citric acid, once with $NaHCO_3$ and once with brine. The organic phase was dried over Na_2SO_4 and the solvent was removed under reduced pressure. The residue was purified by flash chromatography (first column: eluent: cyclohexane/EtOAc 1:1, second column: eluent: DCM/MeOH 14:1) which gave the title compound as a yellow oil (35 mg, 57.5 mmol, 96 % yield).

^{1}H NMR (500 MHz, $CDCl_3$) δ = 7.29 (d, *J*=9.0, 1H), 6.58 (dd, *J*=8.9, 2.2, 1H), 6.50 (d, *J*=2.2, 1H), 6.14 (s, 1H), 5.89 (d, *J*=6.8, 1H), 5.84 – 5.75 (m, 1H), 5.55 (dd, *J*=15.2, 6.1, 1H), 5.23 (s, 2H), 4.39 (s, 1H), 4.02 (dd, *J*=11.2, 2.8, 1H), 3.77 (dd, *J*=11.5, 3.0, 1H), 3.69 (dd, *J*=7.8, 3.3, 1H), 3.66 – 3.59 (m, 1H), 3.41 (q, *J*=7.0, 4H), 2.56 (s, 2H), 2.15 (td, *J*=6.9, 2.6, 2H), 2.05 (dd, *J*=13.9, 7.0, 3H), 1.94 (t, *J*=2.6, 1H), 1.48 (dd, *J*=9.1, 6.6, 3H), 1.39 – 1.29 (m, 9H), 1.28 – 1.15 (m, 28H), 1.10 – 1.02 (m, 5H), 0.91 – 0.77 (m, 4H)

^{13}C NMR (126 MHz, $CDCl_3$) δ = 162.34, 156.17, 155.63, 150.63, 134.39, 128.68, 124.40, 108.87, 105.92, 97.91, 83.49, 77.28, 77.03, 76.77, 74.72, 68.88, 62.12, 61.88, 55.67, 44.83, 32.85, 32.24, 31.85, 29.71, 29.31, 29.28, 29.17, 29.10, 29.02, 28.46, 23.81, 22.77, 17.97, 14.12, 12.43.

HRMS calculated for $C_{34}H_{49}N_4O_6^+$: 609.36521, found: 609.36508

3.2. Buffers and media

3.2.1. Bacterial culture media

LB medium

Autoclaved Luria-Bertani (LB) medium was prepared by the media kitchen at EMBL according to following composition and stored at room temperature.

1 % (w/v) bacto trypton
0.5 % (w/v) bacto yeast extract
170 mM NaCl

The pH was adjusted to 7.6 using NaOH and the medium was supplemented with antibiotics (100 µg/mL ampicillin, 33 µg/mL chloramphenicol or 30 µg/mL kanamycin) immediately prior to use.

LB agarose plates

LB agarose plates were prepared by the media kitchen with 1.5 % (w/v) bacto agar in LB, supplemented with antibiotics (100 µg/mL ampicillin, 33 µg/mL chloramphenicol or 30 µg/mL kanamycin) and stored at 4 °C.

SOC medium

Super Optimal broth with Catabolite repression (SOC) medium was prepared by the media kitchen according to following composition, pH adjusted to 7.0, autoclaved and stored at 4°C.

20 mM glucose
10 mM $MgCl_2$
10 mM $MgSO_4$
2.5 mM KCl
10 mM NaCl
2 % (w/v) bacto tryptone
0.5 % (w/v) bacto yeast extract

3.2.2. Buffers and solutions

PBS

137 mM NaCl
2.7 mM KCl
2 mM KH_2PO_4
10 mM Na_2PO_4
1 mM EDTA

PBS was prepared by the media kitchen at EMBL. It was adjusted to pH 7.4 using HCl and sterile filtered.

Imaging buffer

20 mM HEPES
115 mM NaCl
1.2 mM $MgCl_2$
1.2 mM K_2HPO_4
1.8 mM $CaCl_2$

The pH of the imaging buffer was adjusted to 7.4 using 1 M NaOH or 1 M HCl solution. Before each experiment, glucose was added to a final concentration of 0.2 % (w/v).

Lysis buffer

50 mM HEPES
50 mM NaCl
1 % (w/v) SDS
1x protease inhibitor cocktail (PIC)

The pH of the lysis buffer was adjusted to 8.5 before addition of SDS. One tablet of PIC was added to 50 mL lysis buffer immediately before use.

Amido Black solution

0.02 % (w/v) amido black
40 % (v/v) methanol
10 % (v/v) glacial acetic acid
50 % (v/v) H_2O

PHEM buffer

60 mM PIPES
5 mM HEPES
10 mM EGTA
2 mM $MgCl_2$

The buffer was adjusted to pH 6.9, sterile filtered and refrigerated before use.

Borate buffer (for lipidomics analysis)

200 mM boric acid
10 mM tris(2-carboxyethyl)-phosphine
10 mM ascorbic acid
33.7 µM $^{15}N^{13}C$ valine

The boric acid solution was adjusted to pH 8.8 before addition of the other components and sterile filtration.

3.2.3. Eukaryotic cell media

Standard culture medium

Dulbecco’s Modified Eagle Medium (DMEM) (4.5 g/L glucose, Gibco/Life Technologies)
10 % fetal calf serum (Sigma-Aldrich, Lot.-No. 032M3395)
2 mM L-glutamine (Gibco/Life Technologies)
1 % penicillin/streptomycin (Gibco/ Life Technologies)

HeLa cell culture medium

DMEM (1 g/L glucose, Gibco/Life Technologies)
10 % fetal calf serum (Sigma-Aldrich, Lot.-No. 032M3395)
1 % primocin (InvivoGen)

All media were sterile filtered and stored at 4 °C.

3.3. Cell culture

3.3.1. Eukaryotic cell lines

HeLa (human cervical adenocarcinoma cells, No. CCL-2)

ATCC / LGC Standards GmbH (Wesel, DE)

TPC1-KO (mouse embryonic fibroblasts from Tpcn1$^{-/-}$ mouse)
TPC2-KO (mouse embryonic fibroblasts from Tpcn2$^{-/-}$ mouse)
DKO (mouse embryonic fibroblasts from a Tpcn1$^{-/-}$, Tpcn2$^{-/-}$ double knockout mouse)
Ctrl MEF (mouse embryonic fibroblasts from a WT mouse)

Dr. Antony Galione (Department of Pharmacology, University of Oxford, UK)

Ctrl FB (human fibroblasts derived from healthy donor)
NPC-PH (human fibroblasts derived from NPC patient (#17))
NPC-WF (human fibroblasts derived from NPC patient (#22))
NPC-SGM (human fibroblasts derived from NPC patient (#25))

Dr. Forbes D. Porter (Section of Molecular Dysmorphology, NIHCD, Betheseda, USA)

CHO WT (Chinese hamster ovary cells)
CHO null (NPC1 null Chinese hamster ovary cells)
CHO OE (NPC1 overexpressing chinese hamster ovary cells)

Dr. Daniel Ory (Washinton University School of Medicine, St. Louis, USA)

Ctrl FB (human fibroblasts derived from healthy donor)
MLIV (human fibroblasts derived from mucolipidosis type IV patient)

Dr. Frances Platt (Department of Pharmacology, University of Oxford, UK)

All cells were kept in appropriate growth medium in a humidified incubator at 37 °C with 5 % CO_2 and were passaged 2 – 3 times per week. For live-cell imaging experiments, cells were seeded in 8-well Labtek dishes (Nunc/Thermo Scientific) 48 h prior to the experiment.

3.3.2. Transfection

For imaging experiments, cells in 8-well Labteks were transfected 24 h prior to the experiment using Fugene HD reagent (Promega), OPTIMEM medium (Gibco/Life Technologies) and 100 ng TFEB-GFP plasmid as well as 50 ng R-GECO plasmid per well according to the manufacturer's instructions.

3.4. Live-cell microscopy

3.4.1. Cell loading

Cells in 8-well Labteks at 70 – 80 % confluency were labelled with 100 µL of 5 µM Fluo4 AM (Molecular Probes) solution in imaging buffer at 37 °C for 30 min. 15 min prior to the start of the experiment, caged lipids (Sph-Cou, Sph-NB, dhSph-Cou or TFS) were added to a final concentration of 2 µM. The cells were then washed and kept in imaging buffer at 37 °C for the duration of the experiment.

3.4.2. Confocal time lapse microscopy and photoactivation

The fluorescence of the calcium indicator Fluo4 was monitored on a dual scanner confocal laser scanning microscope (Olympus FluoView 1200) using a 63x oil objective at 488 nm excitation and emission settings between 500 - 550 nm at an intverval of 1 s per frame. A baseline of 10 frames (= 10 s) was captured before photoactivation ('uncaging') in a circular region (10 pixel units diameter, 8.9 μm^2) inside the cells using the tornado function of the Olympus software. Coumarin-uncaging was carried out using the 405 nm laser line set to 50 % intensity for 3 s at 2 µs per pixel. For nitrobenzyl-uncaging, the 375 nm laser line was set to 100 % intensity and activated for 5 s at 2 µs per pixel.

3.4.3. Image analysis

For calcium measurements, time lapse images were analyzed using Fiji software (W. Rasband, NIH, USA) with the FluoQ macro [166] set to the following parameters:

Background subtraction method: Mean of an interactively selected ROI
Noise reduction / smoothing method: None
Threshold method: Interactively with ImageJ's built-in threshold window
ROI segmentation: Semi-automatically with binary mask modification
Calculate amplitude changes: Using maximum observed amplitude change

The maximum amplitude values were calculated by subjecting the raw traces to a central moving average. The maximal amplitude $\mathrm{x}^{\mathrm{max}}_{\mathrm{response}}$ of these smoothed traces was used to calculate the amplitude change in percent $\%\Delta_x^{max}$according to following formula:

$$\%\Delta_x^{max} = \frac{x_{response}^{max} - \bar{x}_{baseline}}{|\bar{x}_{baseline}|} * 100$$

The resulting intensity series/amplitude values represent mean values of whole cells and were further analyzed using R software[167].

3.4.4. Data anaylsis

The intensity/amplitudes values derived from the FluoQ macro were loaded in R and grouped according to lipid and condition (cell lines, inhibitors used). Single cell traces belonging to the same groups were summarized using a custom function called summarySE (see Appendix C.1) which calculated the mean as well as the standard error of the mean of all traces for every time point. Line and bar graphs were generated using the ggplot2 package in R[224].

3.5. Lipid analyses

3.5.1. Thin layer chromatographic analysis of caged lipids

HeLa cells were grown in 6 cm dishes (Nunc) to 85 – 95 % confluency and labelled with indicated concentrations of Sph-Cou in imaging buffer for the designated times. Cells were washed with PBS and scraped in 300 µL PBS. 600 µL MeOH and 150 µL $CHCl_3$ were added and the mixture was vortexed and centrifuged at 14 000 rpm for 3 min. The supernatant was transferred in a new vial, 300 µL $CHCl_3$ and 600 µL acetic acid (0.1 % v/v in water) were added and the mixture was vortexed and centrifuged at 14 000 rpm for 4 min. The (upper) aqueous phase as discarded and the organic phase was dried in a speed-vac at 30 °C for 15 min. The lipids were redissolved in 30 µL $CHCl_3$ and applied onto a 10 x 10 cm HPTLC Silica 60 glass plate (VWR) using the automatic Camaq system. TLC plates were developed using $CHCl_3$/MeOH/H_2O/AcOH 65:25:4:1 for 6 cm and then cyclohexane/ethylacetate 1:1 for 9 cm. Lipids containing the fluorescent cage group were visualized using a geldoc system.

3.5.2. Thin layer chromatographic analysis of clickable lipids

Cells were grown in 60 cm dishes to 85 – 95 % confluency and labelled with the snapshot probes or pacSph at 1 – 6 µM for the indicated times. After washing with PBS, the cells were transferred onto an ice block and UV-irradiated using a 450 – 1000 W high-pressure mercury lamp (Newport, USA) equipped with glass filters removing wavelengths below 345 nm and below 400 nm. The cells were irradiated with > 400 nm for 2.5 min and then immediately irradiated with > 350 nm for another 2.5 min. The cells were washed again and scraped in 300 µL PBS and mixed with 600 µL MeOH and 150 µL $CHCl_3$. The mixture was vortexed and centrifuged at 14 000 rpm for 3 min and the supernatant was transferred into a new vial. 300 µL $CHCl_3$ and 600 µL acetic acid (0.1 % v/v in water) were added, the mixture was again vortexed and centrifuged (14 000 rpm, 4 min) and the aqueous phase was discarded. The organic phase was dried in a speed-vac at 30 °C for 15 min. The lipids were dissolved in 7 µL $CHCl_3$ and 30 µL click-mixture (5 µL 44.5 mM 3-azido-7-hydroxycoumarin, 500 µL of 10 mM [acetonitrile]$_4$CuBF$_4$ and 2 mL EtOH) was added. The reaction vial is vortexed and incubated in a heating block at 42 °C with no shaking for 3 -4 h until all solvent is condensed under the lid. The tube is then vortexed and the mixture is applied onto a 10 x 10 cm HPTLC Silica 60 glass plate (VWR) using the automatic Camaq system. TLC plates were developed using $CHCl_3$/MeOH/H_2O/AcOH 65:25:4:1 for 6 cm and then cyclohexane/ethylacetate 1:1 for 9 cm. Lipids containing the fluorescent coumarin group were visualized using a geldoc system.

3.5.3. Lipidomics analysis of Sph and metabolites

HeLa cells were grown in 6 cm dishes (Nunc) to 85 – 95 % confluency and labelled with 2 µM Sph-Cou in imaging buffer or only in imaging buffer for 15 min. After washing with PBS, cells were transferred onto an ice block and UV-irradiated with > 400 nm light for 2 min and then immediately pelleted (by centrifugation with 3000 rpm for 1 min) and snap-frozen in liquid nitrogen. The pellets were resuspended in extraction solvent EtOH/H_2O/diethylether/pyridine (15:15:5:1) supplemented with ammonium hydroxide ($2.1 \cdot 10^{-3}$ N) and internal standards (C17-sphingosine, C17-sphinganine, C17-sphingosine-1-phosphate and C17-sphinganine-1-phosphate) were added. The pellets were vortexed at 4 °C for 10 min and incubated on ice for 20 min. Cell debris was pelleted by centrifugation at 20000 *g* for 2 min at 4 °C. The extraction was repeated one more time skipping the incubation on ice. Supernatants were combined and dried under vaccum in a Centrivap (Labconco, Kansas City, USA).

The lipid extract was resuspended in borate buffer and derivatized by reaction for 15 min at 55 °C with 6-aminoquinolyl-*N*-hydroxysuccinimidyl carbamate (AQC, 2.85mg/ml in acetonitrile) The AQC reagent was synthesized according to Cohen et al[225]. Samples were analyzed after overnight incubation at 24 °C using a reverse-phase C18 column (HPLC EC 100/2 Nucleoshell RP.18 2.7µm) on an Accela high-performance liquid chromatography system (ThermoFisher Scientific, Waltham, MA), coupled to a TSQ Vantage (ThermoFisher Scientific, Waltham, USA). MRM-MS was used to identify and quantify lipid species. The relative amounts of Sph and its metabolites were normalized to $^{15}N^{13}C$-valine, the internal standard for the derivatization process.

3.6. Proteomic screen

3.6.1. Cell labelling and crosslinking

HeLa cells were grown in three 10 cm dishes for each condition and labelled with 4 mL of 100 µM TFFA for 15 min, 100 µM TFDAG for 15 min and 6 µM TFS probe for 5 min. The cells were then UV-irradiated for 2.5 min at wavelengths above 400 nm follwed by a second irradiation at wavelenghts above 345 nm and washed with ice-cold PBS. The cells were scraped off in 2 mL PBS and centrifuged at 3000 rpm for 10 min at 4 °C. The cell pellet was resuspended in 300 µL PBS, 600 µL MeOH and 150 µL $CHCl_3$ were added, vortexed and centrifuged at 14 000 rpm for 3 min. The protein pellet was resuspended in 100 µL PBS and 100 µL lysis buffer were added, and shaken at 95 °C for 5 min. After cooling down, 2 µL benzonase was added and incubated for 30 min at 37 °C. Next, 100 µL of 200 mM DTT (in 200 mM HEPES) was added and incubated at 45 °C for 30 min and then 20 µL of 400 mM iodoacetamide (in 200 mM HEPES) was added and shaken at 24 °C for 30 min. Finally, 20 µL 200 mM DTT were added to quench the reaction. The proteins were precipitated by addition of 600 µL MeOH and 150 µL $CHCl_3$ and resuspended in 152.5 µL PBS/1 % (w/v) SDS/2x PIC by shaking at 37 °C for >1 h. 5 µL of the solution was removed for protein determination, the three lysates belonging to the same condition were pooled and stored at - 20 °C.

3.6.2. Protein determination using Amido Black

A serial dilution of BSA was prepared with 0, 2.5, 5, 7.5, 10, 25 and 50 µg BSA in 100 µL water. The samples were diluted to 100 µL. To all samples, 400 µL amido black solution was added, vortexed, incubated at room temperature for 5 min and centrifuged at 14 000 rpm for 5 min. The supernatant was aspirated and the pellets were washed twice with 500 µL MeOH/AcOH 10/1. The pellets were dissolved in 300 µL 0.1 N NaOH and 150 µL were spotted onto a 96 well plate. The absorbance at 550 nm was recorded on a Synergy 4 microplate reader (BioTek, Winooski, USA).

3.6.3. Biotinylation and pull-down

The volume of the lysate was adjusted to 1 mg of protein and diluted to 630 µL. 30 µL of each reagent for click reaction (2.5 mM TBTA in DMSO, 25 mM $CuSO_4$ in water, 25 mM biotin azide in water, 25 mM ascorbic acid in water) was added and the mixture was shaken at 37 °C for > 3 h. The proteins were precipitated twice using $CHCl_3$/MeOH (1/4), redissolved in 160 µL PBS/1 % SDS and diluted with 240 µL RPVS to reach a final SDS concentration of 0.4 % (w/v). After centrifugation at 1000 rpm for 3 min, the supernatant was transferred into a new vial and mixed with 10 µL NeutrAvidin agarose resin (Thermo Scientific), which were washed three times with 180 µL PBS/0.2 % SDS. The lysate was incubated with the resin for 1 h at room temperature and the supernatant was removed. The resin was washed 15 times with PBS/1 % SDS and the proteins were eluted with 50 µL elution buffer (100 mM Tris pH 6.8, 4 % SDS, 4 % βmercaptoethanol) at room temperature for 1 h. The supernatant was taken after heating to 95 °C for 30 min.

3.6.4. On-bead tryptic digest (adapted from Hughes et al.[210])

20 µL of hydrophilic and hydrophobic Sera-Mag Speed beads (Thermo Scientific) were mixed and kept in 100 µL water. The protein lysate was mixed with 5 µL fomic acid (5 % (v/v) in water) and 5 µL beads. Acetonitril was added immediately to a final concentration of greater than 50 %. The mixture was incubated 8 min at room temperature and was then placed on a magnetic rack for further 2 min. The supernatant was removed and discarded. The beads were washed twice with 200 µL EtOH (70 % (v/v) in water) and once with 180 µL acetonitrile. The dry beads were then reconstituted in 10 µL digestion solution (50 mM HEPES pH 8.0 + 1 µg trypsin/LysC (Promega, mass spec grade)) and incubated for 14 h at 37 °C. The peptides were recovered by adding 190 µL acetonitrile to the beads, incubating at room temperature for 8 min and for further 2 min on the magnetic rack. The supernatant was removed and discarded. The beads were washed with 180 µL acetonitrile and 200 µL EtOH (90 % (v/v) in water). Beads were reconstituted in 9 µL DMSO (4 % (v/v) in water) and sonicated for 5 min. The supernatant was removed and transferred to a deactivated glass vial containing 1 µL formic acid (10 % (v/v) in water).

3.6.5. High pH reverse phase offline fractionation (adapted from Bock et al.[226])

The peptide mixture was basified by addition of 10 µL 200 mM NH_4OH and 2 µL pure NH_4OH and injected into an Agilent 1200 Infinity high-performance liquid chromatography (HPLC) system equipped with a peltier-cooled autosampler and fraction collector (both set at 10 °C for all samples). The column was a Gemini C_{18} column (3 µm, 110 Å, 100 x 1.0 mm, Phenomenex) with a Gemini C_{18}, 4 x 2.0 mm SecurityGuard cartrigdge (Phenomenex) as a guard column. The solvent system consisted of two mobile phases: Phase A was 20 mM ammonium formate (pH 10.0) and phase B was acetonitrile (100 %). Sepearation was achieved at a flow rate of 0.1 mL/min using the following linear gradient: 100 % A for 2 min., from 100 % A to 35 % B in 59 min., 100 % A and reequilibration for 13 min. Thirty-two fractions were collected which were then pooled into 10 fractions and dried under vacuum centrifugation and reconstituted in 10 µL 0.1 % formic acid.

3.6.6. Peptide cleanup and enrichment

An Oasis HLB microelution plate (Waters) was washed twice with 200 µL 80 % acetonitrile/0.05 % formic acid and then equilibrated twice with 200 µL formic acid (0.05 % (v/v) in water) per well. The samples were loaded and the flowthrough was discarded. Samples were then washed twice with 200 µL formic acid (0.05 % (v/v) in water). Elution was achieved with 50 µL 80 % acetonitrile/0.05 % formic acid. The eluate was dried under vacuum centrifugation and reconstituted in DMSO (4 % (v/v) in water) + 1 % formic acid.

3.6.7. LC-MS/MS

Peptides were separated using the nanoAcquity UPLC system (Waters) fitted with a trapping (nanoAcquity Symmetry C18, 5 µm, 180 µm x 20 mm) and an analytical column (nanoAcquity BEH C18, 1.7 µm, 75 µm x 200 mm). The outlet of the analytical column was coupled directly to an LTQ Orbitrap Velos Pro (Thermo Fisher Scientific) using the Proxeon nanospray source. Solvent A was water, 0.1 % formic acid and solvent B was acetonitrile/0.1% formic acid. The samples (7 µL) were loaded with a constant flow of solvent A at 5 µL/min onto the trapping column. Trapping time was 6 minutes. Peptides were eluted via the analytical column a constant flow of 0.3 µL/min. During the elution step, the percentage of solvent B increased in a linear fashion from 3 % to 7 % in 10 min, then increased to 25 % in 20 min and finally to 40 % in a further 10 min. The peptides were introduced into the mass spectrometer via a Pico-Tip Emitter 360 µm OD x 20 µm ID; A 10 µm tip (New Objective) and a spray voltage of 2.2 kV were applied. The capillary temperature was set at 300 °C. Full scan MS spectra with mass range 300-1700 *m/z* were acquired in profile mode in the FT with resolution of 30 000. The filling time was set at maximum of 500 ms with limitation of 10^6 ions. The most intense ions (up to 15) from the full scan MS were selected for sequencing in the LTQ. Normalized collision energy of 40 % was used, and the fragmentation was performed after accumulation of 3 x 10^4 ions or after filling time of 100 ms for each precursor ion (whichever occurred first). MS/MS data were acquired in centroid mode. Only multiply charged (2+, 3+, 4+) precursor ions were selected for MS/MS. The dynamic exclusion list was restricted to 500 entries with a maximum retention period of 30 s and relative mass window of 10 ppm. In order to improve the mass accuracy, a lock mass correction using a background ion (*m/z* 445.12003) was applied.

3.6.8. Data analysis

Proteome Discoverer 1.4 (version 1.4.1.14, Thermo Scientific) was used as raw data post-processing interface with the possibility to select scan events for peptide/protein identification. Identification was performed using a species specific Uniprot database (Homo sapiens taxonomy, 2012, 86945 entries). Mascot (version 2.2.07, Matrix Sciences, London) was used as search engine. Variable amino acid modification was oxidized methionine. Carbamidomethylation of cysteines was set as fixed modification. Trypsin was selected as the enzyme, with one potential missed cleavage. Peptide and fragment ion tolerance was respectively 10 ppm and 0.5 Da. False Discovery Rates (FDR) of 5% (relaxed) and 1% (strict), validated based on q-value, were calculated by Proteome Discoverer based on the search against the corresponding randomized database. Results were filtered on upload for only high peptide confidence, peptide length greater than 6 amino acids and a minimum mascot peptide ion score of 20.

3.7. Visualization of protein-lipid complexes in cells

Cells were seeded onto 11 mm coverslips placed in wells of a 24-well plate and labeled with 4 µM pacSph in imaging buffer for 10 min. Cells were washed, overlaid with 1 mL imaging buffer and UV-irradiated on ice for 2.5 min at wavelength > 400 nm and for further 2.5 min at wavelengths of > 345 nm. Cells were immediately fixed with MeOH at -20°C for 20 min. Not crosslinked lipids were extracted by washing three times with 1 mL of $CHCl_3$/MeOH/AcOH 10:55:0.75 (v/v) at RT. Cells were then incubated with 50 µl of click mixture (1 mM ascorbic acid, 100 µM TBTA, 1 mM $CuSO_4$ and 2 µM Alexa 488 azide in PBS) for 1 h at RT in the dark. Cells were then washed with PBS and incubated with 50 µl of primary antibody (rabbit α-LAMP1, Cell Signaling, 1:100 or mouse α-GM130, abcam, 1:200 in PBS supplemented with 4 % BSA and 0.02 % Triton) overnight at 4°C. Coverslips were again washed in PBS and incubated with secondary antibody (α-rabbit conjugated to AlexaFluor555, α-mouse conjugated to AlexaFluor555Cell Signaling, 1:800) for 1 h, washed and mounted in DAPI-containing mounting medium (Vectashield, Vector Laboratories). Microscopy images were captured at room temperature using a confocal laser scanning microscope (Zeiss LSM780) with a 63x oil objective. Settings were as follows: DAPI-channel (405 nm excitation (ex), 409 - 475 nm emmission (em); green channel: 488 nm ex, 489 - 550 nm em; red channel: 561 nm ex, 569 - 655 nm em). Images were further processed using Fiji software (http://fiji.sc/Fiji).

3.8. Visualization of Sph via correlated light- and electron microscopy

NPC or wt cells were seeded on carbon coated Sapphire discs (3mm diameter, thickness 0.05 mm, Engineering Office M. Wohlwend GmbH, Sennwald, Switzerland) for 24 h. Uncaging and crosslinking was performed as described in chapter 3.7. Cells were then fixed in 4 % PFA in PHEM buffer for 10 min and permeabilized with 0.001 % Saponin in PHEM buffer for 5 min before click reaction for 1 h in the dark (see also chapter 3.7.). The samples were processed within 1 h for high-pressure freezing (HPF) using the HPM 010 (Bal-Tec), placed between two aluminium carriers and a gold slot grid spacer (Plano GmbH, Wetzlar, Germany).

The freeze substitution was performed in a temper temperature-controlling device (AFS2, Leica) in acetone supplemented with 0.1 % (w/v) uranyl acetate for 24 h at -90 °C. The temperature was raised to -45 °C within 10 h, held at that temperature, washed three times with acetone and infiltrated by Lowicryl HM20 (Polysciences Europe GmbH, Eppelheim, Germany) for 4 h periods at increasing concentrations (10 %, 25 %, 50 %, 75 %). The temperature was subsequently raised to -25 °C (5 °C/hour) and the final Lowicryl concentration of 100 % was held and washed every 10 h for three times. The blocks were finally polymerized by UV light incubation for 48 h at 20 °C.

Thick sections (300 nm) were cut using a Leica Utracut UCT microtome mounted with a diamond knife (Diatome, Biel, Switzerland). Each section was placed on a carbon-coated copper grid (Plano GmbH, Wetzlar, Germany), incubated for 8 min in a drop of 1:200 with 50 nm fluorescent microspheres in PBS (TetraSpecks, Lifetechnologies) followed by 3 times washing in water.

The grids were sandwiched between two coverslips (Menzel-Gläser, No. 1) filled with 30 µL water and sealed by vaccum grease. Samples were imaged using a Metamorph (Molecular Devices) operated widefield fluorescence microscope (Olympus IX81) equipped with an X-Cite 120PC light source (EXFO Life 2 Sciences), an Olympus PlanApo 100x 1.45 NA oil immersion objective, Orca-ER camera (Hamamatsu Photonics), electronic shutters and filter wheels (Sutter Instruments Co.). 470/22 nm and 556/20 nm excitation filters were used in combination with emission filters 520/35 nm for Tetraspecks and 624/40 nm for Alexa594.

The grids were incubated with gold fiducial markers (15 nm) and placed into a single-tilt holder on a Tecnai TF30 microscope (FEI) at 300 kV using Serial EM for electron tomography. Images were acquired at -60 to +60 ° (1 ° increment) recorded by a 4K Eagle camera (FEI) at a pixel size of 5.068 nm and reconstructed using IMOD (versions 4.1.4). Fluorescent and electron tomography images were correlated based on the fluorescent and gold fiducials using a MATLAB script[220].

Bibliography

1. Zechner, R., Kienesberger, P. C., Haemmerle, G., Zimmermann, R. & Lass, A. Adipose triglyceride lipase and the lipolytic catabolism of cellular fat stores. *J. Lipid Res.* **50,** 3–21 (2009).

2. Van Meer, G., Voelker, D. R. & Feigenson, G. W. Membrane lipids: where they are and how they behave. *Nat. Rev. Mol. Cell Biol.* **9,** 112–124 (2008).

3. Sud, M. *et al.* LMSD: LIPID MAPS structure database. *Nucleic Acids Res.* **35,** 527–532 (2007).

4. Wymann, M. P. & Schneiter, R. Lipid signalling in disease. *Nat. Rev. Mol. Cell Biol.* **9,** 162–176 (2008).

5. Ekroos, K. *et al.* Charting molecular composition of phosphatidylcholines by fatty acid scanning and ion trap MS3 fragmentation. *J. Lipid Res.* **44,** 2181–2192 (2003).

6. Ohvo-Rekilä, H., Ramstedt, B., Leppimäki, P. & Peter Slotte, J. Cholesterol interactions with phospholipids in membranes. *Prog. Lipid Res.* **41,** 66–97 (2002).

7. Hofmann, A. F. Bile Acids: The Good, the Bad, and the Ugly. *News Physiol Sci* **14,** 24–29 (1999).

8. Beato, M. Gene regulation by steroid hormones. *Cell* **56,** 335–344 (1989).

9. Wehling, M. Nongenomic actions of steroid hormones. *Trends Endocrinol. Metab.* **5,** 347–353 (1994).

10. Hanada, K. Serine palmitoyltransferase, a key enzyme of sphingolipid metabolism. *Biochim. Biophys. Acta - Mol. Cell Biol. Lipids* **1632,** 16–30 (2003).

11. Hannun, Y. A. & Obeid, L. M. Many ceramides. *J. Biol. Chem.* **286,** 27855–62 (2011).

12. Woodcock, J. Sphingosine and ceramide signalling in apoptosis. *IUBMB Life* **58,** 462–466 (2006).

13. Teichgräber, V. *et al.* Ceramide accumulation mediates inflammation, cell death and infection susceptibility in cystic fibrosis. *Nat. Med.* **14,** 382–391 (2008).

14. Sentelle, R. D. *et al.* Ceramide targets autophagosomes to mitochondria and induces lethal mitophagy. *Nat. Chem. Biol.* **8,** 831–838 (2012).

15. Gómez-Muñoz, A., Kong, J. Y., Salh, B. & Steinbrecher, U. P. Ceramide-1-phosphate blocks apoptosis through inhibition of acid sphingomyelinase in macrophages. *J. Lipid Res.* **45,** 99–105 (2004).

16. Granado, M. H. *et al.* Ceramide 1-phosphate (C1P) promotes cell migration. Involvement of a specific C1P receptor. *Cell. Signal.* **21,** 405–412 (2009).

17. Warnock, D. E. *et al.* Determination of plasma membrane lipid mass and composition in cultured Chinese hamster ovary cells using high gradient magnetic affinity chromatography. *J. Biol. Chem.* **268,** 10145–10153 (1993).

18. Ramstedt, B. & Slotte, J. P. Membrane properties of sphingomyelins. *FEBS Lett.* **531,** 33–37 (2002).

19. Lingwood, C. A. Glycosphingolipid functions. *Cold Spring Harb. Perspect. Biol.* **3,** 1–26 (2011).

20. Cox, T. M. Gaucher disease: clinical profile and therapeutic developments. *Biologics* **4,** 299–313 (2010).

21. Zarate, Y. A. & Hopkin, R. J. Fabry's disease. *Lancet* **372,** 1427–1435 (2008).

22. Futerman, A. H. & van Meer, G. The cell biology of lysosomal storage disorders. *Nat. Rev. Mol. Cell Biol.* **5,** 554–565 (2004).

23. Cuvillier, O. Sphingosine in apoptosis signaling. *Biochim. Biophys. Acta* **1585,** 153–62 (2002).

24. Suzuki, E., Handa, K., Toledo, M. S. & Hakomori, S. Sphingosine-dependent apoptosis: a unified concept based on multiple mechanisms operating in concert. *Proc. Natl. Acad. Sci. U. S. A.* **101,** 14788–93 (2004).

25. Vanier, M. T. Niemann-Pick disease type C. *Orphanet J. Rare Dis.* **5,** 16 (2010).

26. Spiegel, S. & Milstien, S. The outs and the ins of sphingosine-1-phosphate in immunity. *Nat. Rev. Immunol.* **11,** 403–415 (2011).

27. Pyne, N. J. & Pyne, S. Sphingosine 1-phosphate and cancer. *Nat. Rev. Cancer* **10,** 489–503 (2010).

28. Spiegel, S. & Milstien, S. Sphingosine-1-phosphate: an enigmatic signalling lipid. *Nat. Rev. Mol. Cell Biol.* **4,** 397–407 (2003).

29. Bandhuvula, P. & Saba, J. D. Sphingosine-1-phosphate lyase in immunity and cancer: silencing the siren. *Trends Mol. Med.* **13,** 210–217 (2007).

30. Hagen, N. *et al.* Subcellular origin of sphingosine 1-phosphate is essential for its toxic effect in lyase-deficient neurons. *J. Biol. Chem.* **284,** 11346–11353 (2009).

31. Hagen-Euteneuer, N., Lütjohann, D., Park, H., Merrill, A. H. & Van Echten-Deckert, G. Sphingosine 1-phosphate (S1P) lyase deficiency increases sphingolipid formation via recycling at the expense of de Novo biosynthesis in neurons. *J. Biol. Chem.* **287,** 9128–9136 (2012).

32. Bektas, M. *et al.* Sphingosine 1-phosphate lyase deficiency disrupts lipid homeostasis in liver. *J. Biol. Chem.* **285,** 10880–10889 (2010).

33. Levy, M. & Futerman, A. H. Mammalian ceramide synthases. *IUBMB Life* **62,** 347–356 (2010).

34. Hannun, Y. A. & Obeid, L. M. Principles of bioactive lipid signalling: lessons from sphingolipids. *Nat. Rev. Mol. Cell Biol.* **9,** 139–150 (2008).

35. Sandhoff, K. & Kolter, T. Biosynthesis and degradation of mammalian glycosphingolipids. *Philos. Trans. R. Soc. Lond. B. Biol. Sci.* **358,** 847–861 (2003).

36. Tafesse, F. G., Ternes, P. & Holthuis, J. C. M. The multigenic sphingomyelin synthase family. *J. Biol. Chem.* **281,** 29421–29425 (2006).

37. Hanada, K. *et al.* Molecular machinery for non-vesicular trafficking of ceramide. *Nature* **426,** 803–809 (2003).

38. Swanton, C. *et al.* Regulators of Mitotic Arrest and Ceramide Metabolism Are Determinants of Sensitivity to Paclitaxel and Other Chemotherapeutic Drugs. *Cancer Cell* **11,** 498–512 (2007).

39. Carstea, E. D. *et al.* Niemann-Pick C1 disease gene: homology to mediators of cholesterol homeostasis. *Science* **277,** 228–231 (1997).

40. Babalola, J. O. *et al.* Development of an assay for the intermembrane transfer of cholesterol by Niemann-Pick C2 protein. *Biol. Chem.* **388,** 617–626 (2007).

41. Scott, C. & Ioannou, Y. A. The NPC1 protein: Structure implies function. *Biochim. Biophys. Acta - Mol. Cell Biol. Lipids* **1685,** 8–13 (2004).

42. Miller, E. H. *et al.* Ebola virus entry requires the host-programmed recognition of an intracellular receptor. *EMBO J.* **31,** 1947–1960 (2012).

43. Millat, G., Marçais, C. & Tomasetto, C. Niemann-Pick C1 Disease: Correlations between NPC1 Mutations, Levels of NPC1 Protein, and Phenotypes Emphasize the Functional Significance of. *Am. J. …* 1373–1385 (2001).

44. Infante, R. E. *et al.* Purified NPC1 protein II. Localization of sterol binding to a 240-amino acid soluble luminal loop. *J. Biol. Chem.* **283,** 1064–1075 (2008).

45. Kwon, H. J. *et al.* Structure of N-Terminal Domain of NPC1 Reveals Distinct Subdomains for Binding and Transfer of Cholesterol. *Cell* **137,** 1213–1224 (2009).

46. Sokol, J. *et al.* Type C Niemann-Pick disease Lysosomal accumulation and defective intracellular mobilization of low density lipoprotein cholesterol. *J. Biol. Chem.* **263,** 3411–3417 (1988).

47. Malathi, K. *et al.* Mutagenesis of the putative sterol-sensing domain of yeast Niemann Pick C-related protein reveals a primordial role in subcellular sphingolipid distribution. *J. Cell Biol.* **164,** 547–556 (2004).

48. Puri, V. *et al.* Cholesterol modulates membrane traffic along the endocytic pathway in sphingolipid-storage diseases. *Nat. Cell Biol.* **1,** 386–388 (1999).

49. White, N. M., Corey, D. a. & Kelley, T. J. Mechanistic similarities between cultured cell models of cystic fibrosis and Niemann-pick type C. *Am. J. Respir. Cell Mol. Biol.* **31,** 538–543 (2004).

50. Trushina, E. *et al.* Mutant huntingtin inhibits clathrin-independent endocytosis and causes accumulation of cholesterol in vitro and in vivo. *Hum. Mol. Genet.* **15,** 3578–3591 (2006).

51. Patterson, M. C. *et al.* The effect of cholesterol-lowering agents on hepatic and plasma cholesterol in Niemann-Pick disease type C. *Neurology* **43,** 61–64 (1993).

52. Walter, M., Chen, F. W., Tamari, F., Wang, R. & Ioannou, Y. a. Endosomal lipid accumulation in NPC1 leads to inhibition of PKC, hypophosphorylation of vimentin and Rab9 entrapment. *Biol. cell* **101,** 141–152 (2009).

53. Liscum, L. *et al.* Identification of a pharmaceutical compound that partially corrects the Niemann-Pick C phenotype in cultured cells. *J. Lipid Res.* **43,** 1708–1717 (2002).

54. Te Vruchte, D. *et al.* Accumulation of glycosphingolipids in Niemann-Pick C disease disrupts endosomal transport. *J. Biol. Chem.* **279,** 26167–75 (2004).

55. Mukherjee, S. & Maxfield, F. R. Lipid and cholesterol trafficking in NPC. *Biochim. Biophys. Acta - Mol. Cell Biol. Lipids* **1685,** 28–37 (2004).

56. Lachmann, R. H. *et al.* Treatment with miglustat reverses the lipid-trafficking defect in Niemann-Pick disease type C. *Neurobiol. Dis.* **16,** 654–658 (2004).

57. Lloyd-Evans, E. *et al.* Niemann-Pick disease type C1 is a sphingosine storage disease that causes deregulation of lysosomal calcium. *Nat. Med.* **14,** 1247–55 (2008).

58. Berridge, M. J., Lipp, P. & Bootman, M. D. The versatility and universality of calcium signalling. *Nat. Rev. Mol. Cell Biol.* **1,** 11–21 (2000).

59. Nilius, B., Owsianik, G., Voets, T. & Peters, J. A. Transient receptor potential cation channels in disease. *Physiol. Rev.* **87,** 165–217 (2007).

60. Burdakov, D., Petersen, O. H. & Verkhratsky, A. Intraluminal calcium as a primary regulator of endoplasmic reticulum function. *Cell Calcium* **38,** 303–310 (2005).

61. Haller, T., Dietl, P., Deetjen, P. & Völkl, H. The lysosomal compartment as intracellular calcium store in MDCK cells: a possible involvement in InsP3-mediated Ca2+ release. *Cell Calcium* **19,** 157–165 (1996).

62. Christensen, K. A., Myers, J. T. & Swanson, J. A. pH-dependent regulation of lysosomal calcium in macrophages. *J. Cell Sci.* **115,** 599–607 (2002).

63. Feng, X. *et al.* Drosophila TRPML forms PI(3,5)P2-activated cation channels in both endolysosomes and plasma Membrane. *J. Biol. Chem.* **289,** 4262–4272 (2014).

64. Peiter, E. *et al.* The vacuolar Ca2+-activated channel TPC regulates germination and stomatal movement. *Nature* **434,** 404–408 (2005).

65. Brailoiu, E. *et al.* An NAADP-gated two-pore channel targeted to the plasma membrane uncouples triggering from amplifying Ca2+ signals. *J. Biol. Chem.* **285,** 38511–38516 (2010).

66. Pitt, S. J. *et al.* TPC2 is a novel NAADP-sensitive Ca2+ release channel, operating as a dual sensor of luminal pH and Ca2+. *J. Biol. Chem.* **285,** 35039–35046 (2010).

67. Schieder, M., Rötzer, K., Brüggemann, A., Biel, M. & Wahl-Schott, C. a. Characterization of two-pore channel 2 (TPCN2)-mediated Ca2+ currents in isolated lysosomes. *J. Biol. Chem.* **285,** 21219–21222 (2010).

68. Wang, X. *et al.* TPC proteins are phosphoinositide- activated sodium-selective ion channels in endosomes and lysosomes. *Cell* **151,** 372–83 (2012).

69. Cang, C. *et al.* mTOR regulates lysosomal ATP-sensitive two-pore Na(+) channels to adapt to metabolic state. *Cell* **152,** 778–90 (2013).

70. Ruas, M. *et al.* Expression of Ca2+-permeable two-pore channels rescues NAADP signalling in TPC-deficient cells. *EMBO J.* 1–16 (2015).

71. Morgan, A. J. & Galione, A. Two-pore channels (TPCs): current controversies. *Bioessays* **36,** 173–83 (2014).

72. Jha, A., Ahuja, M., Patel, S., Brailoiu, E. & Muallem, S. Convergent regulation of the lysosomal two-pore channel-2 by Mg2+, NAADP, PI(3,5)P2 and multiple protein kinases. *EMBO J.* **33,** 501–511 (2014).

73. Jentsch, T. J., Hoegg-beiler, M. B. & Vogt, J. Departure gate of acidic Ca 2 + confirmed. *EMBO J.* **2,** 1–3 (2015).

74. Holroyd, C., Kistner, U., Annaert, W. & Jahn, R. Fusion of endosomes involved in synaptic vesicle recycling. *Mol. Biol. Cell* **10,** 3035–3044 (1999).

75. Bargal, R. *et al.* Identification of the gene causing mucolipidosis type IV. *Nat. Genet.* **26,** 118–123 (2000).

76. Hu, Z. *et al.* Mutations in ATP2C1, encoding a calcium pump, cause Hailey-Hailey disease. *Nat. Genet.* **24,** 61–65 (2000).

77. Sancak, Y. *et al.* Ragulator-rag complex targets mTORC1 to the lysosomal surface and is necessary for its activation by amino acids. *Cell* **141,** 290–303 (2010).

78. Zoncu, R. *et al.* mTORC1 Senses Lysosomal Amino Acids through an Inside-out Mechanism that Requires the Vacuolar H+-ATPase. *Science (80-.).* **334,** 678–683 (2011).

79. Settembre, C. *et al.* TFEB links autophagy to lysosomal biogenesis. *Science* **332,** 1429–1433 (2011).

80. Sardiello, M. *et al.* A gene network regulating lysosomal biogenesis and function. *Science* **325,** 473–477 (2009).

81. Medina, D. L. *et al.* Transcriptional activation of lysosomal exocytosis promotes cellular clearance. *Dev. Cell* **21,** 421–430 (2011).

82. Medina, D. L. *et al.* Lysosomal calcium signalling regulates autophagy through calcineurin and TFEB. *Nat. Cell Biol.* **17,** 288–299 (2015).

83. Spampanato, C. *et al.* Transcription factor EB (TFEB) is a new therapeutic target for Pompe disease. *EMBO Mol. Med.* **5,** 691–706 (2013).

84. Decressac, M. *et al.* TFEB-mediated autophagy rescues midbrain dopamine neurons from α-synuclein toxicity. *Proc. Natl. Acad. Sci. U. S. A.* **110,** E1817–26 (2013).

85. Polito, V. a *et al.* Selective clearance of aberrant tau proteins and rescue of neurotoxicity by transcription factor EB. *EMBO Mol. Med.* **6,** 1–19 (2014).

86. Tsunemi, T. *et al.* PGC-1 Rescues Huntington's Disease Proteotoxicity by Preventing Oxidative Stress and Promoting TFEB Function. *Sci. Transl. Med.* **4,** 142ra97–142ra97 (2012).

87. Feldmann, H. & Geisbert, T. W. Ebola haemorrhagic fever. *Lancet* **377,** 849–862 (2011).

88. World Health Organization. Ebola data and statistics. *Situat. Summ.* (2015). at <http://apps.who.int/gho/data/view.ebola-sitrep.ebola-summary-latest?lang=en>

89. Martínez-Romero, C. & García-Sastre, A. Against the clock towards new Ebola virus therapies. *Virus Res.* (2015). doi:10.1016/j.virusres.2015.05.025

90. Lee, J. E. & Saphire, E. O. Ebolavirus glycoprotein structure and mechanism of entry. *Future Virol.* **4,** 621–635 (2009).

91. Nanbo, A. *et al.* Ebolavirus is internalized into host cells via macropinocytosis in a viral glycoprotein-dependent manner. *PLoS Pathog.* **6,** (2010).

92. Mulherkar, N., Raaben, M., de la Torre, J. C., Whelan, S. P. & Chandran, K. The Ebola virus glycoprotein mediates entry via a non-classical dynamin-dependent macropinocytic pathway. *Virology* **419,** 72–83 (2011).

93. Chandran, K., Sullivan, N. J., Felbor, U., Whelan, S. P. & Cunningham, J. M. Endosomal proteolysis of the Ebola virus glycoprotein is necessary for infection. *Science* **308,** 1643–1645 (2005).

94. Hood, C. L. *et al.* Biochemical and structural characterization of cathepsin L-processed Ebola virus glycoprotein: implications for viral entry and immunogenicity. *J. Virol.* **84,** 2972–2982 (2010).

95. Brecher, M. *et al.* Cathepsin Cleavage Potentiates the Ebola Virus Glycoprotein To Undergo a Subsequent Fusion-Relevant Conformational Change. *J. Virol.* **86,** 364–372 (2012).

96. Falzarano, D. & Feldmann, H. Delineating Ebola entry. *Science (80-.).* **347,** 947–948 (2015).

97. Carette, J. E. *et al.* Ebola virus entry requires the cholesterol transporter Niemann-Pick C1. *Nature* **477,** 340–343 (2011).

98. Côté, M. *et al.* Small molecule inhibitors reveal Niemann-Pick C1 is essential for Ebola virus infection. *Nature* **477,** 344–348 (2011).

99. Herbert, A. S. *et al.* Niemann-Pick C1 Is Essential for Ebolavirus Replication and Pathogenesis In Vivo. *MBio* **6,** 1–12 (2015).

100. Kolokoltsov, A. A., Saeed, M. F., Freiberg, A. N., Holbrook, M. R. & Davey, R. A. Identification of novel cellular targets for therapeutic intervention against Ebola virus infection by siRNA screening. *Drug Dev. Res.* **70,** 255–265 (1009).

101. Sakurai, Y. *et al.* Two-pore channels control Ebola virus host cell entry and are drug targets for disease treatment. *Science (80-.).* **347,** 995–998 (2015).

102. Carrasco, S. & Mérida, I. Diacylglycerol, when simplicity becomes complex. *Trends Biochem. Sci.* **32,** 27–36 (2007).

103. Wang, X., Devaiah, S. P., Zhang, W. & Welti, R. Signaling functions of phosphatidic acid. *Prog. Lipid Res.* **45,** 250–278 (2006).

104. Delmas, P., Coste, B., Gamper, N. & Shapiro, M. S. Phosphoinositide lipid second messengers: New paradigms for calcium channel modulation. *Neuron* **47,** 179–182 (2005).

105. Alvarez, S. E., Milstien, S. & Spiegel, S. Autocrine and paracrine roles of sphingosine-1-phosphate. *Trends Endocrinol. Metab.* **18,** 300–7 (2007).

106. Young, M. M., Kester, M. & Wang, H.-G. Sphingolipids: regulators of crosstalk between apoptosis and autophagy. *J. Lipid Res.* **54,** 5–19 (2013).

107. Eyster, K. The membrane and lipids as integral participants in signal transduction: lipid signal transduction for the non-lipid biochemist. *Adv. Physiol. Educ.* **31,** 5–16 (2007).

108. Nishioka, T. *et al.* Rapid Turnover Rate of Phosphoinositides at the Front of Migrating MDCK Cells. **19,** 4213–4223 (2008).

109. Axe, E. L. *et al.* Autophagosome formation from membrane compartments enriched in phosphatidylinositol 3-phosphate and dynamically connected to the endoplasmic reticulum. *J. Cell Biol.* **182,** 685–701 (2008).

110. Quinn, K. V, Behe, P. & Tinker, A. Monitoring changes in membrane phosphatidylinositol 4,5-bisphosphate in living cells using a domain from the transcription factor tubby. *J. Physiol.* **586,** 2855–2871 (2008).

111. Brombacher, E. *et al.* Rab1 guanine nucleotide exchange factor SidM is a major phosphatidylinositol 4-phosphate-binding effector protein of Legionella pneumophila. *J. Biol. Chem.* **284,** 4846–4856 (2009).

112. Varnai, P., Thyagarajan, B., Rohacs, T. & Balla, T. Rapidly inducible changes in phosphatidylinositol 4,5-bisphosphate levels influence multiple regulatory functions of the lipid in intact living cells. *J. Cell Biol.* **175,** 377–382 (2006).

113. Oatey, P. B. *et al.* Confocal imaging of the subcellular distribution of phosphatidylinositol 3,4,5-trisphosphate in insulin- and PDGF-stimulated 3T3-L1 adipocytes. *Biochem. J.* **344 Pt 2,** 511–518 (1999).

114. Martelli, A. M. *et al.* Intranuclear 3′-phosphoinositide metabolism and Akt signaling: New mechanisms for tumorigenesis and protection against apoptosis? *Cell. Signal.* **18,** 1101–1107 (2006).

115. Van Meer, G. & Liskamp, R. M. J. Brilliant lipids. *Nat. Methods* **2,** 14–15 (2005).

116. Fili, N., Calleja, V., Woscholski, R., Parker, P. J. & Larijani, B. Compartmental signal modulation: Endosomal phosphatidylinositol 3-phosphate controls endosome morphology and selective cargo sorting. *Proc. Natl. Acad. Sci. U. S. A.* **103,** 15473–15478 (2006).

117. Zoncu, R. *et al.* A Phosphoinositide Switch Controls the Maturation and Signaling Properties of APPL Endosomes. *Cell* **136,** 1110–1121 (2009).

118. Ueno, T., Falkenburger, B. H., Pohlmeyer, C. & Inoue, T. Triggering Actin Comets Versus Membrane Ruffles: Distinctive Effects of Phosphoinositides on Actin Reorganization. *Sci. Signal.* **4,** ra87–ra87 (2011).

119. Suh, B.-C., Inoue, T., Meyer, T. & Hille, B. Rapid chemically induced changes of PtdIns(4,5)P2 gate KCNQ ion channels. *Science* **314,** 1454–1457 (2006).

120. Zoncu, R., Efeyan, A. & Sabatini, D. M. mTOR: from growth signal integration to cancer, diabetes and ageing. *Nat. Rev. Mol. Cell Biol.* **12,** 21–35 (2011).

121. Inoue, T., Heo, W. Do, Grimley, J. S., Wandless, T. J. & Meyer, T. An inducible translocation strategy to rapidly activate and inhibit small GTPase signaling pathways. *Nat. Methods* **2,** 415–418 (2005).

122. Xu, T., Johnson, C. a, Gestwicki, J. E. & Kumar, A. Conditionally controlling nuclear trafficking in yeast by chemical-induced protein dimerization. *Nat. Protoc.* **5,** 1831–1843 (2010).

123. Kennedy, M., Hughes, R. & Peteya, L. Rapid blue-light-mediated induction of protein interactions in living cells. *Nat. Methods* **7,** 973–975 (2010).

124. Feng, S. *et al.* A rapidly reversible chemical dimerizer system to study lipid signaling in living cells. *Angew. Chemie - Int. Ed.* **53,** 6720–6723 (2014).

125. Baron, C. L. & Malhotra, V. Role of diacylglycerol in PKD recruitment to the TGN and protein transport to the plasma membrane. *Science* **295,** 325–328 (2002).

126. Kagan, J. C. & Medzhitov, R. Phosphoinositide-Mediated Adaptor Recruitment Controls Toll-like Receptor Signaling. *Cell* **125,** 943–955 (2006).

127. Lee, M. *et al.* Sphingosine-1-phosphate as a ligand for the G-protein-coupled receptor EDG-1. *Science (80-.).* **279,** 1552–1555 (1998).

128. Pasternack, S. M. *et al.* G protein-coupled receptor P2Y5 and its ligand LPA are involved in maintenance of human hair growth. *Nat. Genet.* **40,** 329–334 (2008).

129. Manifava, M. *et al.* Differential Binding of Traffic-related Proteins to Phosphatidic Acid- or Phosphatidylinositol (4,5)-Bisphosphate-coupled Affinity Reagents. *J. Biol. Chem.* **276,** 8987–8994 (2001).

130. Gallego, O. *et al.* A systematic screen for protein-lipid interactions in Saccharomyces cerevisiae. *Mol. Syst. Biol.* **6,** 430 (2010).

131. Saliba, A.-E. *et al.* A quantitative liposome microarray to systematically characterize protein-lipid interactions. *Nat. Methods* **11,** 47–50 (2014).

132. Maeda, K. *et al.* Interactome map uncovers phosphatidylserine transport by oxysterol-binding proteins. *Nature* **501,** 257–61 (2013).

133. Contreras, F.-X. *et al.* Molecular recognition of a single sphingolipid species by a protein's transmembrane domain. *Nature* **481,** 525–529 (2012).

134. Höglinger, D., Nadler, A. & Schultz, C. Caged lipids as tools for investigating cellular signaling. *Biochim. Biophys. Acta* **1841,** 1085–96 (2014).

135. Il'ichev, Y. V., Schwörer, M. a. & Wirz, J. Photochemical Reaction Mechanisms of 2-Nitrobenzyl Compounds: Methyl Ethers and Caged ATP. *J. Am. Chem. Soc.* **126,** 4581–4595 (2004).

136. Schade, B. *et al.* Deactivation Behavior and Excited-State Properties of (Coumarin-4-yl)methyl Derivatives. 1. Photocleavage of (7-Methoxycoumarin-4-yl)methyl-Caged Acids with Fluorescence Enhancement. *J. Org. Chem.* **64,** 9109–9117 (1999).

137. Qiao, L., Kozikowski, A. P., Olivera, A. & Spiegel, S. Synthesis and evaluation of a photolyzable derivative of sphingosine 1-phosphate--caged SPP. *Bioorg. Med. Chem. Lett.* **8,** 711–714 (1998).

138. Meyer zu Heringdorf, D. *et al.* Photolysis of intracellular caged sphingosine-1-phosphate causes Ca2+ mobilization independently of G-protein-coupled receptors. *FEBS Lett.* **554,** 443–449 (2003).

139. Hopson, K. P., Truelove, J., Chun, J., Wang, Y. & Waeber, C. S1P activates store-operated calcium entry via receptor- and non-receptor-mediated pathways in vascular smooth muscle cells. *Am. J. Physiol. Cell Physiol.* **300,** C919–C9126 (2011).

140. Usatyuk, P. V *et al.* Photolysis of caged sphingosine-1-phosphate induces barrier enhancement and intracellular activation of lung endothelial cell signaling pathways. *Am. J. Physiol. Lung Cell. Mol. Physiol.* **300,** L840–L850 (2011).

141. Chakrabarti, P. & Khorana, G. A new approach to the study of phospholipid-protein interactions in biological membranes. Synthesis of fatty acids and phospholipids containing photosensitive groups. *Biochemistry* **14,** 5021–5033 (1975).

142. Gupta, C. M. *et al.* Intermolecular crosslinking of fatty acyl chains in phospholipids: use of photoactivable carbene precursors. *Proc. Natl. Acad. Sci. U. S. A.* **76,** 2595–2599 (1979).

143. Suchanek, M., Radzikowska, A. & Thiele, C. Photo-leucine and photo-methionine allow identification of protein-protein interactions in living cells. *Nat. Methods* **2,** 261–267 (2005).

144. Thiele, C., Hannah, M. J., Fahrenholz, F. & Huttner, W. B. Cholesterol binds to synaptophysin and is required for biogenesis of synaptic vesicles. *Nat. Cell Biol.* **2,** 42–49 (2000).

145. Haberkant, P. *et al.* Protein-sphingolipid interactions within cellular membranes. *J. Lipid Res.* **49,** 251–262 (2008).

146. Kolb, H. C., Finn, M. G. & Sharpless, K. B. Click Chemistry : Diverse Chemical Function from a Few Good Reactions. *Angew. Chemie - Int. Ed.* **40,** 2004–2021 (2001).

147. Tornøe, C. W., Christensen, C. & Meldal, M. Peptidotriazoles on solid phase: [1,2,3]-Triazoles by regiospecific copper(I)-catalyzed 1,3-dipolar cycloadditions of terminal alkynes to azides. *J. Org. Chem.* **67,** 3057–3064 (2002).

148. Tanaka, K. A. K. *et al.* Membrane molecules mobile even after chemical fixation. *Nat. Methods* **7,** 865–866 (2010).

149. Gubbens, J. *et al.* Photocrosslinking and Click Chemistry Enable the Specific Detection of Proteins Interacting with Phospholipids at the Membrane Interface. *Chem. Biol.* **16,** 3–14 (2009).

150. Hulce, J. J., Cognetta, A. B., Niphakis, M. J., Tully, S. E. & Cravatt, B. F. Proteome-wide mapping of cholesterol-interacting proteins in mammalian cells. *Nat. Methods* **10,** 259–64 (2013).

151. Haberkant, P. *et al.* In vivo profiling and visualization of cellular protein-lipid interactions using bifunctional fatty acids. *Angew. Chem. Int. Ed. Engl.* **52,** 4033–8 (2013).

152. Niphakis, M. J. *et al.* A Global Map of Lipid-Binding Proteins and Their Ligandability in Cells. *Cell* **161,** 1668–1680 (2015).

153. Canals, D., Perry, D. M., Jenkins, R. W. & Hannun, Y. A. Drug targeting of sphingolipid metabolism: Sphingomyelinases and ceramidases. *Br. J. Pharmacol.* **163,** 694–712 (2011).

154. Mayer, G. & Heckel, A. Biologically active molecules with a 'light switch'. *Angew. Chem. Int. Ed. Engl.* **45,** 4900–4921 (2006).

155. Zehavi, U. Synthesis of potentially caged sphingolipids, possible precursors of cellular modulators and second messengers. *Chem. Phys. Lipids* **90,** 55–61 (1997).

156. Scott, R. H., Pollock, J., Ayar, A., Thatcher, N. M. & Zehavi, U. Synthesis and use of caged sphingolipids. *Methods Enzymol.* **312,** 387–400 (2000).

157. Givens, R., Rubina, M. & Wirz, J. Applications of p-hydroxyphenacyl (pHP) and coumarin-4-ylmethyl photoremovable protecting groups. *Photochem. Photobiol. Sci.* **11,** 472–488 (2012).

158. Hagen, V. *et al.* [7-(Dialkylamino)coumarin-4-yl]methyl-caged compounds as ultrafast and effective long-wavelength phototriggers of 8-bromo-substituted cyclic nucleotides. *ChemBioChem* **4,** 434–442 (2003).

159. Thiele, C. *et al.* Tracing fatty acid metabolism by click chemistry. *ACS Chem. Biol.* **7,** 2004–11 (2012).

160. Guan, X. L., Riezman, I., Wenk, M. R. & Riezman, H. *Yeast lipid analysis and quantification by mass spectrometry*. *Methods Enzymol.* **470,** (Elsevier Inc., 2010).

161. Lester, R. L. & Dickson, R. C. High-performance liquid chromatography analysis of molecular species of sphingolipid-related long chain bases and long chain base phosphates in Saccharomyces cerevisiae after derivatization with 6-aminoquinolyl-N-hydroxysuccinimidyl carbamate. *Anal. Biochem.* **298,** 283–292 (2001).

162. Clapham, D. E. Calcium signaling. *Cell* **131,** 1047–58 (2007).

163. Rudolf, R., Mongillo, M., Rizzuto, R. & Pozzan, T. Looking forward to seeing calcium. *Nat. Rev. Mol. Cell Biol.* **4,** 579–586 (2003).

164. Paredes, R. M., Etzler, J. C., Watts, L. T., Zheng, W. & Lechleiter, J. D. Chemical calcium indicators. *Methods* **46,** 143–151 (2008).

165. Gee, K. R. *et al.* Chemical and physiological characterization of fluo-4 Ca(2+)-indicator dyes. *Cell Calcium* **27,** 97–106 (2000).

166. Stein, F., Kress, M., Reither, S., Piljic, A. & Schultz, C. FluoQ : A Tool for Rapid Analysis of Multiparameter Fluorescence Imaging Data Applied to Oscillatory Events. *ACS Chem. Biol.* 1862–1868 (2013). doi:10.1021/cb4003442

167. R Development Core Team. R: A Language and Environment for Statistical Computing. (2014).

168. Rosen, H., Gonzalez-Cabrera, P. J., Sanna, M. G. & Brown, S. Sphingosine 1-phosphate receptor signaling. *Annu. Rev. Biochem.* **78,** 743–68 (2009).

169. Lee, M. *et al.* Sphingosine-1-Phosphate as a Ligand for the G Protein-Coupled Receptor EDG-1. *Science (80-.).* **279,** 1552–1555 (1998).

170. Yatomi, Y. *et al.* N,N-Dimethylsphingosine Inhibition of Sphingosine Kinase and Sphingosine 1-Phosphate Activity in Human Platelets. *Biochemistry* **35,** 626–633 (1996).

171. Edsall, L. C., Brocklyn, J. R. Van, Cuvillier, O., Kleuser, B. & Spiegel, S. N, N-dimethylsphingosine is a potent competitive inhibitor of sphingosine kinas but not protein kinase C: Modulation of cellular levels of sphingosine 1-phosphate and ceramide. *Biochemistry* **37,** 12892–12898 (1998).

172. French, K. J. *et al.* Pharmacology and antitumor activity of ABC294640, a selective inhibitor of sphingosine kinase-2. *J. Pharmacol. Exp. Ther.* **333,** 129–139 (2010).

173. Igarashi, Y. *et al.* Effect of Chemically Well-Defined Sphingosine and Its N-Methyl Derivatives on Protein Kinase C and src Kinase Activities. *Biochemistry* **28,** 6796–6800 (1989).

174. Hannun, Y. A., Loomis, C. R., Merrill, A. H. & Bell, R. M. Sphingosine inhibition of protein kinase C activity and of phorbol dibutyrate binding in vitro and in human platelets. *J. Biol. Chem.* **261,** 12604–12609 (1986).

175. Gräler, M. H. & Goetzl, E. J. The immunosuppressant FTY720 down-regulates sphingosine 1-phosphate G-protein-coupled receptors. *FASEB J.* **18,** 551–553 (2004).

176. Tonelli, F. *et al.* FTY720 and (S)-FTY720 vinylphosphonate inhibit sphingosine kinase 1 and promote its proteasomal degradation in human pulmonary artery smooth muscle, breast cancer and androgen-independent prostate cancer cells. *Cell. Signal.* **22,** 1536–42 (2010).

177. Lim, K. G. *et al.* Inhibition kinetics and regulation of sphingosine kinase 1 expression in prostate cancer cells: Functional differences between sphingosine kinase 1a and 1b. *Int. J. Biochem. Cell Biol.* **44,** 1457–1464 (2012).

178. Gafni, J. *et al.* Xestospongins: Potent Membrane Permeable Blockers of the Inositol 1,4,5-Trisphosphate Receptor. *Neuron* **19,** 723–733 (1997).

179. Berg, T. O., Strømhaug, E., Løvdal, T., Seglen, O. & Berg, T. Use of glycyl-L-phenylalanine 2-naphthylamide, a lysosome-disrupting cathepsin C substrate, to distinguish between lysosomes and prelysosomal endocytic vacuoles. *Biochem. J.* **300 (Pt 1,** 229–236 (1994).

180. Brailoiu, E. *et al.* Essential requirement for two-pore channel 1 in NAADP-mediated calcium signaling. *J. Cell Biol.* **186,** 201–9 (2009).

181. Calcraft, P. J. *et al.* NAADP mobilizes calcium from acidic organelles through two-pore channels. *Nature* **459,** 596–600 (2009).

182. Dong, X. *et al.* PI(3,5)P(2) controls membrane trafficking by direct activation of mucolipin Ca(2+) release channels in the endolysosome. *Nat. Commun.* **1,** 38 (2010).

183. Ruas, M. *et al.* TPC1 has two variant isoforms, and their removal has different effects on endo-lysosomal functions compared to loss of TPC2. *Mol. Cell. Biol.* **34,** 3981–92 (2014).

184. Durlu-Kandilci, N. T. *et al.* TPC2 proteins mediate Nicotinic Acid Adenine Dinucleotide Phosphate (NAADP)- and agonist-evoked contractions of smooth muscle. *J. Biol. Chem.* **285,** 24925–24932 (2010).

185. Naylor, E. *et al.* Identification of a chemical probe for NAADP by virtual screening. *Nat. Chem. Biol.* **5,** 220–6 (2009).

186. Pitt, S. J., Lam, A. K. M., Rietdorf, K., Galione, A. & Sitsapesan, R. Reconstituted human TPC1 is a proton-permeable ion channel and is activated by NAADP or Ca2+. *Sci. Signal.* **7,** 1–11 (2014).

187. Settembre, C. & Ballabio, A. Lysosome: regulator of lipid degradation pathways. *Trends Cell Biol.* **24,** 743–750 (2014).

188. Zhao, Y. *et al.* An Expanded Palette of Genetically Encoded Ca2+ Indicators. *Science (80-.).* **333,** 1888–1891 (2011).

189. Ellis-Davies, G. C. & Kaplan, J. H. Nitrophenyl-EGTA, a photolabile chelator that selectively binds Ca2+ with high affinity and releases it rapidly upon photolysis. *Proc. Natl. Acad. Sci. U. S. A.* **91,** 187–191 (1994).

190. Coxey, R. a, Pentchev, P. G., Campbell, G. & Blanchette-Mackie, E. J. Differential accumulation of cholesterol in Golgi compartments of normal and Niemann-Pick type C fibroblasts incubated with LDL: a cytochemical freeze-fracture study. *J. Lipid Res.* **34,** 1165–1176 (1993).

191. Kobayashi, T. *et al.* Late endosomal membranes rich in lysobisphosphatidic acid regulate cholesterol transport. *Nat. Cell Biol.* **1,** 113–118 (1999).

192. Zhang, M. *et al.* Sterol-modulated Glycolipid Sorting Occurs in Niemann-Pick C1 Late Endosomes. *J. Biol. Chem.* **276,** 3417–3425 (2001).

193. Xu, M. *et al.* δ-tocopherol reduces lipid accumulation in Niemann-Pick type C1 and Wolman cholesterol storage disorders. *J. Biol. Chem.* **287,** 39349–39360 (2012).

194. Mattie, M., Brooker, G. & Spiegel, S. Sphingosine-1-phosphate, a putative second messenger, mobilizes calcium from internal stores via an inositol trisphosphate-independent pathway. *J. Biol. Chem.* **269,** 3181–3188 (1994).

195. Rybalchenko, V. *et al.* Membrane potential regulates Nicotinic Acid Adenine Dinucleotide Phosphate (NAADP) dependence of the pH- and Ca2+-sensitive organellar two-pore channel TPC1. *J. Biol. Chem.* **287,** 20407–20416 (2012).

196. Ruas, M. *et al.* Purified TPC isoforms form NAADP receptors with distinct roles for Ca(2+) signaling and endolysosomal trafficking. *Curr. Biol.* **20,** 703–9 (2010).

197. Parkesh, R. *et al.* Cell-permeant NAADP: A novel chemical tool enabling the study of Ca2+ signalling in intact cells. *Cell Calcium* **43,** 531–538 (2008).

198. Patel, S. & Docampo, R. Acidic calcium stores open for business: expanding the potential for intracellular Ca2+ signaling. *Trends Cell Biol.* **20,** 277–86 (2010).

199. Pacheco, C. D., Kunkel, R. & Lieberman, A. P. Autophagy in Niemann-Pick C disease is dependent upon Beclin-1 and responsive to lipid trafficking defects. *Hum. Mol. Genet.* **16,** 1495–1503 (2007).

200. Elrick, M. J., Yu, T., Chung, C. & Lieberman, A. P. Impaired proteolysis underlies autophagic dysfunction in Niemann-Pick type C disease. *Hum. Mol. Genet.* **21,** 4876–4887 (2012).

201. Bartke, N. & Hannun, Y. A. Bioactive sphingolipids: metabolism and function. *J. Lipid Res.* **50 Suppl,** S91–6 (2009).

202. Morad, S. a F. & Cabot, M. C. Ceramide-orchestrated signalling in cancer cells. *Nat. Rev. Cancer* **13,** 51–65 (2013).

203. Hla, T. & Dannenberg, A. J. Sphingolipid signaling in metabolic disorders. *Cell Metab.* **16,** 420–434 (2012).

204. Summers, S. a. & Nelson, D. H. A Role for Sphingolipids in Producing the Common Features of Type 2 Diabetes, Metabolic Syndrome X, and Cushing's Syndrome. *Diabetes* **54,** 591–602 (2005).

205. Sloan, C. D. K., Marty, M. T., Sligar, S. G. & Bailey, R. C. Interfacing lipid bilayer nanodiscs and silicon photonic sensor arrays for multiplexed protein-lipid and protein-membrane protein interaction screening. *Anal. Chem.* **85,** 2970–2976 (2013).

206. Haberkant, P. & Holthuis, J. C. M. Fat & fabulous: Bifunctional lipids in the spotlight. *Biochim. Biophys. Acta* (2014). doi:10.1016/j.bbalip.2014.01.003

207. Shieh, P., Hangauer, M. J. & Bertozzi, C. R. Fluorogenic Azidofluoresceins for Biological Imaging. *J. Am. Chem. Soc.* **134,** 17428–17431 (2012).

208. Rivolta, I. *et al.* Cellular uptake of coumarin-6 as a model drug loaded in solid lipid nanoparticles. *J. Physiol. Pharmacol.* **62,** 45–53 (2011).

209. Haberkant, P. *et al.* Bifunctional Sphingosine for Cell-Based Analysis of Protein-Sphingolipid Interactions. *In preparation* (2015).

210. Hughes, C. S. *et al.* Ultrasensitive proteome analysis using paramagnetic bead technology. *Mol. Syst. Biol.* **10,** 1–14 (2014).

211. Smedley, D. *et al.* The BioMart community portal: an innovative alternative to large, centralized data repositories. *Nucleic Acids Res.* 1–10 (2015). doi:10.1093/nar/gkv350

212. Hoetelmans, R. W. *et al.* Effects of acetone, methanol, or paraformaldehyde on cellular structure, visualized by reflection contrast microscopy and transmission and scanning electron microscopy. *Appl. Immunohistochem. Mol. Morphol.* **9,** 346–351 (2001).

213. Karten, B., Vance, D. E., Campenot, R. B. & Vance, J. E. Trafficking of cholesterol from cell bodies to distal axons in Niemann Pick C1-deficient neurons. *J. Biol. Chem.* **278,** 4168–4175 (2003).

214. Millard, E. E., Srivastava, K., Traub, L. M., Schaffer, J. E. & Ory, D. S. Niemann-Pick type C1 (NPC1) overexpression alters cellular cholesterol homeostasis. *J. Biol. Chem.* **275,** 38445–38451 (2000).

215. Vanier, M. T. & Millat, G. Niemann-Pick disease type C. *Clin. Genet.* **64,** 269–281 (2012).

216. Fernandez-Valero, E. M. *et al.* Identification of 25 new mutations in 40 unrelated Spanish Niemann-Pick type C patients: Genotype-phenotype correlations. *Clin. Genet.* **68,** 245–254 (2005).

217. Cologna, S. M. *et al.* Quantitative Proteomic Analysis of Niemann-Pick Disease, Type C1 Cerebellum Identifies Protein Biomarkers and Provides Pathological Insight. *PLoS One* **7,** (2012).

218. Porter, F. D. *et al.* Cholesterol oxidation products are sensitive and specific blood-based biomarkers for Niemann-Pick C1 disease. *Sci. Transl. Med.* **2,** 1–12 (2010).

219. Fan, M. *et al.* Identification of Niemann-Pick C1 disease biomarkers through sphingolipid profiling. *J. Lipid Res.* **54,** 2800–14 (2013).

220. Kukulski, W. *et al.* Correlated fluorescence and 3D electron microscopy with high sensitivity and spatial precision. *J. Cell Biol.* **192,** 111–119 (2011).

221. Kågedal, K., Zhao, M., Svensson, I. & Brunk, U. T. Sphingosine-induced apoptosis is dependent on lysosomal proteases. *Biochem. J.* **359,** 335–343 (2001).

222. Kirkegaard, T. *et al.* Hsp70 stabilizes lysosomes and reverts Niemann-Pick disease-associated lysosomal pathology. *Nature* **463,** 549–553 (2010).

223. Subramanian, D. *et al.* Activation of membrane-permeant caged PtdIns(3)P induces endosomal fusion in cells. *Nat. Chem. Biol.* **6,** 324–326 (2010).

224. Wickham, H. ggplot2: elegant graphics for data analysis. (2009).

225. Cohen, S. A. & Michaud, D. P. Synthesis of a fluorescent derivatizing reagent, 6-aminoquinolyl-N-hydroxysuccinimidyl carbamate, and its application for the analysis of hydrolysate amino acids via high-performance liquid chromatography. *Anal. Biochem.* **211,** 279–287 (1993).

226. Bock, T. *et al.* An integrated approach for genome annotation of the eukaryotic thermophile Chaetomium thermophilum. *Nucleic Acids Res.* **42,** 13525–13533 (2014).

List of Abbreviations

AA	amino acid
AcOH	acetic acid
AM	acetoxymethyl
ATP	adenosine triphosphate
BFDAG	bifunctional diacylglycerol
BFS	bifunctional sphingosine
BODIPY	boron-dipyrromethene
bp	base pair
BSA	bovine serum albumin
C1P	ceramide-1-phosphate
cADPR	cyclic adenosine diphosphate ribose
CDase	ceramidase
CDS	glucosylceramide synthase
Cer	ceramide
CerK	ceramide kinase
CerS	ceramide synthase
CERT	ceramide transfer protein
CHO	chinese hamster ovary (cells)
CLEAR	coordinated lysosomal expression and regulation (network)
CoA	coenzyme A
DAG	diacylglycerol
DCM	dichloromethane
DEAC	*N,N*-diethylaminocoumarin
DES	sphingolipid desaturase
dhCer	dihydroceramide
dhSph	dihydrosphingosine, sphinganine
DIPEA	diisopropylethylamine
DKO	double knock out
DMEM	Dulbecco's Modified Eagle Medium
DMNB	4,5-dimethoxy-nitrobenzyl
DMS	dimethylsphingosine
DMSO	dimethylsulfoxide
DNA	desoxyribonucleic acid

DTT	dithiothreitol
EBOV	Ebola virus
EDTA	ethylene diamine tetraacetic acid
EGTA	ethylene glycol tetraacetic acid
ER	endoplasmic reticulum
EtOAc	ethylacetate
FDR	false discovery rate
GalCer	galactosylceramide
GBA	glucosylceramidase
GluCer	glucosylceramide
GM130	*cis*-Golgi matrix protein 130
GO	gene ontology
GP	glycoprotein
GPN	glycyl-L-phenylalanine 2-naphtylamide
HEPES	4-(2-hydroxyethyl)-1-piperazineethanesulfonic acid
HOPS	homotypic fusion and vacuole protein-sorting
HPLC	high performance liquid chromatography
HPTLC	high performance thin layer chromatography
HRMS	high resolution mass spectrometry
HSAN1	hereditary sensory and autonomic neuropathy type I
$InsP_3R$	inositol-triphophate receptor
KDSR	3-ketodihydrosphingosine reductase
LAMP-1	lysosomal associated membrane protein 1
LB	Luria-Bertani
LC	liquid chromatography
LE	late endosome
MARV	Marburg virus
MeOH	methanol
MLIV	mucolipidosis type IV
MS	mass spectrometry
mTORC	mechanistic target of rapamycin complex
NAADP	nicotinic acid adenine dinucleotide phosphate
NBD	nitrobenoxadiazole
NMR	nuclear magnetic resonance
NPC	Niemann-Pick type C
NTP	nucleotide triphosphate
OD	optical density
Osh	oxysterol binding protein homolog
pacSph	photoactivatable and clickable sphinogsine
PBS	phosphate buffered saline
PC	phosphatidylcholine
PCR	polymerase chain reaction
PE	phosphatidylethanolamine
$PI(3,5)P_2$	phophatidylinositol (3,5)-bisphosphate

PIC	protease inhibitor cocktail
PM	plasma membrane
PSM	peptide spectral matches
RNAi	ribonucleic acid interference
ROI	region of interest
RT	room temperature
RyR	ryanodine receptor
S1P	sphingosine-1-phosphate
S1PL	sphingosine-1-phosphate lyase
S1PR	sphingosine-1-phosphate receptor
SAG	stearoyl-arachinoylglycerol
SDS	sodium dodecylsulfate
siRNA	small interfering ribonucleic acid
SKI-II	sphingosine kinase inhibitor II
SM	sphingomyelin
SMase	sphingomyelinase
SMS	sphingomyelin synthase
SOC	super optimal broth with catabolite repression
Sph	sphingosine
SK	sphingosine kinase
SPT	serine palmitoyl transferase
SSD	sterol sensing domain
TAP	tandem affinity purification
TBE	Tris buffered EDTA
TEA	triethylamine
TFDAG	trifunctional diacylglycerol
TFEB	transcription factor EB
TFFA	trifunctional fatty acid
TFS	trifunctional sphingosine
THF	tetrahydrofuran
TLC	thin layer chromatography
TPC	two-pore channels
Trp	transient receptor potential
UPLC	ultra performance liquid chromatography
UV	ultraviolet
*v*ATPase	vacuolar H^+-adenylpyrophosphatase
VGCC	voltage gated calcium channels
WT	wild type

Appendix A – NMR spectra

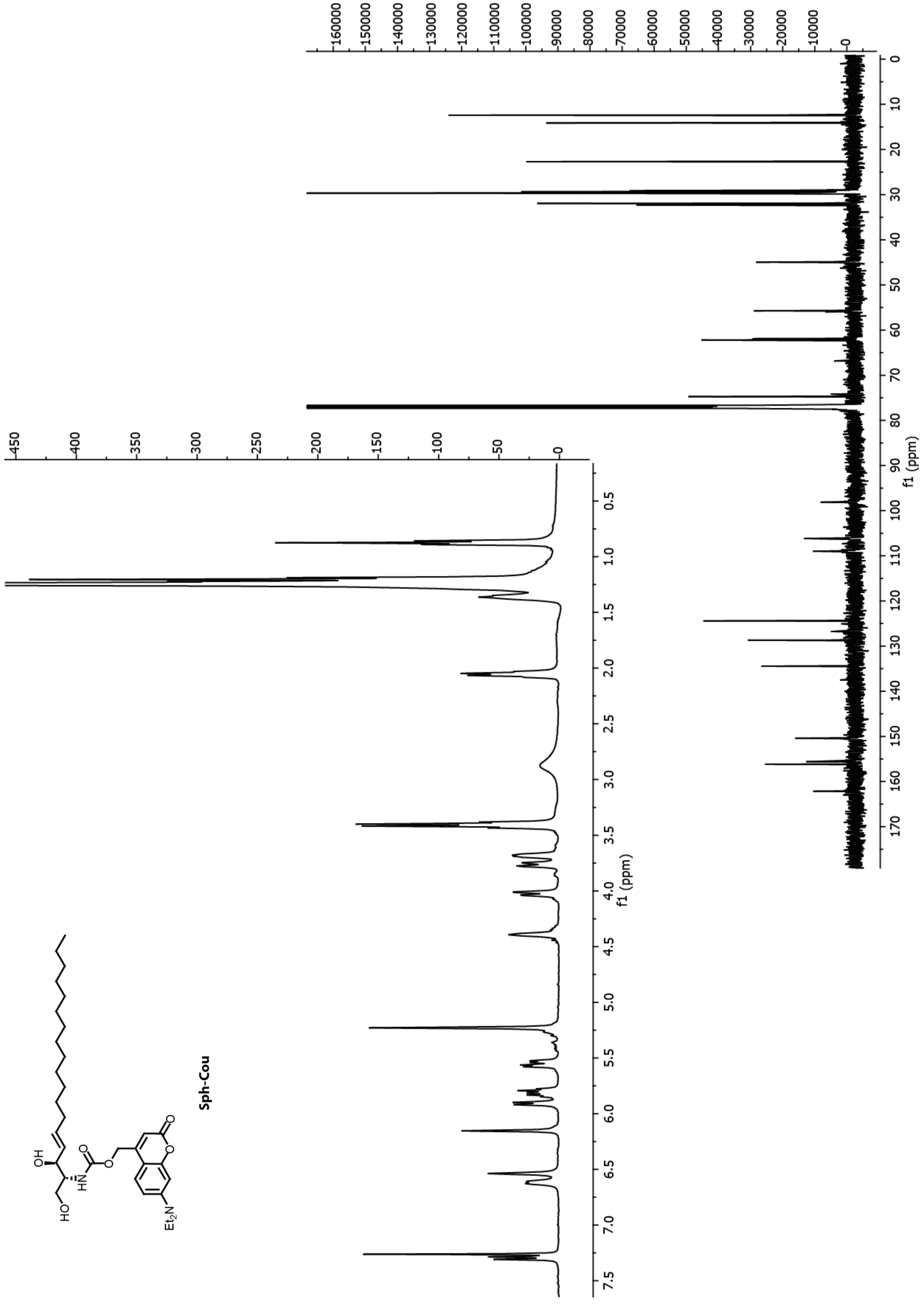

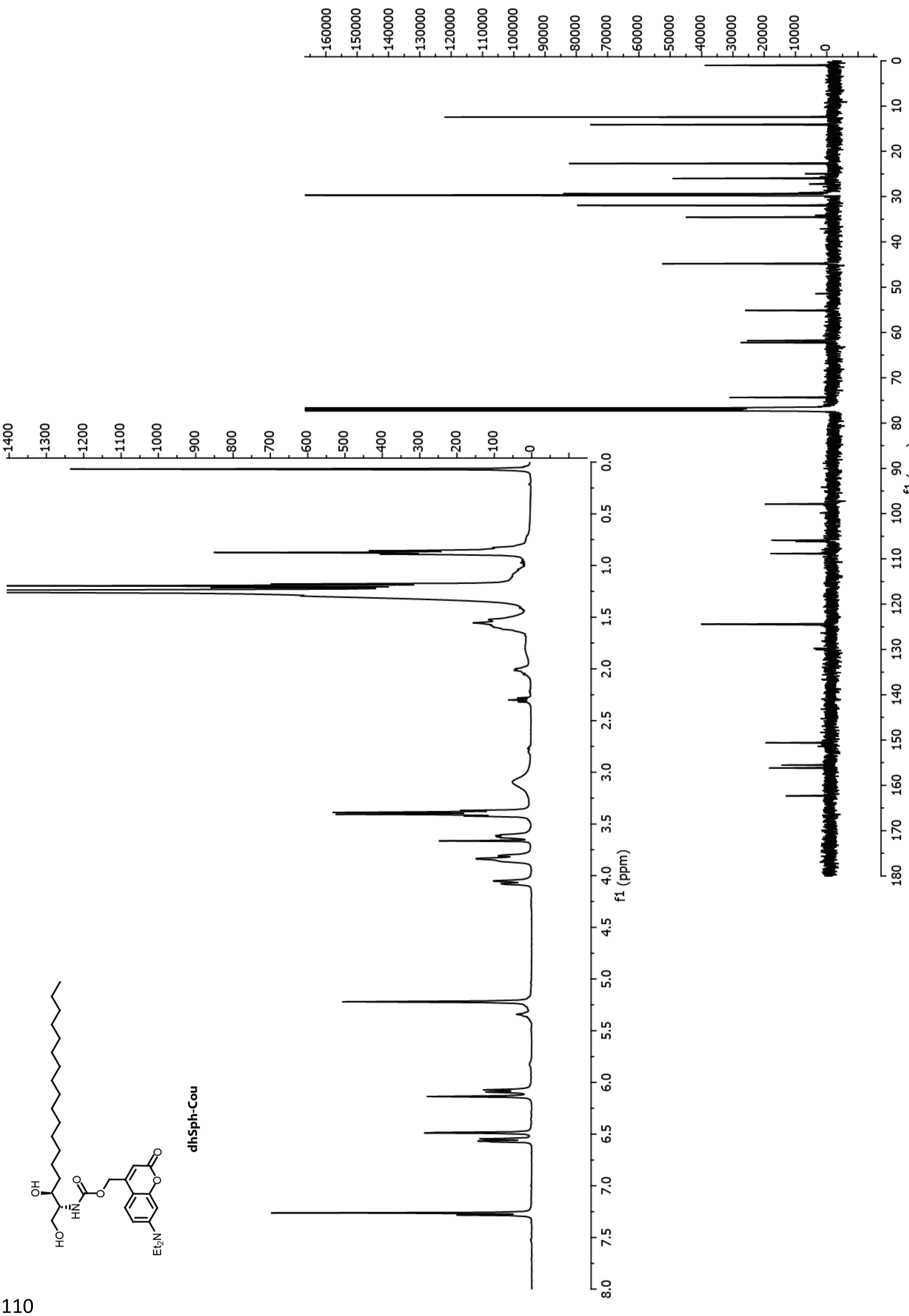
HO
OH
HN
O
O
O
O
Et$_2$N
f1 (ppm)
0.0
0.5
1.0
1.5
2.0
2.5
3.0
3.5
4.0
4.5
5.0
5.5
6.0
6.5
7.0
7.5
8.0
1400
1300
1200
1100
1000
900
800
700
600
500
400
300
200
100
0
f1 (ppm)
0
10
20
30
40
50
60
70
80
90
100
110
120
130
140
150
160
170
180
160000
150000
140000
130000
120000
110000
100000
90000
80000
70000
60000
50000
40000
30000
20000
10000
0

dhSph-Cou

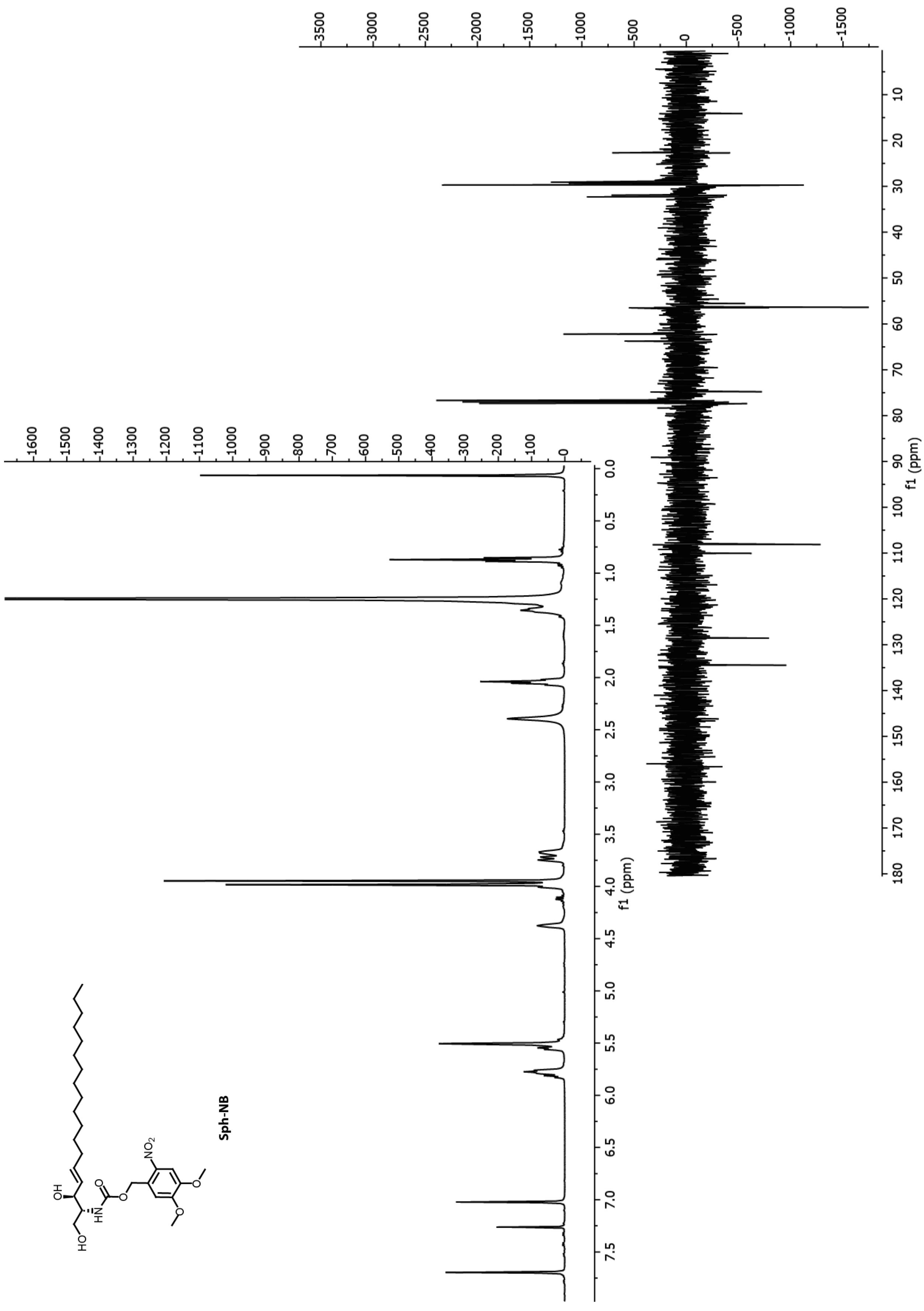
3500
3000
2500
2000
1500
1000
500
0
-500
-1000
-1500
10
20
30
40
50
60
70
80
90
100
110
120
130
140
150
160
170
180
f1 (ppm)
1600
1500
1400
1300
1200
1100
1000
900
800
700
600
500
400
300
200
100
0
0.0
0.5
1.0
1.5
2.0
2.5
3.0
3.5
4.0
4.5
5.0
5.5
6.0
6.5
7.0
7.5
f1 (ppm)
OH
HO
HN
O
O
NO2
O
O

Sph-NB

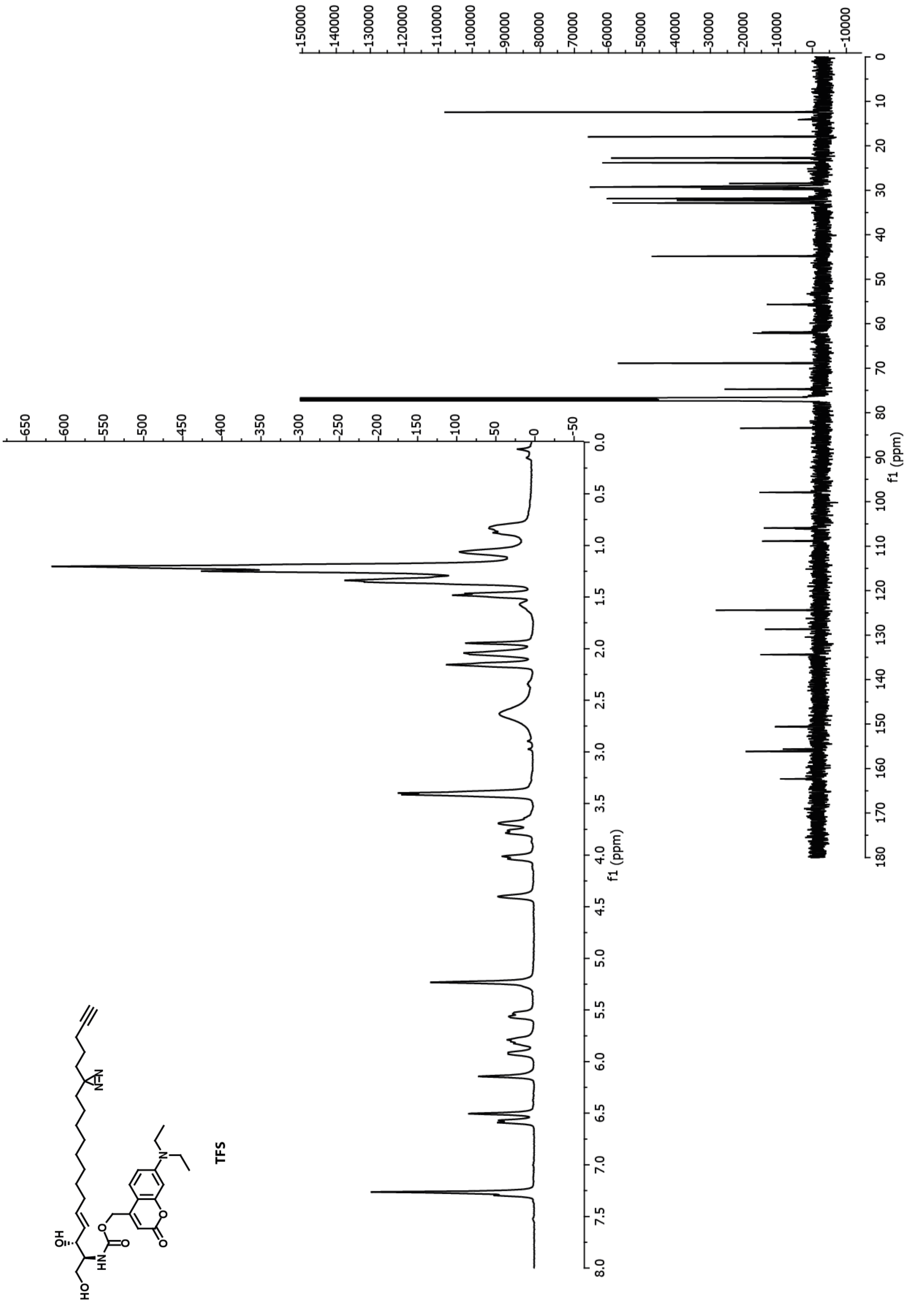
f1 (ppm)
0.0
0.5
1.0
1.5
2.0
2.5
3.0
3.5
4.0
4.5
5.0
5.5
6.0
6.5
7.0
7.5
8.0
f1 (ppm)
0
10
20
30
40
50
60
70
80
90
100
110
120
130
140
150
160
170
180
650
600
550
500
450
400
350
300
250
200
150
100
50
0
-50
150000
140000
130000
120000
110000
100000
90000
80000
70000
60000
50000
40000
30000
20000
10000
0
-10000
HO
OH
HN
O
N=N
N

TFS

Appendix B – Results of proteomic screens

B.1. List of high confidence Sph-binding proteins

description	size [aa]	function	localization
Prolow-density lipoprotein receptor-related protein 1 GN=LRP1	4544	endocytosis of apoptotic cells	PM
DnaJ homolog subfamily C member 1 GN=DNAJC1	554	protein synthesis, DNA binding	ER, nucleus
SUN domain-containing protein 2 GN=SUN2	717	cytoskeleton, nucleoskeleton	nucleus
Leucyl-cystinyl aminopeptidase GN=LNPEP	1025	Zn binding, peptide hormone degradation	membrane
Endothelin-converting enzyme 1 GN=ECE1 PE=2 SV=1	770	catalysis of endothelin conversion, binds Zn	PM
C-type mannose receptor 2 GN=MRC2	1479	internalizes glycosylated ligands	membrane
Cation-dependent mannose-6-phosphate receptor GN=M6PR	277	endosome to lysosome transport	lysosome
3-ketodihydrosphingosine reductase GN=KDSR	332	de novo synthesis, nucleotide binding	ER
Protein sel-1 homolog 1 GN=SEL1L	794	ER quality ctrl, notch signaling	ER
Transmembrane emp24 domain-containing protein 2 GN=TMED2	201	secretory pathway	Golgi, endosome
Proactivator polypeptide = Prosaposin GN=PSAP	524	GlcCer hydrolysis	lysosome
Ceramide synthase 2 GN=LASS2	380	suppresses growth of cancer cells	ER
Isoform 3 of Transmembrane protein 87A GN=TMEM87A	555		membrane
C-X-C chemokine receptor type 4 GN=CXCR4	352	activation increases Ca^{2+} und MAPK	PM
Translocating chain-associated membrane protein 1 GN=TRAM1	374	protein translation, targeting	ER
Golgi integral membrane protein 4 GN=GOLIM4	696	protein transport from endosome to Golgi	Golgi, endosome
Vacuole membrane protein 1 GN=VMP1	406	autophagy	vesicle
Putative peripheral benzodiazepine receptor-related protein GN=TSPO	169	porphyrin, Heme-binding, lipid transport	mitochondria
UPF0420 protein C16orf58 GN=C16orf58	460		membrane
Lysosomal Pro-X carboxypeptidase GN=PRCP	496	peptide cleavage, blood coagulation	lysosome
Translocase of inner mitochondrial membrane domain-containing	285	chaperone of mitochondrial complex 1	mitochondria
B-cell receptor-associated protein 29 GN=BCAP29	230	protein transport	ER
Isoform 4 of Clusterin GN=CLU	449	blood coagulation, myelin maintenance	secreted
Isoform 3 of Atlastin-2 GN=ATL2	583	GTPase, ER biogenesis	ER
Cathepsin B GN=CTSB	339	thiol protease	lysosome
Transmembrane protein 59 GN=TMEM59	323	autophagy regulation in *S.aureus*	LE/lysosome
Carbohydrate sulfotransferase 3 GN=CHST3	479	carbohydrate metabolism	Golgi
Phosphatidylinositol transfer protein alpha isoform GN=PITPNA	270	PI, PC transporter	cytoplasm
Secretory carrier-associated membrane protein 2 GN=SCAMP2	329	post-Golgi recycling pathway	Golgi
Beta-hexosaminidase subunit alpha GN=HEXA	529	GM2 degradation	lysosome
Reticulocalbin-2 GN=RCN2	317	binds calcium	ER
Inter-alpha-trypsin inhibitor heavy chain H3 GN=ITIH3	890	trypsin inhibitor	secreted
Isoform 5 of Amyloid-like protein 2 GN=APLP2	763	trypsin inhibitor, hemostasis,	PM, nucleus
Protein S100-A8 = Calprotectin GN=S100A8	93	Ca^{2+}, Zn^{2+} and arachidonic acid binding	cytoplasm
Heme-binding protein 1 GN=HEBP1	189	porphyrin-binding, circadian rhythm	cytoplasm
Protein S100-A9 GN=S100A9	114	Ca^{2+}, Zn^{2+} and arachidonic acid binding	cytoplasm,
Putative disease resistance protein GN=SLC30A5	765	zinc transporter	Golgi
Mitochondrial cardiolipin hydrolase GN=PLD6	252	stimulated by Ca^{2+} and Mn^{2+}	MOM
Beta-hexosaminidase subunit beta GN=HEXB	556	GM2 degradation	lysosome
Glycerophosphodiester phosphodiesterase 1 GN=GDE1	331	binds Mg,	cytoplasm, PM
DnaJ homolog subfamily C member 3 GN=DNAJC3	504	UR, ER stress, chaperone	ER
ADP-ribosylation factor-like protein 6-interacting protein 6 GN=ARL6IP6	226		membrane
Protocadherin Fat 1 GN=FAT1	4588	polarization, migration, binds Ca^{2+}	PM, nucleus
Ras-related protein Rab-31 GN=RAB31	194	GTPase, secretory pathway	Golgi, endosome
CMP-N-acetylneuraminate-beta-galactosamide-alpha-2,3-	333	protein glycosylation	Golgi, secreted
CD276 antigen GN=CD276	534	T-cell mediated immune response	plasma
CDGSH iron-sulfur domain-containing protein 1 GN=CISD1	108	oxidative phosphorylation	mitochondria
Mitochondrial import inner membrane translocase subunit Tim22	194	protein import, targeting to mitochondria	mitochondria
Isoform 4 of Mitochondrial fission factor GN=MFF	342	peroxisomal fission, synaptic vesicles	mitochondria

Transmembrane protein 160 GN=TMEM160	188		membrane
Protein FAM8A1 GN=FAM8A1	413		membrane
Protein PRRC1 GN=PRRC1	620	cytokinesis regulator	cytoskeleton
Transmembrane emp24 domain-containing protein 3 GN=TMED3	217	early secretory pathway	Golgi, ER
Protein C5orf15 GN=C5orf15	265	keratinocyte-associated Tmem2	membrane
Connective tissue growth factor GN=CTGF	349	proliferation in chondrocytes	secreted
Protein FAM3A GN=FAM3A	230	cytokine like protein	secreted
Isoform 3 of UBX domain-containing protein 8 GN=UBXN8	270	ER quality control	ER
Polypeptide N-acetylgalactosaminyltransferase 3 GN=GALNT3	633	protein glycosylation, binds Ca^{2+} and Mn^{2+}	Golgi
Peroxisomal membrane protein PEX16 GN=PEX16	336	peroxisome biogenesis	peroxisome
Lysosome-associated membrane glycoprotein 2 GN=LAMP2	410	protection of lys membrane	lysosome
StAR-related lipid transfer protein 3 GN=STARD3	445	cholesterol transport	LE /lysosome
2-hydroxyacylsphingosine 1-beta-galactosyltransferase GN=UGT8	541	GalCer synthesis	membrane
Galectin-3-binding protein GN=LGALS3BP	585	cell adhesion, host defense	secreted
Isoform 3 of Solute carrier family 35 member F2 GN=SLC35F2	374	solute transporter	membrane
Sodium/hydrogen exchanger 6 GN=SLC9A6	669	calcium homeostasis	endosomes
Transmembrane protein with metallophosphoesterase domain	453	binds 2-divalent metal cations	membrane
Isoform K of Membrane cofactor protein GN=CD46	392	cofactor for serine protease	vesicle
Peptidyl-glycine alpha-amidating monooxygenase GN=PAM	973	amidation of peptides	secreted
Carboxypeptidase D GN=CPD	1380	binds Zn, peptidase activity	membrane
D-glucuronyl C5-epimerase GN=GLCE	617	glycan metabolism, heparin biosynthesis	Golgi
Isoform 5 of Polycystin-2 GN=PKD2	968	calcium channel in cillia	cillium
Collagen alpha-1(V) chain GN=COL5A1	1838	type v collagen, binds calcium	secreted
Isoform 3 of Tax1-binding protein 1 GN=TAX1BP1	789	TNF-induced apoptosis	cytosol

B.2. List of high-confidence DAG-binding proteins

description	size [aa]	function	localization
Guanine nucleotide-binding protein subunit beta-2 GN=GNB2	340	Ca-channel activatoin	cytoplasm
Guanine nucleotide-binding protein subunit beta-1 GN=GNB1	340	Ras signal transduction	cytoplasm
DNA replication licensing factor MCM3 GN=MCM3	808	DNA replication initiation	nucleus
Mitochondrial import receptor subunit TOM40 GN=TOMM40	361	mitochondrial transport	mitochondria
Microtubule-associated protein 4 GN=MAP4	1152	promotes microtubule assembly	cytoskeleton
Isoform 2 of Tyrosine-protein kinase BAZ1B GN=BAZ1B	1483	chromatin remodeling	nucleus
40S ribosomal protein S27-like GN=RPS27L	84	endopeptidase activator	nucleus, ribosome
Isoleucine--tRNA ligase, cytoplasmic GN=IARS	1262	tRNA editing	cytoplasm
Isoform 3 of Palladin GN=PALLD	1383	actin binding	cytoskeleton
40S ribosomal protein S3a GN=RPS3A	264	regulation of TF DDITT3	nucleus
Eukaryotic translation initiation factor 3 subunit D GN=EIF3D	548	protein synthesis	cytoplasm
ATP-dependent RNA helicase DDX1 GN=DDX1	740	double-strand break repair	cytoplasm, nucleus
Bifunctional purin biosynthesis protein PURH GN=ATIC	592	purine biosynthesis	cytoplasm
Phosphoglycerate kinase 1 GN=PGK1	417	polymerase alpha cofactor	cytoplasm
Threonine--tRNA ligase, cytoplasmic GN=TARS	723	threonine-tRNA ligation	cytoplasm
2-oxoglutarate dehydrogenase complex, mitochondrial GN=DLST	453	L-lysine degradation	mitochondria
Isoform 4 of Plasminogen activator inhibitor 1 RNA-binding protein	408	mRNA stability	cytoplasm, nucleus
Nucleolar protein 58 GN=NOP58	529	biogenesis of boxC/D snoRNAs	nucleus
Serine palmitoyltransferase 2 GN=SPTLC2	562	sphingolipid synthesis	ER
Serine/threonine-protein phosphatase 2A subunit A GN=PPP2R1A	589	chromosome segregation	Cytoplasm
Zinc finger CCCH domain-containing protein 15 GN=ZC3H15	426	inhibits DRG1 degradation	cytoplasm, nucleus
NADH-ubiquinone oxidoreductase, mitochondrial GN=NDUFS1	727	cellular respiration	mitochondria
THO complex subunit 2 GN=THOC2	1593	mRNA export	nucleus
Transgelin-2 GN=TAGLN2	199	epithelial cell differentiation	vesicle
Probable ATP-dependent RNA helicase DDX27 GN=DDX27	796	RNA unwinding	nucleus
Ras-related C3 botulinum toxin substrate 1 GN=RAC1	192	GTPase	PM, cytoplasm
Macrophage-capping protein GN=CAPG	348	calcium binding	cytoplasm, nucleus

Dihydroxyacetone phosphate acyltransferase GN=GNPAT	680	gylcerophospholipid metabolism	peroxisome
Cell division cycle 27, isoform CRA_c GN=CDC27	823	cell division	nucleus
Isoform 3 of Protein AHNAK2 GN=AHNAK2	5795	interacts with DYSF	nucleus
Zinc finger CCCH domain-containing protein 14 GN=ZC3H14	736	mRNA stability in neurons	nucleus
DNA-directed RNA polymerase I subunit RPA1 GN=POLR1A	1720	RNA transcription	nucleus
Phosphoglycerate kinase GN=PGK1	242	glycolytic process	cytoplasm
60S ribosomal protein L10 GN=RPL10	163	protein translation	ribosome
Isoform 2 of Nuclear pore complex protein Nup50 GN=NUP50	468	nuclear protein import	nucleus
Dihydropyrimidinase-related protein 3 GN=DPYSL3	570	cytoskeleton remodeling	cytoplasm
Asparagine--tRNA ligase, cytoplasmic GN=NARS	548	protein translation	cytoplasm
Isoform 4 of A-kinase anchor protein 2 GN=AKAP2	859	cell polarity, PKA binding	cytoplasm
Pescadillo homolog GN=PES1	571	maturation of rRNA	nucleus
NUP153 variant protein GN=NUP153 variant protein	1475	nuclear transport	nucleus
Probable ATP-dependent RNA helicase DHX36 GN=DHX36	797	RNA processing	cytoplasm, nucleus
Isoform 2 of Triosephosphate isomerase GN=TPI1	286	gluconeogenesis	cytoplasm
40S ribosomal protein S16 GN=RPS16	146	protein translation	cytoplasm, ribosome
Apolipoprotein O-like GN=APOOL	268	mitochondrial architecture	mitochondria
Mitochondrial glutamate carrier 1 GN=SLC25A22	323	glutamate carrier	mitochondria
Actin-related protein 3 GN=ACTR3	418	regulation of actin polymerization	cytoskeleton
Isocitrate dehydrogenase [NAD], mitochondrial GN=IDH3A	331	oxidoreduction	mitochondria
26S protease regulatory subunit 7 GN=PSMC2	433	protein degradation	cytoplasm
Protein DEK GN=DEK	375	chromatin organization	nucleus
Tyrosine--tRNA ligase, cytoplasmic GN=YARS	528	gene expression	cytoplasm
Isoform 2 of Putative adenosylhomocysteinase 2 GN=AHCYL1	530	mRNA processing	ER, cytoplasm
Isoform 5 of Microtubule-associated protein 4 GN=MAP4	1152	microtubule assembly	cytoskeleton
Periodic tryptophan protein 2 homolog GN=PWP2	919	RNA binding	nucleus
DNA mismatch repair protein Msh2 GN=MSH2	934	DNA repair	nucleus
DNA-directed RNA polymerase GN=POLR2B	1099	transcription	nucleus
Cyclin-dependent kinase 9 GN=CDK9	372	transcription regulation	nucleus
Ribonucleases P/MRP protein subunit POP1 GN=POP1	1024	tRNA maturation	nucleus
WD repeat-containing protein 36 GN=WDR36	951	rRNA processing	nucleus
NF-X1-type zinc finger protein NFXL1 GN=NFXL1	911	RNA polymerase II dependent	nucleus
Disks large homolog 1 GN=DLG1	904	scaffolding protein	PM
Cullin-associated NEDD8-dissociated protein 1 GN=CAND1	1230	protein ubiquitination	cytoplasm, nucleus
Up-regulated during skeletal muscle growth protein 5 GN=USMG5	58	ATP synthesis	mitochondria
Brain acid soluble protein 1 GN=BASP1	227	gonad development	PM
Adenylate kinase 2, mitochondrial GN=AK2	239	energy homeostasis	mitochondria
LIM and SH3 domain protein 1 GN=LASP1	261	cytoskeletal regulation	cytoskeleton
ATP synthase subunit O, mitochondrial GN=ATP5O	213	respiration	mitochondria
Calponin-3 GN=CNN3	329	actomyosin structure	cytoskeleton
Eukaryotic translation initiation factor 3 subunit I GN=EIF3I	325	protein synthesis	cytoplasm
Pachytene checkpoint protein 2 homolog GN=TRIP13	432	chromosome recombination	nucleus
Quinone oxidoreductase GN=CRYZ	329	catabolism of xenobiotics	cytoplasm
MKI67 FHA domain-interacting nucleolar phosphoproteinGN=MKI67IP	293	rRNA transcription	nucleus
DNAJC7 protein GN=DNAJC7	494	HSP regulation	cytoplasm, nucleus
Lysophosphatidylcholine acyltransferase 2 GN=LPCAT2	544	phospholipid metabolism	ER, Golgi
SUMO-activating enzyme subunit 1 GN=SAE1	346	protein sumoylation	nucleus
Protein FAM49B GN=FAM49B	324	-	cilium, exosome
UBX domain-containing protein 4 GN=UBXN4	508	unfolded protein response	ER
Glucose-6-phosphate isomerase GN=GPI	558	glycolysis	cytoplasm
EH domain-containing protein 4 GN=EHD4	541	endosomal transport	endosome
Protein phosphatase 1G GN=PPM1G	546	serine/threonine phosphatase	cytoplasm
Isoform 3 of Leukotriene A-4 hydrolase GN=LTA4H	611	leukotriene B4 biosynthesis	cytoplasm
DNA mismatch repair protein Msh6 GN=MSH6	1360	DNA repair	nucleus
Pre-rRNA-processing protein TSR1 homolog GN=TSR1	804	ribosome maturation	nucleus
Isoform 2 of Calpain-2 catalytic subunit GN=CAPN2	700	non-lysosomal proteolysis	cytoplasm
Condensin complex subunit 1 GN=NCAPD2	1401	chromatin condensation	nucleus, cytoplasm
Myosin light polypeptide 6 GN=MYL6	151	muscle contraction	cytoplasm

40S ribosomal protein S21 GN=RPS21	83	gene expression	cytoplasm, ribosome
Isoform 3 of Ethylmalonyl-CoA decarboxylase GN=ECHDC1	307	metabolite proofreading	cytoplasm
60S ribosomal protein L18a GN=RPL18A	154	gene expression	ribosome
Ubiquitin carboxyl-terminal hydrolase GN=USP14	494	protein degradation	cytoplasm
Isoform 4 of Glutathione S-transferase kappa 1 GN=GSTK1	226	disulfide oxidoreduction	peroxisome
Copine-3 GN=CPNE3	537	membrane trafficking	cytoplasm, PM
Histidine--tRNA ligase, cytoplasmic GN=HARS	509	translation	cytoplasm
Isoform 2 of U4/U6 small nuclear ribonucleoprotein Prp4 GN=PRPF4	522	pre-mRNA splicing	nucleus
Signal recognition particle 72 kDa protein GN=SRP72	671	secretory protein targeting	ER
WD repeat-containing protein 74 GN=WDR74	385	blastocyst formation	nucleus
DnaJ homolog subfamily B member 11 GN=DNAJB11	358	unfolded protein response	ER
Isoform 2 of Cullin-4B GN=CUL4B	913	protein degradation	nucleus
WD repeat-containing protein 1 GN=WDR1	606	actin disassembly	cytoskeleton
Isoform 3 of Apoptosis inhibitor 5 GN=API5	524	binds to ACIN1	nucleus
MAGUK p55 subfamily member 6 GN=MPP6	160	rRNA maturation	nucleus
4-trimethylaminobutyraldehyde dehydrogenase GN=ALDH9A1	494	carnitine biosynthesis	cytoplasm
Coatomer subunit delta GN=ARCN1	511	intracellular transport	Golgi, vesicle
Dystrophin GN=DMD	3685	actin binding	PM, cytoskeleton
ATP-binding cassette sub-family E member 1 GN=ABCE1	599	mRNA turnover	cytoplasm, mito
Isoform 5 of N-terminal kinase-like protein GN=SCYL1	808	COPI-retrograde traffic	Golgi, ER, vesicle
CCAAT/enhancer-binding protein zeta GN=CEBPZ	1054	transcription regulation	nucleus
Protein transport protein Sec24D GN=SEC24D	1032	COPII coat	ER, Golgi, cytoplasm
Putative PIP5K1A and PSMD4-like protein GN=PIPSL	862	protein degradation	cytoplasm
Fibronectin type III domain-containing protein 3B GN=FNDC3B	1204	adipogenesis	PM
Golgi-specific guanine nucleotide exchange factor 1 GN=GBF1	1859	early secretory pathway trafficking	ER, Golgi, cytoplasm
40S ribosomal protein S23 GN=RPS23	143	translation	cytoplasm, ribosome
Isoform 2 of Proteasome subunit alpha type-3 GN=PSMA3	255	protein degradation	cytoplasm
Deoxyuridine 5'-triphosphate nucleotidohydrolase, mitocho. GN=DUT	252	nucleotide metabolism	nucleus
26S proteasome non-ATPase regulatory subunit 4 GN=PSMD4	377	protein degradation	cytoplasm
PDZ and LIM domain protein 5 GN=PDLIM5	596	scaffolding protein	cytoskeleton
Isoform 2 of Transcription factor BTF3 GN=BTF3	206	transcription	cytoplasm, nucleus
Isoform 2 of Nuclear RNA export factor 1 GN=NXF1	619	RNA transport	nucleus, cytoplasm
Nitric oxide synthase-interacting protein GN=NOSIP	301	inhibits NO production	cytoplasm, nucleus
40S ribosomal protein S13 GN=RPS13	151	gene expression	cytoplasm, ribosome
Serpin B5 GN=SERPINB5	375	tumor suppressor	secreted
Isoform 2 of 28S ribosomal protein S29, mitochondrial GN=DAP3	398	apoptosis	mitochondria
26S protease regulatory subunit 10B GN=PSMC6	389	protein degradation	cytoplasm, nucleus
Syntaxin-binding protein 1 GN=STXBP1	594	synaptic vesicle fusion	cytoplasm, PM
Fructose-bisphosphate aldolase GN=ALDOC	364	carbohydrate degradation	cytoplasm, exosome
Serine/threonine-protein phosphatase GN=PPP4C	307	dephosphorylation	cytoplasm, nucleus
Retinoic acid receptor RXR-beta GN=RXRB	533	gene expression regulation	nucleus
Isoform Short of Ancient ubiquitous protein 1 GN=AUP1	476	protein degradation	ER, cytoplasm
RNA-binding motif, single-stranded-interacting protein 1 GN=RBMS1	370	RNA binding	
COP9 signalosome complex subunit 4 (Fragment) GN=COPS4	406	ubiquitin conjugation	cytoplasm, nucleus
mRNA cap guanine-N7 methyltransferase GN=RNMT	476	gene expression	nucleus
Isoform 3 of Septin-10 GN=SEPT10	454	cytokinesis	cytoskeleton
Serine/threonine phosphatase 2A subunit B alpha, GN=PPP2R2A	447	dephosphorylation	cytoplasm
Copine-1 GN=CPNE1	537	membrane trafficking	cytoplasm
Tyrosine-protein phosphatase non-receptor type 11 GN=PTPN11	597	signal transduction	cytoplasm
phosphatidylinositol 4,5-bisphosphate phosphodiesterase delta-3 GN=PLCD3	789	PIP2 hydrolysis	PM, cytoplasm
Complement decay-accelerating factor GN=CD55	381	lipid binidng	PM
Isoform 2 of Protein unc-45 homolog A GN=UNC45A	944	chaperone for HSP90	cytoplasm
WD repeat-containing protein 5 GN=WDR5	334	histone modification	nucleus
Ribosomal RNA-processing protein 1 homolog A GN=RRP1	461	rRNA generation	nucleus
Fanconi anemia group I protein GN=FANCI	1090	DNA repair	
FAS-associated factor 1 GN=FAF1	650	apoptosis	nucleus
Calpain-1 catalytic subunit GN=CAPN1	714	non-lysosomal proteolysis	cytoplasm
Peroxisomal biogenesis factor 3 GN=PEX3	373	membrane protein import	peroxisome

Phosphoribosylformylglycinamidine synthase GN=PFAS	1338	purine biosynthesis	cytoplasm
Isoform 2 of Reactive oxygen species modulator 1 GN=ROMO1	79	cell proliferation	mitochondria
Serine-threonine kinase receptor-associated protein GN=STRAP	350	pre-mRNA splicing	cytoplasm, nucleus
Actin-related protein 2/3 complex subunit 4 GN=ARPC4	113	actin polymerization	cytoskeleton
Eukaryotic translation initiation factor 5A-1 GN=EIF5A	154	translation elongation	cytoplasm, nucleus
Dolichol-phosphate mannosyltransferase subunit 3 GN=DPM3	92	protein glycosylation	ER
Phosphoribosylaminoimidazole-succinocarboxamide synthase GN=PAICS	425	IMP biosynthesis	cytoplasm
NADH dehydrogenase [ubiquinone] 1 alpha subcomplex subunit 4 GN=NDUFA4	81	respiration	mitochondria
Creatine kinase B-type GN=CKB	381	energy transduction	cytoplasm
ATP synthase subunit d, mitochondrial GN=ATP5H	161	energy homeostasis	mitochondria
Probable ribosome biogenesis protein RLP24 GN=RSL24D1	66	translation	cytoplasm, ribosome
Hypoxanthine-guanine phosphoribosyltransferase GN=HPRT1	218	purine salvage	cytoplasm
28S ribosomal protein S18b, mitochondrial GN=MRPS18B	258	translation	mitochondria
Ras-related protein Rap-2a GN=RAP2A	183	cell migration	recycling endosome
CCR4-NOT transcription complex subunit 10 GN=CNOT10	744	mRNA degradation	cytoplasm, nucleus
Ubiquitin carboxyl-terminal hydrolase isozyme L5 GN=UCHL5	218	protein degradation	cytoplasm
NEDD8-conjugating enzyme Ubc12 GN=UBE2M	183	ubiquitin conjugation	cytoplasm
Peptidyl-prolyl cis-trans isomerase E GN=PPIE	301	protein folding	nucleus
Isoform 2 of Proteasome assembly chaperone 1 GN=PSMG1	288	protein degradation	ER, cytoplasm
Glyoxylate reductase/hydroxypyruvate reductase GN=GRHPR	328	oxidoreduction	cytoplasm
Phenylalanine--tRNA ligase beta subunit GN=FARSB	589	translation	cytoplasm
Protein disulfide-isomerase A5 GN=PDIA5	519	oxidoreduction	ER
Exportin-7 GN=XPO7	1087	nuclear protein export	cytoplasm, nucleus
Endophilin-A2 GN=SH3GL1	368	endocytosis	early endosome
RNA-binding protein PNO1 GN=PNO1	252		nucleus
Protein kish-A GN=TMEM167A	72	early secretory pathway	Golgi
Replication factor C subunit 5 GN=RFC5	340	DNA replication	nucleus
Signal peptidase complex subunit 3 GN=SPCS3	180	translation	ER, microsome
Eukaryotic translation initiation factor 3 subunit G GN=EIF3G	320	protein synthesis	cytoplasm, nucleus
Ribonucleoside-diphosphate reductase subunit M2 GN=RRM2	389	DNA replication	cytoplasm
F-box only protein 22 GN=FBXO22	403	ubiquitin conjugation	cytoplasm
Ribosomal RNA-processing protein 8 GN=RRP8	456	rDNA silencing	nucleus
Microtubule-associated protein RP/EB family member 1 GN=MAPRE1	268	microtubule elongation	cytoskeleton
Tumor necrosis factor receptor superfamily member 6 GN=FAS	335	cell death	PM
Mitochondrial inner membrane protease subunit 2 GN=IMMP2L	175	protein targeting	mitochondria
Mitochondrial import receptor subunit TOM34 GN=TOMM34	309	protein import	mitochondria
DnaJ homolog subfamily C member 9 GN=DNAJC9	260	chaperone	nucleus
Translation initiation factor eIF-2B subunit alpha GN=EIF2B1	305	translation	cytoplasm, PM
Phosphatidylinositol-binding clathrin assembly protein GN=PICALM	652	endocytosis	PM, vesicle
Isoform 2 of ATP synthase subunit s-like protein GN=ATP5SL	257	energy homeostasis	mitochondria
Nuclear protein localization protein 4 homolog GN=NPLOC4	608	protein degradation	ER, cytoplasm
Sorbitol dehydrogenase GN=SORD	357	oxidoreduction	mitochondria
Rho GTPase-activating protein 1 GN=ARHGAP1	439	cdc24 binding	cytoplasm
Elongator complex protein 2 GN=ELP2	826	chromatin organization	cytoplasm, nucleus
SUMO-activating enzyme subunit 2 GN=UBA2	640	protein sumoylation	cytoplasm, nucleus
Chromosome X open reading frame 56, isoform CRA_b GN=CXorf56	222		
Gelsolin GN=GSN	782	actin capping	cytoskeleton
EH domain-containing protein 2 GN=EHD2	543	membrane reorganization	PM, endosome
Folate transporter 1 GN=SLC19A1	591	potocytosis	PM
Isoform Short of Ubiquitin carboxyl-terminal hydrolase 5 GN=USP5	858	protein deubiquitination	lysosome
Rho GTPase-activating protein 17 GN=ARHGAP17	881	cell polarity maintenance	PM, cytoplasm
Pseudouridine synthase GN=PUS1	427	transcription	mitochondria
Pre-mRNA-processing factor 17 GN=CDC40	579	pre-mRNA splicing	nucleus
CKLF-like MARVEL transmembrane domain-containing protein 6 GN=CMTM6	183	chemotaxis	PM, exosome
Importin subunit alpha-3 GN=KPNA3	521	nuclear protein import	cytoplasm, nucleus
Negative elongation factor B GN=COBRA1	580	transcription inhibition	Nucleus
Reticulon-4-interacting protein 1, mitochondrial GN=RTN4IP1	396	oxidoreduction	mitochondria
Protein MAK16 homolog GN=MAK16	300	RNA binding	nucleus

Isoform 2 of 6-phosphofructokinase, muscle type GN=PFKM	780	glycolysis	cytoplasm
Eukaryotic translation initiation factor 2D GN=EIF2D	584	tRNA delivery to ribosome	cytoplasm
Cytoplasmic dynein 1 light intermediate chain 2 GN=DYNC1LI2	492	vesicle mobility	cytoskeleton
Cyclin-H GN=CCNH	323	cell cycle control	nucleus
Coiled-coil domain-containing protein 50 GN=CCDC50	306	ubiquitin conjugation	cytoplasm
Coronin-1B GN=CORO1B	489	cell motility	cytoskeleton
Ganglioside-induced differentiation-associated protein 1 GN=GDAP1	358	mitochondrial fission	mitochondria
MMS19 nucleotide excision repair protein homolog GN=MMS19	1030	DNA repair	nucleus
Switch-associated protein 70 GN=SWAP70	585	membrane ruffling	PM, cytoplasm
5'-AMP-activated protein kinase catalytic subunit alpha-1 GN=PRKAA1	559	energy metabolism	cytoplasm, nucleus
Queuine tRNA-ribosyltransferase subunit QTRTD1 GN=QTRTD1	415	tRNA modification	mitochondria
Glioma pathogenesis-related protein 1 GN=GLIPR1	266	lipid metabolism	PM
Isoform 3 of Nucleoredoxin GN=NXN	435	disulfide oxidoreduction	cytoplasm, nucleus
Signal transducer and activator of transcription 3 GN=STAT3	770	growth factor signaling	cytoplasm, nucleus
Exocyst complex component 2 GN=EXOC2	924	membrane fusion	exocyst, PM
EH domain-binding protein 1-like protein 1 GN=EHBP1L1	1523		PM
ATPase ASNA1 GN=ASNA1	348	protein targeting to ER	ER, cytoplasm
N-alpha-acetyltransferase 15, NatA auxiliary subunit GN=NAA15	866	angiogenesis	cytoplasm, nucleus
Microtubule-associated protein 1B GN=MAP1B	2468	microtubule polymerization	cytoskeleton
Tripartite motif-containing protein 16 GN=TRIM16	564	differentiation	cytoplasm
Elongator complex protein 1 GN=IKBKAP	1332	histone acyltransferase	cytoplasm, nucleus
Arf-GAP w/ coiled-coil, ANK repeat and PH domain-containing protein 2 GN=ACAP2	778	growth factor signaling	endosome
Dystonin GN=DST	7570	cytoskeletal linker	cytoskeleton
EPS15L1 protein GN=EPS15L1	864	endocytosis	PM
TFIIH basal transcription factor complex helicase XPB subunit GN=ERCC3	782	DNA repair	nucleus
Probable ATP-dependent RNA helicase DHX37 GN=DHX37	1157	RNA processing	cytoplasm, nucleus

Appendix C – R code

C.1. Source code for summarySE function (written by Frank Stein)

```
summarySE <- function(data=NULL, measurevar, groupvars=NULL, na.rm=FALSE, conf.interval=.95, .drop=TRUE) {
 require(plyr)

 # New version of length which can handle NA's: if na.rm==T, don't count them
 length2 <- function (x, na.rm=FALSE) {
  if (na.rm) sum(!is.na(x))
  else       length(x)
 }

 # This is does the summary; it's not easy to understand...
 datac <- ddply(data, groupvars, .drop=.drop,
                .fun= function(xx, col, na.rm) {
                  c( N    = length2(xx[,col], na.rm=na.rm),
                     mean = mean   (xx[,col], na.rm=na.rm),
                     sd   = sd     (xx[,col], na.rm=na.rm),
                     IQR   = IQR     (xx[,col], na.rm=na.rm),
                     quantile = quantile (xx[,col],na.rm=na.rm)
                  )
                },
                measurevar,
                na.rm,
                .progress="text"
 )

 # Rename the "mean" and quantile columns
 #datac <- rename(datac, c("mean"=measurevar))
 datac <- rename(datac, c("quantile.0%"="min"))
 datac <- rename(datac, c("quantile.100%"="max"))
 datac <- rename(datac, c("quantile.50%"="median"))
 datac <- rename(datac, c("quantile.25%"="first.quartile"))
 datac <- rename(datac, c("quantile.75%"="third.quartile"))

 datac$se <- datac$sd / sqrt(datac$N)  # Calculate standard error of the mean

                ciMult <- qt(conf.interval/2 + .5, datac$N-1)
 datac$ci <- datac$se * ciMult

 return(datac)
}
```

C.2. Examplary script for analysis of calcium traces (used to generate Fig. 2.13)

```
setwd("~/EMBL/Sph-Ca paper/NPC patient FB")
library("ggplot2")
library("reshape")

npc1 <- read.delim("NPC_dataset.txt")
npc2 <- read.delim("20141119_dataset.txt")
npc <- rbind(npc1, npc2)
rm(npc1)
rm(npc2)

npc["condition"] <- NA
npc$condition[grep("WT", npc$Experiment.ID)]<- "WT"
npc$condition[grep("NPC", npc$Experiment.ID)]<- "NPC"

npc["lipid"] <- NA
npc$lipid[grep("cgSph", npc$Experiment.ID)]<-"Sph"
npc$lipid[grep("dhSph", npc$Experiment.ID)]<-"neg ctrl"

npc["response"]<-F
npc$response[which(npc$Max.change>=10)]<-T

npc["duration"]<-TRUE
npc$duration[which(npc$No.of.frames<60)]<-F

npc$condition<-factor(npc$condition, ordered=T, levels=c("WT", "NPC"))

npc_sum<-summarySE(npc, measurevar="Norm.Mean", groupvars=c("ROI.Class","condition", "lipid","time", "duration"),
na.rm=TRUE)

npc_plot<-ggplot(subset(npc_sum, time<=60&ROI.Class=="Uncaged_Cell"&lipid=="Sph"&duration=="TRUE"),
            aes(time,mean,colour=condition))
npc_plot<-npc_plot+geom_line(size=1.07)+geom_errorbar(aes(ymax=mean+se,ymin=mean-se),alpha=0.4, size=0.8)
npc_plot<-npc_plot+theme_bw(base_size=16)+scale_y_continuous(limits=c(0.9,1.8))+scale_x_continuous(breaks=seq(0,60,10))
            +theme(panel.grid.major=element_blank(),panel.grid.minor=element_blank())+theme(legend.justification=c(0,1),
            legend.position=c(0,1.05), legend.title=element_blank(), legend.text=element_text(size=14),
            legend.key=element_blank(), panel.border=element_blank(), axis.line=element_line(),
            axis.title.y=element_text(vjust=0.7), axis.title.x=element_text(vjust=0.7))
npc_plot+labs(title=" ",y="normalized intensity",x="time [s]")+scale_colour_manual(breaks=c("WT", "NPC"),  labels=c("WT",
"NPC"), values=c("#1b9e77", "#d95f02"))

ggsave(file="NPC_Uncaged_Cell.pdf", width=7,height=4.425)

NPC_hist_plot<-ggplot(subset(npc,time==0&ROI.Class=="Uncaged_Cell"&(condition=="WT"|condition=="NPC")&lipid=="Sph"),
            aes(fill=condition, x=Max.change))+geom_histogram(binwidth=5, colour="black")+facet_grid(~condition)
NPC_hist_plot<-NPC_hist_plot+theme_bw(base_size=16)+scale_x_continuous(breaks=seq(0,120,20))
            +theme(legend.position="none")+theme(panel.grid.major=element_blank(),panel.grid.minor=element_blank(),
            axis.line=element_line(), axis.title.y=element_text(vjust=0.7), axis.title.x=element_text(vjust=0.7),
            panel.border = element_rect(fill=NA, colour = "black", size=0.7))
NPC_hist_plot<-NPC_hist_plot+theme(strip.background = element_rect(colour="black", fill="grey"))
            +scale_x_continuous(breaks=seq(0,120,20))
NPC_hist_plot+scale_fill_manual(values=c("#1b9e77", "#d95f02"))

ggsave(file="NPC_histo.pdf", width=7, height=4.425)
```

Acknowledgements

I am thankful to Carsten Schultz for giving me the opportunity to pursue a PhD in his laboratory, for introducing me to the field of Chemical Biology and for giving me the freedom to pursue my own ideas during this time.

I also thank all past and present members of the Schultz laboratory for creating a great working atmosphere. I am especially grateful to Per Haberkant for all his support within and outside the field of sphingolipids, to Martina Schifferer for a great collaboration and her help with electron microscopy as well as to Madeleine Schultz for reading and improving my thesis.

I am very honored to have had such a distinguished Thesis Advisory Committee: I thank Felix Wieland, Joost Holthuis, Anne-Claude Gavin and Rainer Pepperkok for their scientific input and valuable discussions over the years.

Many aspects of this work would not have been possible without the support of all members of the Sphingonet training network, but especially Fran Platt and Howard Riezman. Thanks a lot for all your contributions to and support of my PhD work.

I am very happy to have made many new friends at EMBL. Thanks to all the predocs of 2011 for such a fun start of my time here and the all members of the EMBL diveclub for exciting trips and many special moments above and under water. A big thank you goes to Christophe and Paola for great friendships, many fun times outside EMBL and for always having open doors (and ears); and to Joana for awesome times as flat mates, many Dr. Who sessions and for cheering me up when I was feeling down.

Ein großes Dankeschön gilt allen meinen “alten” Freunden aus Österreich: die Julias, die Andis, die Marias, Philipp und Agi. Danke für die vielen Besuche, gemeinsamen Urlaube und die legendären Parties.

I am forever grateful to Léo for his love, patience and support, especially in stressful times. I love you so much.

Am allermeisten bedanke ich mich bei meiner Familie und besonders bei meinen Eltern. Ich bin so dankbar, dass ihr mir den Weg in die Wissenschaft nicht nur ermöglicht, sondern mich dabei auch immer unterstützt habt. Ohne euch wäre nichts davon möglich gewesen.